UNICAMP

UNIVERSIDADE ESTADUAL DE CAMPINAS
Instituto de Física Gleb Wataghin

VÍTOR HUGO RIBEIRO

ANÉIS DE VORTICIDADE EM COLISÕES RELATIVÍSTICAS DE ÍONS PESADOS

VORTICITY RINGS IN RELATIVISTIC HEAVY ION COLLISIONS

CAMPINAS
2023

VÍTOR HUGO RIBEIRO

VORTICITY RINGS IN RELATIVISTIC HEAVY ION COLLISIONS

ANÉIS DE VORTICIDADE EM COLISÕES RELATIVÍSTICAS DE ÍONS PESADOS

Dissertação apresentada ao Instituto de Física Gleb Wataghin da Universidade Estadual de Campinas como parte dos requisitos exigidos para a obtenção do título de MESTRE EM FÍSICA, na Área de FÍSICA APLICADA.

Dissertation presented to the Institute of Physics Gleb Wataghin of the University of Campinas in partial fulfillment of the requirements for the degree of MASTER IN PHYSICS, in the area of APPLIED PHYSICS.

Orientador: JUN TAKAHASHI

ESTE TRABALHO CORRESPONDE À VERSÃO FINAL DA DISSERTAÇÃO DEFENDIDA PELO ALUNO VÍTOR HUGO RIBEIRO E ORIENTADA PELO PROF. DR. JUN TAKAHASHI.

CAMPINAS
2023

Ficha catalográfica
Universidade Estadual de Campinas
Biblioteca do Instituto de Física Gleb Wataghin
Lucimeire de Oliveira Silva da Rocha - CRB 8/9174

R354v

Ribeiro, Vítor Hugo, 1999-
Vorticity rings in relativistic heavy ion collisions / Vítor Hugo Ribeiro. – Campinas, SP : [s.n.], 2023.

Orientador: Jun Takahashi.
Dissertação (mestrado) – Universidade Estadual de Campinas, Instituto de Física Gleb Wataghin.

1. Movimento turbulento. 2. Jatos (Física nuclear). 3. Polarização (Física nuclear). I. Takahashi, Jun, 1971-. II. Universidade Estadual de Campinas. Instituto de Física Gleb Wataghin. III. Título.

Informações Complementares

Título em outro idioma: Anéis de vorticidade em colisões relativísticas de íons pesados
Palavras-chave em inglês:
Vortex-motion
Jets (Nuclear physics)
Polarization (Nuclear physics)
Área de concentração: Física Aplicada
Titulação: Mestre em Física
Banca examinadora:
Jun Takahashi [Orientador]
Pedro Cunha de Holanda
Cristiane Jahnke Fiorini da Silva
Data de defesa: 24-08-2023
Programa de Pós-Graduação: Física

Identificação e informações acadêmicas do(a) aluno(a)
- ORCID do autor: https://orcid.org/0000-0002-2641-2877
- Currículo Lattes do autor: http://lattes.cnpq.br/3783591692429936

MEMBROS DA COMISSÃO EXAMINADORA DA DISSERTAÇÃO DE MESTRADO DO ALUNO VÍTOR HUGO RIBEIRO - RA 220612, APRESENTADA E APROVADA AO INSTITUTO DE FÍSICA GLEB WATAGHIN, DA UNIVERSIDADE ESTADUAL DE CAMPINAS, EM 24/08/2023.

COMISSÃO JULGADORA:

- Prof. Dr. Jun Takahashi – Presidente e orientador (IFGW/UNICAMP)
- Prof. Dr. Pedro Cunha de Holanda (IFGW/UNICAMP)
- Profa. Dra. Cristiane Jahnke Fiorini da Silva (Instituto de Física da USP)

OBS.: Ata da defesa com as respectivas assinaturas dos membros encontra-se no SIGA/Sistema de Fluxo de Dissertação/Tese e na Secretaria do Programa da Unidade.

CAMPINAS

2023

"Physics is like sex: sure, it may give some practical results, but that's not why we do it."

(Richard Feynman)

AGRADECIMENTOS

Agredeço a meu orientador, Prof. Dr. Jun Takahashi, pela confiança, por todos os ensimentos oferecidos ao longo destes dois anos e por todo o esforço realizado pela minha formação. Também agradeço de maneira especial a todos os participantes da Colaboração 3C, Prof. Dr. David Dobrigkeit Chinellato e Prof. Dr. Giorgio Torrieri, da Universidade Estadual de Campinas, Prof. Dr. Michael Lisa, da Universidade Estadual de Ohio, Prof. Dr. Chun Shen, da Universidade Estadual de Wayne e ao Dr. William M. Serenone, da Universidade de São Paulo. Obrigado pelas discussões, sugestões e ensinamentos que, com certeza, foram de suma importância para o desenvolvimento deste trabalho.

Agradeço a meus pais, Vilma Pires da Silva Ribeiro e João Xavier Ribeiro, por sempre me apoiarem da melhor forma possível e estarem sempre ao meu lado, me motivando a seguir o caminho que escolhi. Agradeço também a minha namorada Beatriz, por todo amor, carinho e compreensão que da sua forma me ofereceu.

Agradeço aos amigos e companheiros de trabalho que passaram pelo grupo Hadrex. Em especial ao Gabriel Reis Garcia, Gianni Liveraro, Gabriel Rabelo Soares, André Gianinni e João Paulo Piccheti. Agradeço pela companhia aos longo dos dias de pesquisa, pelas discussões e outros momentos dentro da sala S08.

Seria difícil mencionar o nome de todas as pessoas que fizeram parte da jornada que me trouxe até este momento. No entanto, eu expresso minha gratidão a cada uma dessas pessoas que contribuíram diretamente ou indiretamente para essa trajetória. Obrigado!

Por fim, agradeço ao apoio financeiro oferecido pela Fundação de Apoio a Pesquisa do Estado de São Paulo (FAPESP), sob o número 21/10750-3. Extendo esse agradecimento também ao apoio inicial, oferecido pelo Conselho Nacional de Desenvolvimento Científico e Tecnológico (CNPq), sob número 161246/2021-4, e pela Coordenação de Aperfeiçoamento de Pessoal de Nível Superior (CAPES), sob número 88887.639694/2021-00. E agradeço também ao Instituto de Física Gleb Wataghin e a Universidade Estadual de Campinas, por todo o suporte e serviços oferecidos ao longo deste período.

RESUMO

Colisões relativísticas de íons pesados representam fenômenos fascinantes e complexos, em que núcleos atômicos colidem com energias extremamente altas, criando um ambiente de condições extremas que é impossível de se medir diretamente. Apesar dessa complexidade, diversos resultados relacionados a esse cenário foram obtidos nas últimas décadas e aprimoraram nosso conhecimento sobre as propriedades fundamentais da matéria nuclear. Dentre esses resultados, dois deles - o comportamento coletivo do meio e o fenômeno de perda de energia dos jatos - têm servido como sinais consistentes para a formação de um novo estado da matéria nuclear, conhecido como Plasma de Quarks e Glúons (QGP). Recentemente, uma nova medição relacionada ao acoplamento vorticidade-spin foi observada, abrindo novas oportunidades para explorar e extrair as características do QGP. Com base nesse contexto, neste trabalho, empregamos um modelo que conecta o comportamento fluido do QGP e a perda de energia dos jatos para estudar o processo de termalização dos fluxos de energia-momento depositados no meio de colisão por um jato que foi absorvido. Realizamos um estudo sistemático sobre a formação de anéis de vorticidade dentro do QGP e utilizamos a polarização das partículas como um observável para medir os efeitos causados pelos anéis. Expandimos análises anteriores nesse modelo para um cenário mais realista, considerando eventos não centrais e flutuações nas condições iniciais. Os resultados deste trabalho foram obtidos por meio da aplicação de uma cadeia de simulação computacional híbrida com modelos considerados estados da arte [TRENTo + (3+1D)MUSIC + iSS]. Com essa cadeia de simulação, reproduzimos a formação e evolução da estrutura de anéis em um modelo hidrodinâmico relativístico viscoso e estudamos a sensibilidade de um novo observável chamado "observável do anel" ($\mathcal{R}^t_\Lambda$), que é mensurável experimentalmente por meio da polarização de híperons Λ. Nós demonstramos que esse observável apresenta um aspecto robusto em relação a condições iniciais flutuantes e também analisamos sua dependência em relação a diferentes parâmetros do modelo, como velocidade e posição do jato, viscosidade de cisalhamento do fluido e centralidade da colisão. Nossos resultados mostram que a medição da polarização de partículas pode ser uma ferramenta poderosa para investigar diferentes propriedades das interações jato-meio e também pode oferecer um sinal claro da termalização da energia perdida por um jato que é absorvido pelo meio [1].

ABSTRACT

Relativistic heavy ion collisions represent a fascinating and intricate phenomena, where atomic nuclei collide at extremely high energies, creating an environment of extreme conditions that are impossible to measure directly. Despite this complexity, several results regarding such a scenario were obtained in the last decades and improved our knowledge about the fundamental properties of nuclear matter. Among these results, two of them - the collective behavior of the medium and the jet energy loss phenomenon - have served as strong signatures for the formation of a new state of nuclear matter known as Quark-Gluon Plasma (QGP). Recently, a new measurement regarding the vorticity-spin coupling was observed and set up new opportunities for exploring and extracting the characteristics of the QGP. Based on that picture, in this work, we employed a model that connects the fluid behavior and the jet energy loss to study the thermalization process of the energy-momentum currents deposited into the collision medium by a quenched jet. We performed a systematic study on the formation of vorticity rings inside the QGP and used the polarization of the particles as an observable to measure the ring effects. We expanded previous analysis on that model to a more realistic framework by considering non-central events and fluctuations in the initial conditions. The results of this work were obtained through the application of a state of art hybrid chain computer simulation [TRENTo + (3+1D)MUSIC + iSS]. With this simulation chain we reproduced the formation and evolution of the ring structure in a relativistic viscous hydrodynamic model and studied the sensitivity of a proposed "ring observable" ($\mathcal{R}^t_\Lambda$), which is experimentally measurable through the polarization of Λ hyperons. We showed that this observable presents a robust aspect regarding fluctuating initial conditions and we also analyzed its dependence on different model parameters, such as jet's velocity, position, fluid's shear viscosity, and collision centrality. Our results show that the measurement of particle polarization can be a powerful tool to probe different properties of jet-medium interactions and also can offer a clear signal of the thermalization of the energy lost by a quenched jet [1].

CONTENTS

CHAPTER 1

INTRODUCTION

Relativistic heavy-ion collisions have emerged as a fascinating area of research in physical sciences during the last decades. Specifically, the phenomenon of a collision and the resulting medium created by the interacting atomic nuclei characterizes the main focus of study in High Energy Nuclear Physics, which is the field in which this work is situated. Exploring this scenario provides a unique opportunity to investigate the fundamental nature of matter and the underlying dynamics of strong interactions, which corresponds to one of the fundamental forces of our universe. With these collisions, the scientists aims to explore the properties of nuclear matter, examine the behavior of quarks and gluons, and understand the formation of the quark-gluon plasma (QGP), a unique state of matter that is characterized by quarks and gluons in a deconfined state. The current knowledge we have about the QGP says that it exists at extreme temperatures and densities, and also presents an intriguing collective behavior which is analogous to a fluid [2–8].

The conditions required to create the QGP are predicted to be achieved in laboratory in particle accelerators and colliders, like the Relativistic Heavy Ion Collider (RHIC) in the United States and the Large Hadron Collider (LHC) on the border between France and Switzerland. Due to the relativistic velocities of the colliding nucleus in these particle accelerators, the form of the atomic nuclei changes as a consequence of the effect of Lorentz contraction and resemble thin discs, just as it is illustrated in the left part of Fig. 1.1. This process results in the formation of a medium with extremely high energy densities, leading to exceptionally high temperatures and short lifetimes. Because of these properties the study of the collision phenomenon and the QGP formation are very complicated tasks. The extreme temperature and rapid expansion makes it impossible to extract information from the system by using external probes [9]. The scientists just have access to the data from the pre-collision stage, which are the accelerated ions (left part of Fig. 1.1), and the post collision stage, which are the produced particles that emerges from the medium (right part of Fig. 1.1). Based on that picture, what scientists do to understand the system's internal dynamics (center part of Fig. 1.1) is to use theoretical interpretation and modeling possibilities that fits the experimental observations.

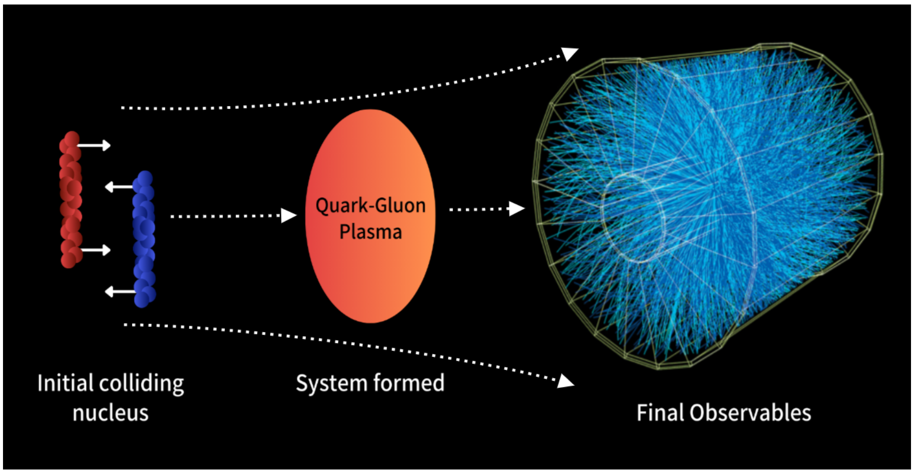

Figure 1.1: Schematic representation of a heavy-ion collision. Final observables from [10].

In that context, any new experimental observable that connects its characteristics to the properties of the medium represents a significant advancement for the evolution of our understanding of the phenomenon. One of the most important probes used to study this extreme medium are the hard probes that we call as jets. These structures, together with the jet quenching phenomenon, configures a strong evidence for the formation of the QGP [11–17]. Although scientists have made significant progress using jets and the jet quenching phenomenon, there are still open questions that must be answered in order to reach a complete understanding of medium interactions. One of these questions asks about the fate of the energy lost by a quenched jet and deposited into the medium. This topic, which represents one of the motivations behind the model studied in this work, remains a challenge and characterizes a point of intense research.

Another important result that forms a fundamental basis for this work is the concept of the vorticity-spin coupling. The physics underlying that concept was established through experimental observations published by the STAR collaboration at RHIC [18]. These observations revealed that the orbital angular momentum created in the QGP can induce the polarization of the final emitted hadrons. This discovery characterized a new opportunity to be explored for studying the properties of extreme nuclear matter.

By connecting together all the concepts presented up to this point, previous works developed by the 3C Collaboration [19, 20], showed a new path to explore the jet quenching phenomenon in the hydrodynamic nature of the system formed in heavy-ion collisions. They proposed a model that combines the fluid description of the QGP and the coupling between vorticity and polarization [18, 21] to investigate the thermalization of a quenched jet within the hydrodynamic medium. They demonstrated that the energy and momentum deposited from the jet into the QGP would generate a typical hydrodynamic structure, known as a vorticity ring (see Fig. 1.2). They showed that such a structure survives the explosive hydrodynamic evolution of the medium and that the effects of the vorticity ring will ultimately lead to a polarization pattern of the Λ hyperons emitted by the system. In order to measure this polarization pattern, they proposed an experimental observable called the “ring observable”, $\mathcal{R}^t_\Lambda$ [22].

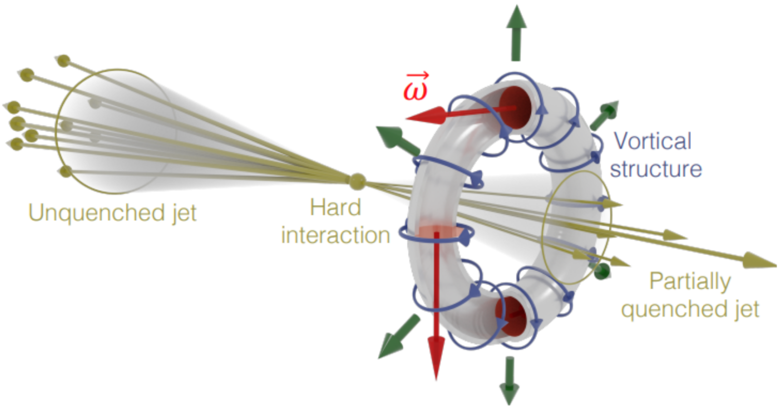

Figure 1.2: Schematic representation of the formation of a vorticity ring as a medium response to jet thermalization. In the figure, the red arrows corresponds to the direction of the created vorticity field ($\vec{\omega}$) and the green arrows corresponds to the direction of expansion of the vorticity ring. The blue circles represents the direction of the motion of the medium. From Ref. [19].

Continuing the research initiated by the 3C Collaboration, the main objectives of this work are centered in conducting a systematic study on the ring observable and also implementing a more realistic scenario for the analysis. We incorporated fluctuations in the initial states of heavy-ion collisions and simulated systems with different centrality classes. To provide a comprehensive understanding of this work the following chapters present the required concepts and theories, contextualizing them within the field of heavy-ion collisions. The text is structured in this way: In Chapter 2, we provided an introduction to the area of heavy-ion collisions and discussed the collective behavior observed in the collision medium. In Chapter 3, we focused on the hydrodynamic theory, starting from the non-relativistic case and progressing to the relativistic conditions of this study. In Chapter 4, we provided the connection between the rotational motion described by vorticity and the particle polarization measured in the detectors. In Chapter 5, we introduced and discussed the concept of hard probes, particularly jets and the jet quenching phenomenon. With the conceptual background established, in Chapter 6, we presented the model of jet thermalization used and detailed the simulation chain employed to obtain the final results. Finally, in Chapter 7, we showed and discussed the results of all the analysis performed in our study. To conclude, in Chapter 8, we present some closing remarks on the study performed for this research. A complementary analysis on medium expansion is also presented in the Appendix A.

Chapter 2

Heavy-Ion Collisions

The scenario studied in relativistic heavy-ion collisions involves the high-energy collision of two heavy nuclei. In such conditions, the study of the physics in that scenario requires a description that takes into account relativistic effects and an appropriate notation. The main goal of this chapter is to draw the general picture of a heavy-ion collision in experimental and phenomenological points of view.

2.1 Kinematic variables and centrality

In the study of relativistic heavy-ion collisions it is important to define the variables that will be applied to describe the system taking into account its relativistic nature. It is expected from the employed variables to present simple properties under a Lorentz transformation. Looking to the experimental side of the scenario, consider the coordinate systems represented in Fig. 2.1, which are drawn over a sketch of the ALICE experiment in the LHC. They represent, in general context, how a coordinate system is adapted in any collider experiment and is referred to as the laboratory frame.

The z-axis is usually taken over the beam direction and because of this is called the longitudinal direction. The x-axis is chosen to be parallel to the ground and the y-axis is placed in the vertical direction. This description represents the simplest way to define a coordinate system for our purposes, but due to the symmetry observed in the behavior of the particles produced in a collision, which propagates radially from the point where the collision happened, it is even more convenient to treat them using a spherical coordinate system. That representation is also shown in Figure 2.1, taking into account a polar (θ) and an azimuthal (ϕ) angles, together with a radius r.

Rapidity (y)

When working with particle colliders, a lot of collisions happen at the same time and the measurement that are taken from each one of these events are represented by the produced particles that reach the particle detectors. Among the several products that emerge from the collisions, some of them can not only be detected but also identified.

For those cases, there is a useful kinematic variable applied to characterize the kinematic condition of that particle [23].

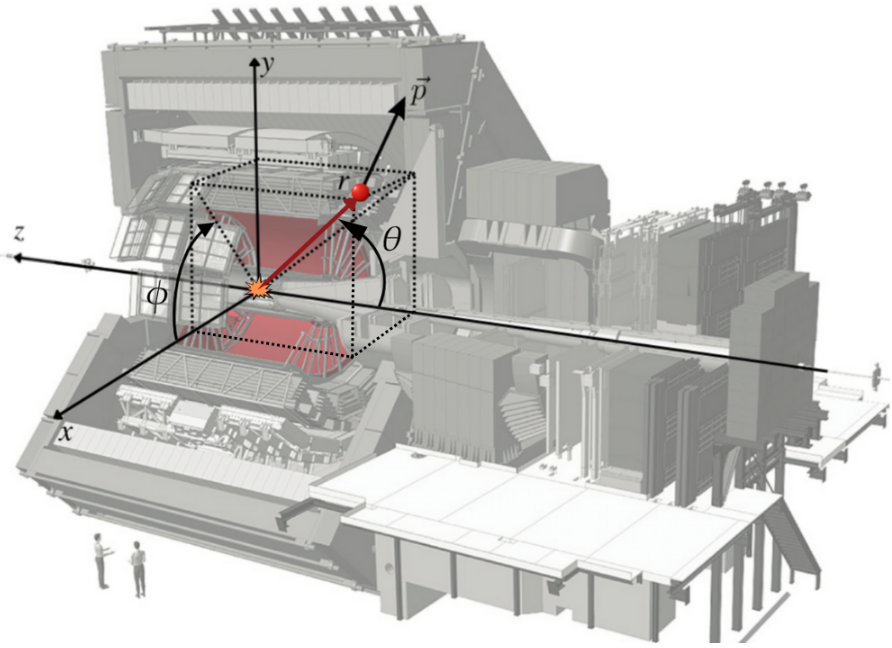

Figure 2.1: Sketch representing the coordinate system usually adopted to study the physics of heavy-ion collisions in colliders experiments. Modified from [24].

This kinematic variable is called "rapidity" (y) and represents an easier way to characterize the longitudinal rapidity of a hadron [25]

$$y = \frac{1}{2}\ln\left(\frac{E+p_z}{E-p_z}\right). \tag{2.1}$$

Equation (2.1) above, defines how the rapidity variable is measured. As can be seen, its value is given by a dimensionless quantity that is written in terms of the energy E of the particle and the z component of its momentum. The preference of using the rapidity is that its transformation over the change of a reference frame is very simple, being characterized just by an additive term [25]. Finally, because of this way that a Lorentz transformation takes place for the rapidity, its measurements are invariant along the beam axis. This kind of invariance is called boost-invariance [25].

Pseudorapidity (η)

On the other hand, complementing the previous situation, it is important to say that not all the products detected from a collision are identified. Several hadrons can't be distinguished and because of this, the experimentalists applies a different quantity, called pseudorapidity (η), that is measured through [25]

$$\eta = \frac{1}{2}\ln\left(\frac{|\vec{p}|+p_z}{|\vec{p}|-p_z}\right) = -\ln\left[\tan\left(\frac{\theta}{2}\right)\right]. \tag{2.2}$$

This variable, defined in the Eq. (2.2), needs just the polar angle (θ) of each detected hadron to be determined. Pseudorapidity is also given by a dimensionless quantity and presents the property of being invariant under Lorentz transformations. Comparing this quantity to the Rapidity (y), it is possible to note that in the relativistic limit, where $E \approx |\vec{p}|$, both quantities will coincide.

Space-time rapidity or spatial rapidity (η_s)

Still considering the concept just explained, which is the definition of pseudorapidity, there is another kinematic variable highly used in the heavy-ion collision scenario to describe the spatial-temporal behavior of the particles that are emitted from the system. This kinematic variable, called space-time rapidity or just spatial rapidity, is represented by a mathematical relation that is very close to the definition given in Eq. (2.2), except it is defined not by momentum quantities but space-time quantities [26]

$$\eta_s = \frac{1}{2} \ln \left(\frac{t+z}{t-z} \right) , \tag{2.3}$$

where t represents the time coordinate and z represents the longitudinal space coordinate.

The space-time rapidity appears as a kinematic variable that is partner of another variable called as proper time [26]

$$\tau = \sqrt{t^2 - z^2}. \tag{2.4}$$

Together, both relations represent convenient quantities to study the dynamics of the particles and the separation between two events in space and time in relativistic systems. They are particularly applied in phenomenological models in order to simulate the longitudinal dynamics of the medium formed in a collision.

Transverse momentum (p_T)

The last common variable used to study the physics of heavy-ion collisions that will be presented here is the transverse momentum. This variable represents the components of momentum that are transverse to the beam axis and that can be measured through the equation represented below [25]:

$$p_T = \sqrt{p_x^2 + p_y^2} \tag{2.5}$$

When studying the products of heavy-ion collisions, most of the particles produced in an event are emitted perpendicular to beam direction (see Fig. 2.2). It makes the transverse momentum an important variable in the study of particle properties and the stages of a collision.

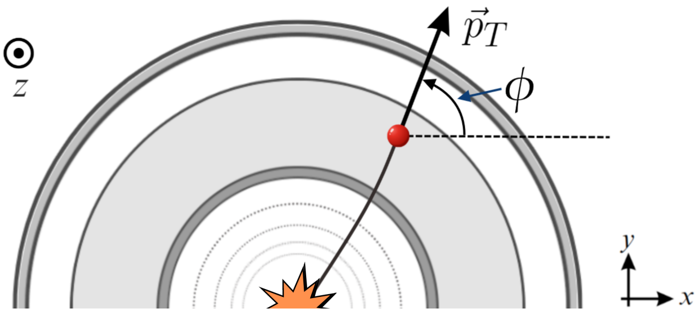

Figure 2.2: Sketch representing the cross section view of a collider experiment that shows a particle (red circle) emitted from the collision and the ϕ angle between the x-axis and the projection of that particle's momentum into the $x - y$ plane, which represents its transverse momentum.

Multiplicity and centrality classification

In addition to the kinematic variables applied in the description of particle's behavior individually, a general characteristic that is used to separate and classify the different collisions is the multiplicity. That observable refers to the number of charged particles produced in an event and measured in a detector. The usual way to classify the collision events is done through the idea of centrality classes: the most central events are characterized by the highest values of multiplicity, while peripheral events correspond to the lowest values of multiplicity. To illustrate that picture, Table 2.1 shows the centrality classification and the multiplicity density measured at midrapidity ($|\eta| < 0.5$) by ALICE Collaboration for Pb-Pb collisions at $\sqrt{s_{NN}} = 2.76$ TeV.

Table 2.1: Values of centrality class and charged particle multiplicity density for Pb-Pb collisions at $\sqrt{s_{NN}} = 2.76$ TeV and $|\eta| < 0.5$, measured by ALICE Collaboration [27].

Centrality	$\mathrm{d}N_{ch}/\mathrm{d}\eta$
0-5%	1601 ± 60
5-10%	1294 ± 49
10-20%	966 ± 37
20-30%	649 ± 23
30-40%	426 ± 15
40-50%	261 ± 9
50-60%	149 ± 6
60-70%	76 ± 4
70-80%	35 ± 2

These different multiplicity values are based on the geometry of each collision process. By treating the colliding nuclei as circles, Fig. 2.3 illustrates the possibilities that we can evaluate regarding the overlap region formed in their interaction. The phenomenological connection between the multiplicity observable and the geometry of the collision is based on a physical quantity called impact parameter (b), which represents the distance between the centers of each colliding nuclei. In the most central events the impact parameter is small and both nuclei collide head to head, forming an overlap region that is bigger and almost circular. On the other hand, in peripheral events, as the impact parameter increases, the area of the overlap region starts to decrease. For those cases, the geometry of the collision starts to be dominated by an almond shape.

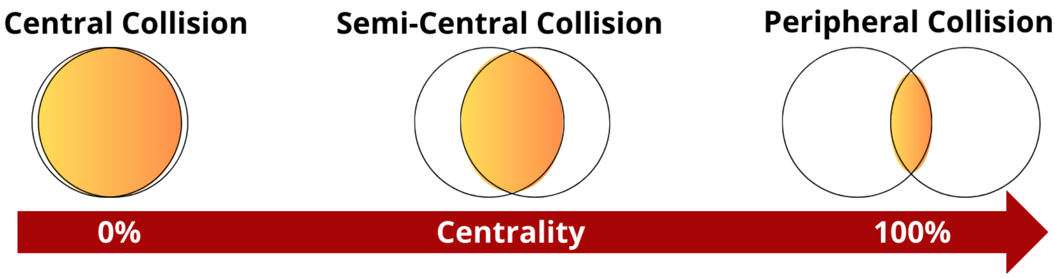

Figure 2.3: Illustration of the concept of collision centrality and its respective geometry. The values of centrality of the collision is represented in the x-axis, by the red arrow.

2.2 Stages of a collision

The current knowledge that we have about heavy-ion collisions was constructed over decades of theoretical and experimental studies. Nowadays it is well understood that such collisions have an extremely short lifetime, whose duration is of the order of 10 fm/c and reach extremely high temperatures, of the order of 400 MeV. Translating this to a more usual unit we obtain, respectively, values of the order of 10^{-23} s and 10^{12} K, which makes clear to our common sense how extreme it is. Phenomenological studies and analyses separated the process of a collision since its beginning to the detection of the final hadrons in a few main stages. Those stages are represented in the Fig. 2.4.

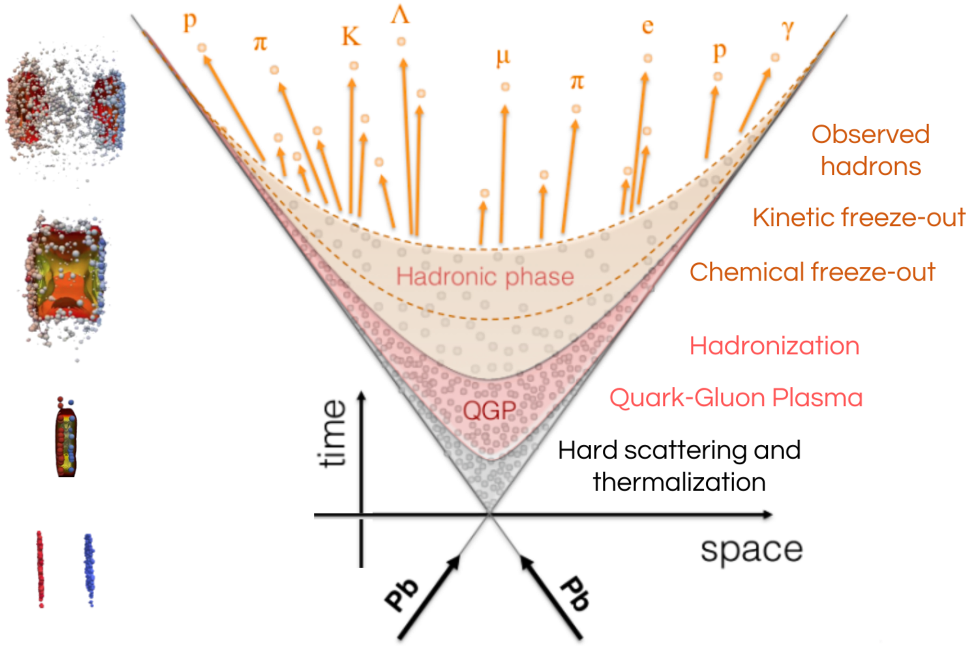

Figure 2.4: Left panels illustrate side views of the collision evolution [28]. The right panel corresponds to a schematic representation of the space-time evolution of a heavy-ion collision and its main stages. Modified from Ref. [29].

Initial condition

The first stage that takes place in a collision is characterized by the first interaction of the accelerated ions. It marks the beginning of the phenomenon and is set in the Figure 2.4 over the space axis, at a time equal to zero. In this stage, the nucleons of the ions will interact with each other and create a system that is called the initial condition or initial state. Usually, this interaction is modeled by the deposition of energy or entropy, resulting in a profile that will expand and evolve in the subsequent stages. A very important characteristic of the initial condition is its fluctuating nature, which arises from the quantum fluctuations in the position of the partons that constitutes each colliding nuclei [9].

Pre-equilibrium

After the collision, the system created presents very high values of energy density. This leads to a fast thermalization process, known as pre-equilibrium, and makes the system evolve from an out-of-equilibrium state to a point where local equilibrium is reached [9]. Such a transition lasts approximately 1 fm/c, involving both soft and hard scatterings, and also a fast expansion of the medium. It is during these initial moments that the jets are created inside the medium [30, 31].

Deconfined phase (QGP)

Once the system reaches local equilibrium, the medium formed consists of deconfined quarks and gluons, the quark-gluon plasma. In that point, the QGP starts to behave as a strongly interacting fluid with a very low shear viscosity, approaching the characteristics of a perfect fluid. During this stage, the QGP will expand and cool down [32].

Hadronization

In this phase, the deconfined quarks and gluons have already decreased their energies to a level in which they start to recombine again into bounded states, forming hadrons. This transition from a parton degree of freedom to a hadron degree of freedom is called hadronization [9].

Hadronic phase

The last stage of a heavy-ion collision is the hadronic phase, characterized by the interactions and decays of the hadrons produced in the hadronization process. During this stage, the system is formed by a hadron gas in resonance and the primary hadrons emitted from the collision will decay into more stable species, while interacting through elastic and inelastic scatterings. Eventually, the composition of hadron species becomes fixed, in the sense that the ratios of species will not change anymore. This point is called chemical freeze-out. From this point onward, the system dynamics are governed just by elastic interactions. Then, as the system expands the hadrons become too distant to interact with each other, marking the limit of kinetic freeze-out. Subsequently, the final hadrons are detected by particle detectors and will provide the data that we access from the collision event [33].

2.3 The Quark-Gluon Plasma

2.3.1 QCD phase diagram

One of the main purposes of particle accelerators and colliders, like LHC and RHIC, is to study the phase diagram predicted by Quantum Chromodynamics (QCD) for the hadronic matter. This diagram, represented in Fig. 2.5, reveals that under extreme conditions of temperature and energy density, the matter that we know from our everyday life could reach a new state with some new and intriguing properties. That state of nuclear matter, called Quark-Gluon Plasma, would arise from a transition where the components of the ordinary matter, which are the protons and neutrons, would be destroyed and giving rise to a medium of deconfined quarks and gluons [34].

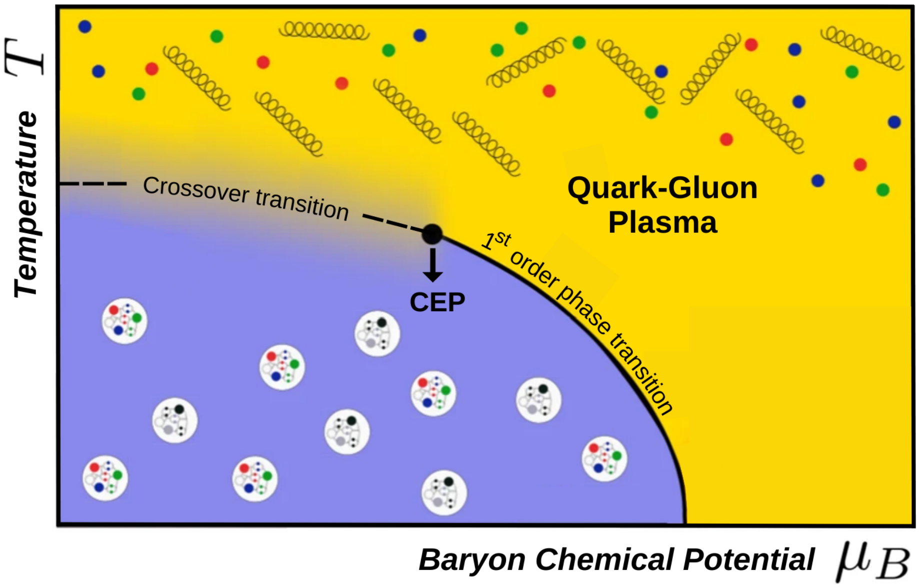

Figure 2.5: QCD Phase Diagram. The temperature is represented in the vertical axis and the baryon chemical potential in the horizontal axis. Modified from Ref. [35].

Nowadays, it is known that this transition of the hadronic matter to QGP can occur by different ways, depending on what region of the diagram it happens. In the case of regions characterized by high temperatures and low baryonic densities, the transition is defined by a smooth crossover [36]. The other possibility is in the regions with low temperatures and large baryonic densities, where theory indicates that the change of states appears to be a first order phase transition [37]. The specific point where the change between transitions occurs is called QCD critical end point (CEP) and the search for its location in the QCD phase diagram remains a topic of intensive research [38].

With the experiments involving particle accelerators a lot of data and results were obtained. Some of them provided important signatures for the existence of the QGP and also reported unexpected properties. The first evidence for the QGP was obtained from experiments conducted at RHIC. These results can be visualized in the famous series of “White Papers" [39–42], published in 2005 by the collaborations responsible for RHIC experiments: PHOBOS, BRAHMS, STAR and PHENIX.

One of the most interesting results from these first runs of heavy-ion collisions was the fluid behavior presented by the collision medium. This phenomenon, observed in both RHIC and LHC, serves as one of the signatures that points to the formation of QGP. Moreover, it has paved the way for studies with the aim to investigate the connection between the properties of this extreme matter and those of a hydrodynamic system. Among the signatures that indicate the existence of the QGP, the high opacity and the fluid nature can be seen as the strongest evidence [43]. In the next subsection we will briefly explore how the fluid behavior of the system was observed and how its observation supports the QGP interpretation. The high opacity property will be discussed in Chapter 5, since it depends on the definition of jets and the jet quenching phenomenon.

2.3.2 Anisotropic flow

Regarding the fluid behavior, the most strong indication for the formation of the QGP is the experimental observation of anisotropies in the final observables of a collision. These anisotropies, manifested in spatial and momentum distributions, represent an indicative of collective behavior being presented by the QGP. That observations suggest that the medium formed after a collision behaves as a strongly interacting system, just as a fluid.

Remembering the discussion about the initial condition geometry in Sec. 2.1, in the case of a hydrodynamic behavior, the evolution of the medium will be guided by the pressure gradients that arise from the geometric shape of the initial condition. If the initial form of the medium is characterized by an elliptic shape, the smaller axis of the system will develop a stronger pressure gradient, leading to a preference for the system to flow in that direction. Figure 2.6 provides a schematic illustration of this concept. In the left panel, the arrows represent the magnitude of the pressure gradient along the horizontal (red arrows) and vertical (blue arrows) axis of the medium. As the horizontal components of pressure are much bigger, the anisotropy observed by such a spatial distribution is converted into an anisotropy in momentum space. Then, as can be observed in the right panel of Fig. 2.6, it results in higher values for the horizontal components of momentum of the system.

To connect this phenomenological description to the experimental results from particle detectors, Fig. 2.7 shows an example of a spatial anisotropy obtained by STAR Collaboration [44]. This figure shows a particle distribution as a function of the azimuthal angle in the laboratory frame ϕ_{lab} relative to the orientation angle of the event Ψ_{plane}[1]. Due to the preference of the system to evolve in the horizontal direction, a higher number of particles is observed in $\phi_{lab} - \Psi_{plane} \approx 0$ and $\phi_{lab} - \Psi_{plane} \approx \pi$. Additionally, remembering the geometric picture of the centrality classification (see Fig. 2.3), as bigger is the centrality class of the measured events, closer to the shape of a thin ellipse the initial condition will look like. As a result, more intense will be the effect caused by the pressure gradients and consequently, more particles will be observed in that direction. That understanding is well represented in that measure presented by the STAR Collaboration, which shows higher peaks for peripheral events. That observation was understood as a consequence of the elliptical flow presented by the system and serves as a very compelling evidence that indeed the medium formed in the collision presents a collective behavior.

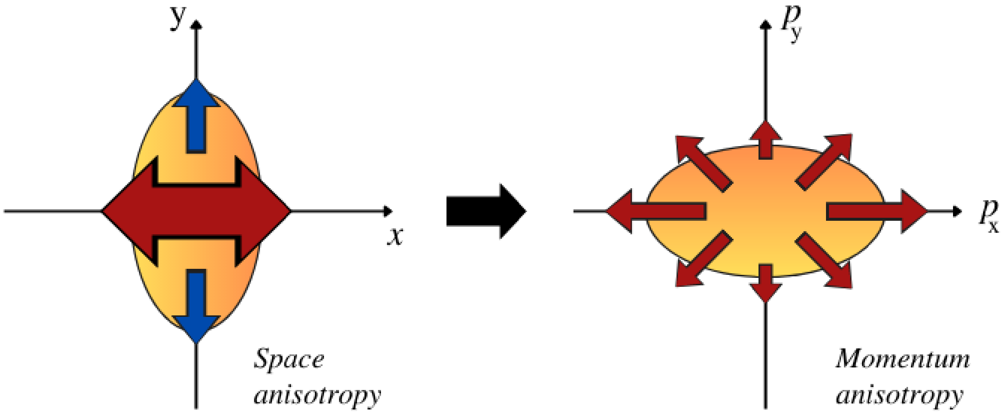

Figure 2.6: Schematic representation of the conversion of the initial shape anisotropy to a momentum anisotropy.

One of the forms of quantifying the anisotropy observed in the experimental particle distribution is using a Fourier Series [45]. In such an analysis, due to the symmetry observed in the distribution the result obtained is written just in terms of a cosine series as follows [46]

---

[1] This represents a measurement of the orientation of the ellipse formed in the initial condition relative to the x axis in the laboratory frame.

$$\frac{dN}{dyd\phi} = \frac{dN}{dy}\left(1 + \sum_{n=1}^{\infty} 2v_n \cos[n(\phi - \Psi_n)]\right); \tag{2.6}$$

$$v_n = \langle \cos[n(\phi - \Psi_n)] \rangle ,$$

where ϕ corresponds to the azimuthal angle, v_n are the anisotropy coefficients and Ψ_n is the n-th event-plane angle[2], given by

$$\Psi_n = \frac{1}{n} \arctan\left[\frac{\langle p_T \sin(n\phi)\rangle}{\langle p_T \cos(n\phi)\rangle}\right]. \tag{2.7}$$

The anisotropy coefficients in Eq. 2.6 represents a measure of the flow strength for each harmonic in the Fourier expansion. These harmonics can be understood as components of particle distribution related to different flow patterns observed in the created medium. While the initial condition predominantly exhibits an elliptic shape, its fluctuating nature allows for the approximation of other geometric forms in each one of the mediums formed by different collisions. This concept is illustrated in Fig. 2.8. Due to the different shapes, a different event plane angle is also defined for each harmonic, reflecting its geometric representation. In that context, the most important coefficient for our discussion is the v_2 coefficient, which represents the strength of the elliptic flow generated by the initial elliptic shape. Other coefficients as v_3 and v_4 are known, respectively, as triangular and quadrangular flow coefficients and are related to triangular and quadratic shapes in the initial state.

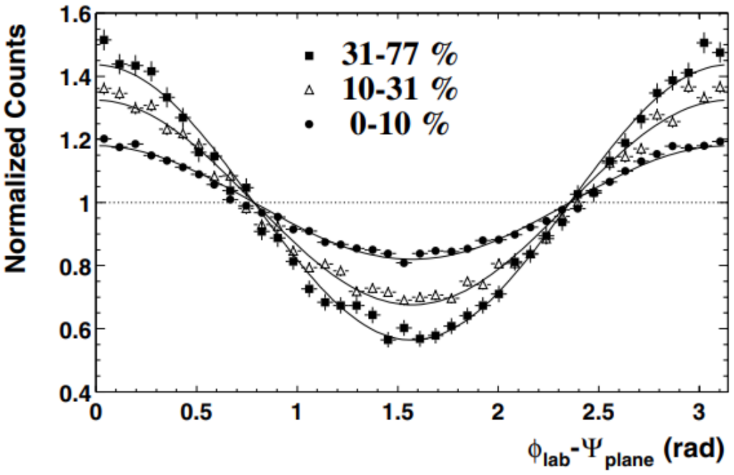

Figure 2.7: Distribution of charged particles from Au-Au events at $\sqrt{s_{NN}} = 200$ GeV measured by STAR Collaboration at RHIC as a function of the azimuthal angle ϕ relative to the event plane angle Ψ_{plane}. The measure is expressed for three different centrality classes [44].

---

[2] These angles are also expressed as $\Psi_{EP,n}$.

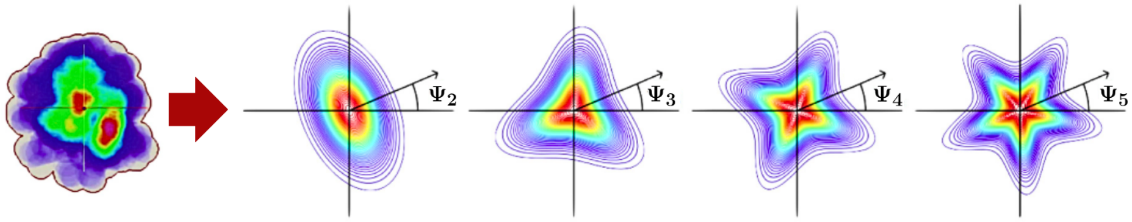

Figure 2.8: Schematic representation of the different shapes that can be assigned to the initial condition profile due to the fluctuations in partons positions and their respective event plane angles. Figure modified from Ref. [47].

The evidence for the collective behavior of the QGP is represented by the measures of the v_2 coefficient. This coefficient is the one intrinsically related to the conversion of the initial anisotropy in configuration space to an anisotropy in momentum space. Using that fluid interpretation, Fig. 2.9 shows one of the first results obtained from the calculus of v_2 with real data compared with hydrodynamic calculations for an ideal fluid. By evolving this ideal description to a fluid that presents viscosity properties, the agreement of the data becomes even more accurate. The right panel of Fig. 2.9 shows the measurements of v_n calculated from real data and compared with viscous hydrodynamic calculations. In that panel it is possible to observe that v_2 presents the largest magnitude compared to the higher order flow coefficients, which should be expected since it is the dominant form of the initial condition generated in non-central collisions. The remarkable agreement between the experimental results with hydrodynamic calculations set up the opportunity to use the fluid description in order to explore and extract information about the properties of the QGP.

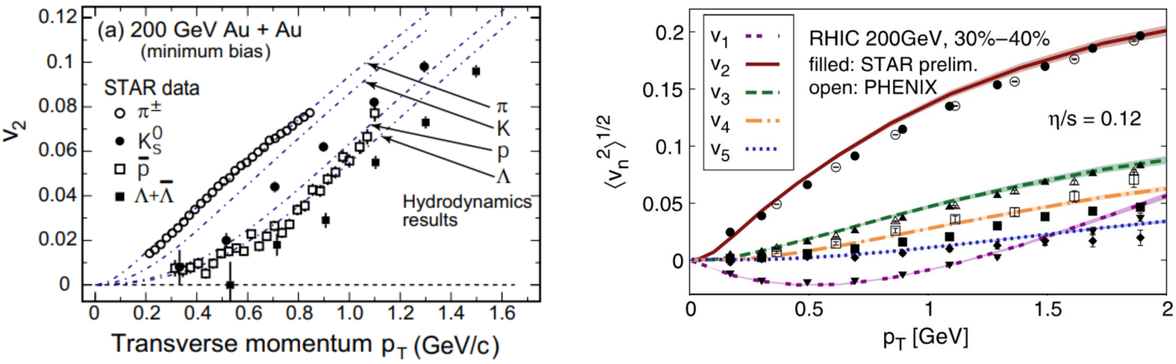

Figure 2.9: The left panel shows the elliptic flow parameter v_2 as a function of the transverse momentum p_T for different species of charged particles (data points). The dot-dashed lines represent the result from hydrodynamic calculations assuming an ideal fluid expansion. These results are from Au-Au collisions at 200 GeV [41]. In the right panel, the root-mean-square of the anisotropic flow coefficients as a function of the transverse momentum for Au-Au collisions at $\sqrt{s_{NN}} = 200$ GeV in the $30-40\%$ centrality class. The colored curves correspond to results obtained from hydrodynamic calculations. The plot was obtained from Ref. [43] and contains data from Ref. [48, 49].

CHAPTER 3

RELATIVISTIC HYDRODYNAMIC THEORY

Based on the collective behavior observed for the medium created in heavy-ion collisions, efforts were made to develop a physical theory of hydrodynamics that could be applied for the description of this scenario. Although a well established classical theory of hydrodynamics already existed, a transition to the relativistic conditions was necessary. The relativistic ideal hydrodynamics showed a remarkable agreement with experimental data, but it was the viscous version that performed the best. In this chapter, we will present the main topics and ideas of the development of the hydrodynamic theory applied in the study of heavy-ion collisions.

3.1 Non-relativistic hydrodynamics

In a synthetic form, the fluid dynamics can be understood as the description of a continuous medium, where any part of the system is always supposed to be larger compared to the units that constitutes that system. For example, in a bottle of water, the size of the individual molecules is much smaller than the total volume of water inside the bottle. So, in that case, we can apply what we call the hydrodynamic theory. Complementing this concept, when we talk about fluid motion, we are not focusing on the displacement of a single molecule of the system, but rather the movement of an element of volume of that system, which contains several molecules.

In developing the hydrodynamic theory used in daily conditions, a mathematical description of such a system requires the definition of a set of functions responsible for characterizing its dynamics. These functions includes the distribution of fluid velocity $\mathbf{v} = \mathbf{v}(x, y, z, t)$, the pressure $P = P(x, y, z, t)$ and the density $\rho = \rho(x, y, z, t)$ of the fluid. While the pressure and density are the thermodynamic quantities usually applied for describing a fluid system, any of two thermodynamic quantities can be used. Then, with these three functions and the equation of state of the fluid, we can completely define the state of a fluid in movement [50].

The crucial point of that mathematical description is characterized by conservation laws on the matter that is moving along as a fluid. By using that concept, Leonhard Euler developed an equation of fluid motion in 1755, known as *Euler's equation*, which is represented below

$$\frac{\partial \mathbf{v}}{\partial t} + (\mathbf{v} \cdot \nabla)\mathbf{v} = -\frac{1}{\rho}\nabla P. \tag{3.1}$$

Euler derived his equation by considering an ideal fluid, which neglects friction and heat conduction. Regardless of the fact that it did not describe a realist fluid, this mathematical relation represented a significant advancement for a complete description of fluid behavior. Equation (3.1) can be thought of as one of the fundamental equations of fluid dynamics. To improve Euler's description, Claude Navier and George Stokes worked out for the inclusion of the viscosity effects on the theory, resulting in one of the most important equations of all times: the *Navier-Stokes equation* [50]:

$$\frac{\partial \mathbf{v}}{\partial t} + (\mathbf{v} \cdot \nabla)\mathbf{v} = -\frac{\nabla P}{\rho} - \frac{1}{P}\nabla \Pi^{ki}, \tag{3.2}$$

$$\Pi^{ki} = \eta \left(\frac{\partial v_i}{\partial x_k} + \frac{\partial v_k}{\partial x_i} - \frac{2}{3}\delta_{ik}\frac{\partial v_l}{\partial x_l} \right) + \zeta \delta_{ik}\frac{\partial v_l}{\partial x_l}, \tag{3.3}$$

where for 3.3 the subscribed indices represents the spatial coordinates and the terms η and ζ are called viscosity coefficients[1], which can be specified respectively as shear viscosity and bulk viscosity. These viscosity coefficients measure the dissipative properties of the hydrodynamic system. The shear viscosity quantifies the dissipation caused by the motion between adjacent parts of the fluid, while the bulk viscosity characterizes the fluid's resistance to expansion or contraction.

The significance of the *Navier-Stokes equation* lies in its ability to accurately describe most of the fluids that we observe in nature. However, returning to the conditions presented by the phenomenon studied in this work, the equations discussed so far can not be applied. The system of our interest involves a regime of relativistic velocities and Eq. 3.2 represents a classical theory. Regarding its high applicability in classical problems, the formulation of Eq. 3.2 exhibits an intrinsic acausal behavior. That characteristic does not originate a problem in the non-relativistic cases, which allows us to ignore it. However, in relativistic systems, causality must be seen as a preserved property, and when applying the relativistic version of *Navier-Stokes equation* to describe such systems we ended up with equations of motion that are intrinsically unstable. Therefore they do not guarantee the physical causality of the phenomenon that we want to study [51].

---

[1] Here, it is important to establish that the η appearing in eq. 2.2 and in eq. 3.3 corresponds to different concepts. The first one represents the pseudorapidity variable, and the second refers to a viscosity coefficient in hydrodynamic theory. Despite the use of the same term, we will retain this notation because it is the customary notation employed in studies related to each concept. To enhance comprehension throughout this text, we will explicitly differentiate between both concepts.

3.2 Relativistic ideal hydrodynamics

From the failure of the Navier-Stokes theory in describing relativistic regimes, came the need to derive a new relativistic version for fluid motion. Following Euler's approach, it is possible to achieve this objective by once again starting with the concept of an ideal fluid. For this, the most general definition of an ideal fluid requires the fluid to satisfy the condition of local thermodynamic equilibrium. This means that all the elements that constitute the system must be in thermodynamic equilibrium, but not necessarily in the same equilibrium state.

After establishing that concept, the next step is then to define the densities and currents that correspond to the conserved quantities of the fluid that we want to describe. For our relativistic case, this requirement is satisfied by using the energy-momentum tensor $T^{\mu\nu}_{ideal}$ and the net baryon current J^{μ}_{B} [3,51]. These variables, expressed as a tensor and a 4-vector respectively, exhibit a characteristic form when described in the local rest-frame (RF) of system

$$T^{\mu\nu}_{RF} = \begin{pmatrix} \varepsilon & 0 & 0 & 0 \\ 0 & \mathcal{P} & 0 & 0 \\ 0 & 0 & \mathcal{P} & 0 \\ 0 & 0 & 0 & \mathcal{P} \end{pmatrix}, \tag{3.4}$$

$$J^{\mu}_{B,RF} = (\rho_B, 0, 0, 0)\,, \tag{3.5}$$

where ε corresponds to the energy density of a given point, $\mathcal{P}$ corresponds to the pressure and ρ_B to the baryon density associated to that point.

Using that local rest-frame definition, we can rewrite those variables to a general frame by performing a Lorentz boost. That transformation will depend on the fluid field velocity $\mathbf{u}$ and can be observed by its matrix representation as follows:

$$\Lambda^{\mu}_{\mu\nu} = \begin{pmatrix} \gamma & -u^x & -u^y & -u^z \\ -u^x & 1+(1+\gamma)^{-1}u^x u^x & (1+\gamma)^{-1}u^x u^y & (1+\gamma)^{-1}u^x u^z \\ -u^y & (1+\gamma)^{-1}u^y u^x & 1+(1+\gamma)^{-1}u^y u^y & (1+\gamma)^{-1}u^y u^z \\ -u^z & (1+\gamma)^{-1}u^z u^x & (1+\gamma)^{-1}u^z u^y & 1+(1+\gamma)^{-1}u^z u^z \end{pmatrix}, \tag{3.6}$$

with the Lorentz factor $\gamma = \sqrt{1+\mathbf{u}\cdot\mathbf{u}}$ and $u^{\mu} = (\gamma, \mathbf{u})$ being the velocity 4-vector field.

By applying 3.6 into 3.4 and 3.5, we obtain [3]

$$T^{\mu\nu}_{ideal} = \Lambda^{\mu}_{\alpha}(\mathbf{u})\Lambda^{\nu}_{\beta}(\mathbf{u})T^{\mu\nu}_{RF} = (\varepsilon + \mathcal{P})u^{\mu}u^{\nu} - \mathcal{P}g^{\mu\nu}, \tag{3.7}$$

$$J^{\mu}_{B} = \Lambda^{\mu}_{\alpha}(\mathbf{u})J^{\mu}_{B,RF} = \rho_B u^{\mu}, \tag{3.8}$$

where $g^{\mu\nu}$ is the space-time metric in a flat space.

Finally, to achieve the dynamical description of that system, the method consists of applying conservation laws to the quantities defined in 3.7 and 3.8, which leads to

$$\partial_\mu T^{\mu\nu}_{ideal} = 0, \tag{3.9}$$

$$\partial_\mu J^\mu_B = 0. \tag{3.10}$$

With these mathematical relations, the equations of movement of the fluid, for an ideal case, are defined. However, to characterize a solvable problem, an additional equation is needed to close the mathematical system created. At this point, we only have 5 equations, but we want to define the dynamics of a fluid that is characterized by four fields (ε, $\mathcal{P}$, $\mathbf{u}$ and ρ_B), which, in turn, are written in terms of six independent degrees of freedom. Therefore, to complete the problem, it is necessary to define a equation of state of the medium in the form

$$\mathcal{P} = \mathcal{P}(\varepsilon, \rho_B), \tag{3.11}$$

which is guaranteed to exist because of the assumption that we took into the beginning of local thermodynamic equilibrium [51].

3.3 Relativistic viscous hydrodynamics

Now that we have a relativistic ideal hydrodynamic theory, we can evolve its description by adding the viscosity effects. In a first approach, the introduction of these effects into the theory can be achieved by the sum of a second term to the initial energy-momentum tensor expressed in Eq. 3.7 [3, 51]

$$\mathcal{T}^{\mu\nu} = T^{\mu\nu}_{ideal} + \Pi^{\mu\nu}, \tag{3.12}$$

where the term $\Pi^{\mu\nu}$ represents the viscous stress tensor, which accounts for all the viscosity effects. That term, in comparison to what was observed for the *Narvier-Stokes equation*, can be separated in two contributions

$$\Pi^{\mu\nu} = \pi^{\mu\nu} + \Delta^{\mu\nu}\Pi, \tag{3.13}$$

where $\Delta^{\mu\nu} = g^{\mu\nu} - u^\mu u^\nu$ represents the local 3-metric, $\pi^{\mu\nu}$ corresponds to the shear stress tensor and $\Delta^{\mu\nu}\Pi$ to the bulk-viscous pressure.

With this new version of the energy-momentum tensor, the dynamics of the medium can once again be described through the previously mentioned conservation laws on the energy-momentum tensor and the net baryon current. However, at this point, it is important to say that these additional viscosity terms introduced to the theory represent a new set of dynamical variables and, therefore, require their own evolution equation.

To establish the definition of these variables and also avoid the problems that appear in the Navier-Stokes formulation, the theory of hydrodynamics that is used to reproduce the data of relativistic heavy-ion collisions is written through the Israel-Stewart formalism [52,53]. This approach derives the evolution equations for the viscous terms by considering the positivity of the entropy production rate, expressed as $T\partial_\mu S^\mu \geq 0$, where T represents the temperature and $\partial_\mu S^\mu$ refers to the entropy four-current. By applying this condition the equations for Π and $\pi_{\mu\nu}$ assumes the following form [54]

$$\Pi = -\zeta \partial_\mu u^\mu - \tau_\Pi \frac{d\Pi}{d\tau} - \frac{1}{2}\tau_\Pi \Pi \partial_\mu u^\mu - \frac{T\zeta}{2}\Pi \frac{d}{d\tau}\left(\frac{\tau_\Pi}{T\zeta}\right), \tag{3.14}$$

$$\pi^{\mu\nu} = \Delta^{\mu\nu\alpha\beta}\left[\eta \partial_\alpha u_\beta - \tau_\pi \frac{d\pi_{\alpha\beta}}{\tau} - \frac{1}{2}\tau_\pi \pi_{\alpha\beta}\partial_\lambda u^\lambda - \frac{T\eta}{2}\pi_{\alpha\beta}\frac{d}{d\tau}\left(\frac{\tau_\pi}{T\eta}\right)\right]. \tag{3.15}$$

where $\Delta^{\mu\nu\alpha\beta} = \frac{1}{2}\left(\Delta^{\mu\alpha}\Delta^{\nu\beta} + \Delta^{\nu\alpha}\Delta^{\mu\beta}\right) - \frac{1}{3}\Delta^{\mu\nu}\Delta^{\alpha\beta}$ represents a symmetric direct product of the projection operators that are orthogonal to the velocity field u^μ. The terms $\tau_{\Pi,\pi}$ correspond to the transport coefficients called relaxation times. Those terms, which appear for the shear (τ_π) and bulk (τ_Π), are very important since they are responsible to ensure the preservation of the causality property in the theory [54].

Finally, by utilizing the equations presented in this last subsection together with the equation of state of the relativistic fluid, the dynamics of such a system can be, in principle, solved. The remaining part is to specify the transport coefficients that appear in the theory: the shear and bulk viscosity coefficients η and ζ, and the relaxation times τ_π and τ_Π. The determination of these coefficients represents a widely studied topic regarding the description of the QGP fluid. Several studies were performed in order to better understand their behavior and influence in the dynamics of the system. Different approaches have been used, including simplified dependencies and also constant values. However, the only established information is that there exists a physical range that constrains the variation of these coefficient values. Further studies and more information about this topic can be found in the Refs. [55–59].

The description that was presented here corresponds to a formulation that is widely employed to describe the fluid dynamics of the QGP. But at the same time, it is important to emphasize that the Israel-Stewart formalism is not the only approach for constructing a dynamic theory for a relativistic viscous fluid [54]. Further information, more details, reviews and future perspectives in can also be found in Refs. [2–8,60].

3.4 Vorticity in hydrodynamics

In the case of a hydrodynamic theory, the circular motion is usually referred to as vorticity. Vorticity and angular velocity encapsulate the same idea and share a nearly identical mathematical definition, except for a multiplicative factor that may appear in the literature [61]. Although, it is common to define an equation for vorticity as [62]

$$\vec{\omega} \equiv \nabla \times \mathbf{u}. \tag{3.16}$$

Mathematically speaking, the vorticity is a pseudovector that quantifies how the velocity vector of a fluid changes when we move by an infinitesimal distance in a direction perpendicular to our initial position. Conceptually, it can be understood as the tendency of some point of the fluid to rotate.

Although vorticity is intrinsically associated with the idea of rotational motion, there are different types of kinematic scenarios that can give rise to a non zero vorticity. For example, it is possible to have a nonzero vorticity even when the flow of a hydrodynamic system occurs along parallel and straight lines. In this case, a variation of the speed of the flow across the lines of the system can generate some vorticity. To better illustrate this idea, Fig. 3.1 represents different schemes of velocity configurations relative to a point and its respective vorticity conditions.

In both, left and central panels of Fig. 3.1, the colored regions around each blue dot indicate that there is a tendency of that point to rotate, and for these specific cases, the rotation would happen in a clockwise direction. In contrast, for the right panel, it is possible to observe that the blue dot is placed in a white region, which indicates that there is no vorticity associated with that point. Additionally, a special case of our interest is represented in the left panel of Fig. 3.1. When the flow of a fluid assumes the configuration of concentric circles, we have a very specific situation in which together with the concept of vorticity arises another concept that is called vortex or vortices. A vortex is understood as a region of the fluid that rotates around a specific axis, which can be defined by a straight line or even by a curved line [61]. The vortex formation characterizes a common phenomenon in hydrodynamic systems, being represented by a lot of examples that can be cited and observed in our everyday life, such as smoke rings, whirlpools and also tornadoes and dust devils.

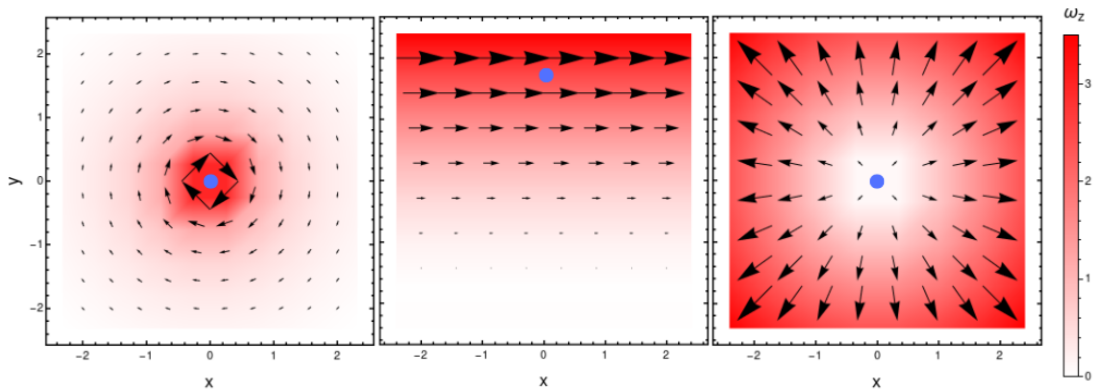

vorticity $\neq 0$ vorticity $\neq 0$ vorticity $= 0$

Figure 3.1: Schematic representation of different velocity fields and their associated vorticity. The color map represents the magnitude of the vorticity induced by each velocity field. The legend below each panel corresponds to the condition of vorticity observed at the blue dot for each respective field.

The dynamics and behavior of the vortices are characterized by the distribution of the velocity and vorticity fields of a fluid. Furthermore, once a vortex is formed, it can move and interact with the system in complex ways, carrying angular and linear momentum, as well as energy and mass with it [61].

Vorticity in relativistic hydrodynamics

Since for our purposes it is necessary to work in the relativistic regime, we need to expand the definition of vorticity to the relativistic case. Differently to the classical regime where there is just one definition, in the context of relativistic hydrodynamics several types of vorticity can be defined. Each one of these definitions presents distinct properties, which can be applied in different situations such as cosmology, astrophysics and, as we will use, particle physics [63]. Among all definitions of vorticity, two of them are of interest to us, since they are applied in the description of the system created in heavy-ion collisions.

The kinematical vorticity

The first definition is the so called kinematical vorticity [64]

$$\omega_{\mu\nu} = \frac{1}{2}(d_\nu u_\mu - d_\mu u_\nu) = \frac{1}{2}(\partial_\mu u_\nu - \partial_\nu u_\mu), \tag{3.17}$$

where $\omega_{\mu\nu}$ is a skew rank-2 tensor and the term u_μ corresponds to the four-velocity field of the fluid.

This definition represents a natural extension of the classical vorticity to a relativistic fluid. However, despite its intuitive form, such an extension does not conserve the same properties as its classic version. For example, it does not conserve the circulation quantity nor the total helicity, which are properties of interest to other studies.

The thermal vorticity

The second definition that will be presented here is called thermal vorticity. It represents the most important definition of vorticity for this work, since it is responsible for induce the local polarization of the particles in a relativistic fluid. The thermal vorticity is defined as [64]

$$\varpi_{\mu\nu} = -\frac{1}{2}\left(\partial_\mu \beta_\nu - \partial_\nu \beta_\mu\right), \tag{3.18}$$

where β corresponds to the temperature four-vector, whose definition is

$$\beta_\mu = \left(\frac{1}{T}\right) u_\mu. \tag{3.19}$$

The thermal vorticity is very relevant for the study of global polarization that will be presented in Chapter 4. It is also adimensional in natural units and has a magnitude given by $\hbar\omega/k_B T$, where ω corresponds to a constant angular velocity.

An interesting fact about thermal vorticity is that by replacing ω in its magnitude with the classical definition of vorticity (eq. (3.16)), the result is a very small number for most hydrodynamic systems, as can be seen in Table 3.1. However, significant values were measured for the hydrodynamic medium that is created in relativistic nuclear collisions, indicating that it represents the most vortical system observed so far [18].

Table 3.1: Indication of the magnitude of the vorticity measured for different natural phenomenons. Values obtained from [18, 65–68].

Situation	Vorticity (s^{-1})
Solar subsurface flow	10^{-7}
Large-scale terrestrial atmospheric patterns	$10^{-5} - 10^{-7}$
Supercell tornado cores	10^{-1}
The great red spot of Jupiter	10^{-4}
Rotating Quark-Gluon Plasma	10^{21}

CHAPTER 4

VORTICITY AND SPIN POLARIZATION IN THE QGP

Physics develops our understanding of the universe by carefully observing and analyzing natural phenomena. The concept of spin originated this way, from empirical observations. Since this property is one of the basis of this work, the main goal of this chapter is to present the idea of spin, connecting this to the phenomenon of heavy-ion collisions.

4.1 The concept of spin

The concept of spin emerged from Quantum Mechanics, which is the fundamental theory that provides a physical description of nature at atomic and subatomic scale. Before the introduction of spin, the study of the quantum properties of matter were believed to be completely defined by a wave equation ψ, written as a function of its spatial coordinates x, y and z. However, new experimental evidence, such as the results of the Stern-Gerlach experiment [69] (1922), pointed out that the existing wave function was inadequate to describe the quantum nature of particle behaviors. Those results suggested that a new internal degree of freedom would be necessary to reach the completeness for the quantum description. This internal degree of freedom was initially conceived as an internal angular momentum, which now we refer to as spin. By incorporating this new concept into the theory, the description of the total angular momentum of a particle, or a system of particles, was rewritten as [70]

$$\mathbf{J} = \mathbf{L} + \mathbf{S}, \tag{4.1}$$

which means that the total angular momentum $\mathbf{J}$ of a system should be composed by a sum of the orbital angular momentum $\mathbf{L}$ and the spin $\mathbf{S}$.

Since the introduction of the concept of spin, it has played a crucial role in the description of nature provided by modern physics. Nowadays it is well established that almost all elementary particles possess this internal degree of freedom and that it is necessary to explain a wide range of phenomena across different scales, from the microscopic to the macroscopic level.

In the context of elementary particle physics, which is studied through the framework of Quantum Field Theory, the spin holds a fundamental significance for describing interactions and symmetries in the universe. Particularly for the high energy particle physics scenario, the investigation of spin-related effects began to be made in the 1970s, coinciding with the emergence of heavy-ion collisions experiments. Consequently, a natural and important question arose regarding the possibility of doing spin physics within the context of heavy-ion collisions [71]. Currently, our understanding of spin physics in this scenario relies on phenomenological models that use the connection between angular momentum and spin to provide a bridge between what happens during the collision to what is observed in the detectors.

4.2 Spin-vorticity coupling

Even before the concept of spin, some experiments already demonstrated an intriguing connection between rotational motion and the magnetization of a body. The two experiments that showed this relationship in a more evident way were performed in 1915, a few years before the discovery of spin. These experiments, related to the Einstein-de Haas [72] and the Barnett [73] effects, played a crucial role in establishing this connection. Figure 4.1 shows a schematic representation of the observations made in each experiment.

In the Einstein-de Hass effect, represented in the left panel, it was observed that an iron cylinder undergoing magnetization inversion generates mechanical rotation. Simultaneously, the experiment performed by Barnett, represented in the right panel, demonstrated that a rotating iron exhibits a non-zero magnetization. Even with this brief description, it is possible to conclude that these experiments clearly indicate a reciprocal relationship. The implications of these findings suggested that there should exist a close connection between the concepts of magnetism and mechanical angular momentum.

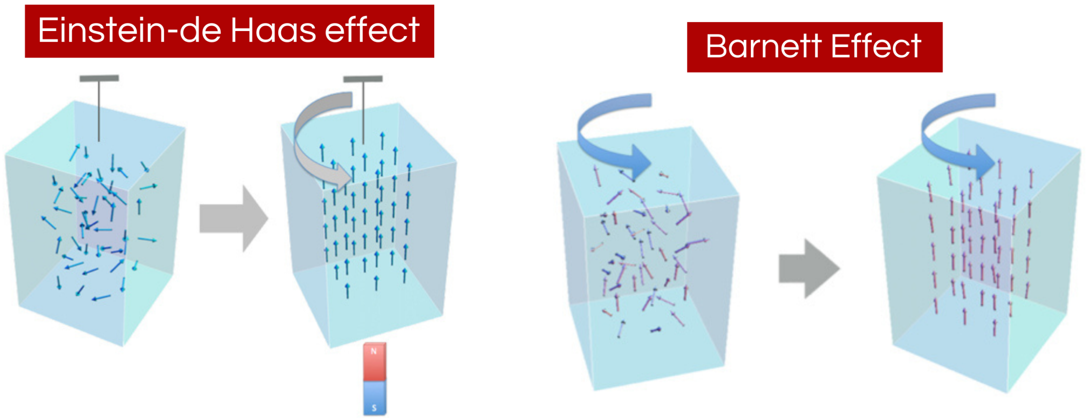

Figure 4.1: Schematic representation of what was observed for the Einstein-de Haas effect (Left) and the Barnett effect (Right). [74]

Nowadays we know that magnetization is a macroscopic property that arises from microscopic electric currents or the alignment of particles spins within bulk matter [75, 76]. After the discovery of spin and the establishment of Eq. (4.1), we now recognize that the effects observed in those experiments involve the transfer of angular momentum between the system's orbital motion and the spin of particles.

In these first examples, the mechanical motion considered in the experiments is simply represented by a rigid-body rotation and is far away from what we need, which is a description that could be applied in fluid dynamics. However, those experiments characterized a great advance in the understanding of the connection between rotational motion and spin. A hydrodynamic version of mechanical movement inducing spin polarization took decades to be observed and was measured just recently, in 2016, by an experiment conducted by Takahashi [77]. This experiment, schematically represented in Fig. 4.2, marked the first observation of a spin-vorticity coupling and was very important in order to establish the phenomenon. Despite the recent experimental observation, the idea of vorticity generating spin polarization has a long history. In the specific context of heavy-ion collisions, the oldest reference of an angular momentum being generated in the collision medium and inducing the polarization of hadrons can be traced back to 2004 [78].

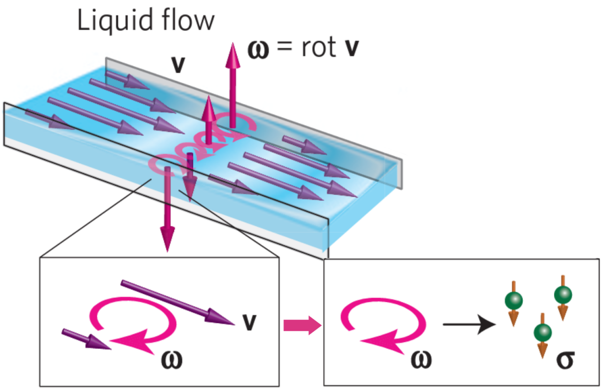

Figure 4.2: Schematic representation of the experiment performed by Takahashi *et al* for the spin hydrodynamic generation. The panel illustrates the velocity **v** and the induced vorticity ω in a liquid which flows through a narrow channel. The velocity gradient generated by the viscosity with the walls gives rise to a local rotational motion (vorticity),which induces the polarization σ of the electrons. Figure modified from [77].

One theoretical approach that resulted in a phenomenological model connecting the hydro-aspect to the observed final particles is known in the field as the Cooper-Frye formula. In that model, it is assumed that the QGP remains in a state of local thermodynamic equilibrium until it freezes out to non-interacting hadrons. By making this assumption, the coherent evolution of the system's dynamic states can be used to transport the properties of the fluid system to the final hadronic level achieved after the collision. This process, developed by Fred Cooper and Graham Frye, involves integrating over the freeze-out hyper-surface $\Sigma(x, y, z, t)$ of the fluid. That integration accounts for the entire distribution of the fluid, which reaches the freeze-out condition at different positions and times. This model has been highly successful in describing the momentum spectra of particles emitted from the QGP and is expressed by the following equation [79,80]

$$E\frac{dN}{d^3p} = \int_\Sigma f(x,p)p^\mu d\Sigma_\mu, \tag{4.2}$$

where $f(x,p)$ corresponds to the phase space distribution function and p^μ to the four momentum of the fluid cell.

Cooper and Frye's work opened doors for the application of this model to other properties, as for example the spin-vorticity coupling. Extending their idea to the spin context, a mathematical relation was developed as an attempt to describe the mean spin vector of particles. In that context, for the specific case of spin 1/2 particles, that relation turned out to be sufficient in describing the polarization of such particles. At leading order, it is expressed as [21]

$$S^\mu(p) = -\frac{1}{8m}\epsilon^{\mu\rho\sigma\tau}p_\tau \frac{\int_\Sigma d\Sigma^\lambda p^\lambda n_F(1-n_F)\varpi_{\rho\sigma}}{\int_\Sigma d\Sigma^\lambda p^\lambda n_F}, \tag{4.3}$$

where p represents the four-momentum of the particle, $\varpi_{\rho\sigma}$ corresponds to the Thermal Vorticity defined in Eq. 3.18 and

$$n_F = \left(1 + \exp\left[\beta \cdot p - \mu_{CP} Q/T\right]^{-1}\right), \tag{4.4}$$

represents the Fermi-Dirac distribution, which is characterized through the four-temperature $\beta^\mu = u^\mu/T$, the chemical potential μ_{CP} and a generic charge Q.

For completeness, while the polarization of spin 1/2 particles is entirely described by the calculation of the mean spin vector, in the case of particles with spin greater than 1/2, a full description of its polarization requires the use of more quantities, like for example, the complete spin density matrix $\Theta_{rs}(p)$.

As the mean spin vector calculated by Eq. 4.3 is also integrated over the freeze-out hypersurface, it is sometimes called the Cooper-Frye formula for the spin. That relation, which works well for particles and antiparticles, shows us that, at leading order, the polarization of the particles emitted from the hypersurface depends on the gradients of temperature and velocity, which is explicitly shown on the dependence of the thermal vorticity.

4.3 Measuring polarization

One of the main methods used to extract particle polarization from collision events involves the analysis of the topology of particle decays. The term "topology" is used to refer to the pattern or configuration presented by the products of a decay process. The topology is determined by the properties of the dynamics of the decay. In some specific cases, the daughter particles generated in a decay present a direct relation to the spin vector of its parent particle. The left panel of Fig. 4.3, schematically represents a result obtained by a tracking system and highlights the trajectory observed for the daughter particles generated in the Λ decay.

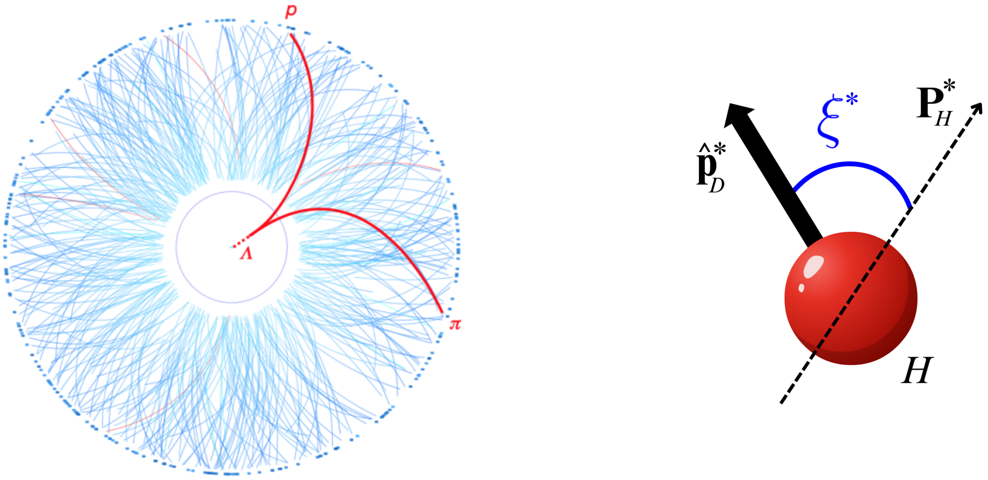

Figure 4.3: (Left) Schematic representation of a hyperon decay in an event display similar to what is obtained in the TPC detectors [18]. (Right) Vectors and angles involved in the analysis of a hyperon decay.

Among all the decays that happen after a collision, the cases that allow us to extract the spin polarization of the parent particles are represented by the weak parity-violating hyperon decays. In that kind of processes, a hyperon decays into a charged meson and a charged baryon, where the latter is emitted from the decay with a momentum direction that points preferentially in the direction of the polarization of the parent particle. Such a property, which is illustrated in the right panel of Fig. 4.3, states that once we measure the angular distribution of the daughter baryons, it is possible to calculate the spin polarization of its parent hyperon. The mathematical relation that represent this statement is given by [81]

$$\frac{dN}{d\Omega^*} = \frac{1}{4\pi}(1+\alpha_H \mathbf{P^*}_H \cdot \hat{\mathbf{p}}^*_D) = \frac{1}{4\pi}(1+\alpha_H \cos\xi^*), \tag{4.5}$$

where $\mathbf{P}^*_H$ correspond to the polarization vector of the hyperon, $\hat{\mathbf{p}}^*_D$ is a unit vector that points in the direction of the momentum of the daughter particle and ξ^* is the angle formed between $\hat{\mathbf{p}}^*_D$ and the polarization direction. The $*$ symbol in the upper index represents quantities that are measured in the rest-frame of the decaying hyperon. The decay parameter α_H, which varies for each different species of hyperon, represents an experimental factor that is used to characterize its decay [82].

One interesting possibility, based on Eq. 4.5 and of significant interest in the experimental setting, is the evaluation of the polarization projection in a specific direction, as for example $\hat{\mathbf{n}}$. By averaging the projection of the momenta of daughter particles along $\hat{\mathbf{n}}$, the obtained result represents the projection of the hyperons spin in that direction [21].

$$\langle \hat{\mathbf{p}^*}_D \cdot \hat{\mathbf{n}} \rangle = \frac{\alpha_H}{3} \mathbf{P}^*_H \cdot \hat{\mathbf{n}}. \tag{4.6}$$

The purpose of developing this relation is motivated by the search for anisotropies in the distribution of particle polarization from heavy-ion collision. A great example of this context is given by several works in literature, which indicate that a huge amount of Orbital Angular Momentum (OAM) is generated by the matter that interacts during the collision. As we already know by the historic and physical picture, this observation presents an ideal opportunity to investigate the mechanisms underlying the transfer of OAM and spin polarization in that scenario.

4.4 Global and local polarization of Λ hyperons

In a heavy-ion collision, it is possible to approximate the Orbital Angular Momentum of the nucleus-nucleus interaction using the geometric configuration of the system's elements. A schematic illustration of that concept is shown in Fig. 4.4. In the represented center-of-mass frame, the incoming particles are moving in the same axis with a momentum $\mathbf{p}_{beam}$, but in opposite directions. A displacement between them is given by the impact parameter $\mathbf{b}$, which points from the center of one nucleus to the center of the other. Using this configuration, the OAM of the system, generated after the collision, can be defined as [21]

$$\mathbf{J}_{sys} = \mathbf{b} \times \mathbf{p}_{beam}. \tag{4.7}$$

In the laboratory frame, the direction of the propagating beam represents the longitudinal axis $\hat{\mathbf{z}}$ while the impact parameter $\mathbf{b}$ is set on the horizontal axis $\hat{\mathbf{x}}$. According to this configuration, the resulting angular momentum is expected to be oriented along the $\hat{\mathbf{y}}$ axis. That description corresponds to an ideal situation and differs from what is observed in real measurements. Considering the experimental aspect, the orientation of $\mathbf{b}$ in a real experiment will hardly agree with the laboratory reference. The most general picture that we can address to a real situation is given by $\mathbf{b}$ defining an angle Ψ_{RP} relative to the x direction, that will vary in each event. Such an angle is called as Reaction Plane Angle and it is used to characterize the orientation of the plane defined by the impact parameter $\mathbf{b}$ of each event and the longitudinal direction $\mathbf{p}_{beam}$.

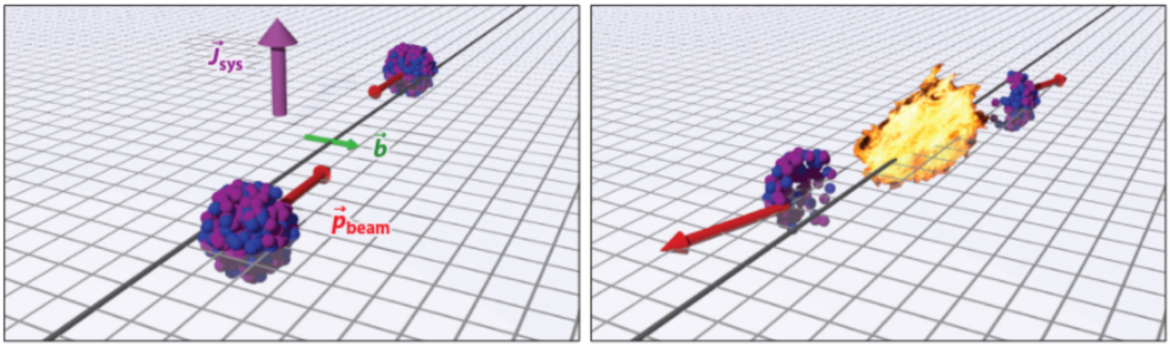

Figure 4.4: Schematic representation of a heavy-ion collision in the center-of-mass frame. The left panel illustrates the primary vectors associated with the geometric and physical aspects of a collision. In the right panel, it is shown the quark-gluon plasma created and the deflected spectator nucleons that do not participate in the collision. Figure taken from Ref. [21].

Despite this geometric complication, there are experimental techniques, which uses the angular correlations between the emitted particles and allow us to approximate the angle formed between the horizontal axis $\hat{\mathbf{x}}$ in the lab frame and the real orientation of $\mathbf{b}$ in each collision (see Fig. 4.5 about this angle, which is called reaction plane angle[1] (Ψ_{RP})). Those techniques are based on the anisotropy distribution presented by the particles due to the anisotropic flow of the QGP [83]. Finally, once the orientation of the real event is established, we are able to do the calculations for each event and then approximate the direction of the OAM for each event.

Within this framework, the measure of the global polarization ($\bar{P}_H$) is performed by taking the preferential direction $\hat{\mathbf{n}}$ in the direction of the OAM, for each event. In that context, by substituting $\hat{\mathbf{n}} = \mathbf{J}_{sys}$ into Eq. (4.6), the final relation applied in experimental analysis to extract the global polarization is expressed by the following relation [18]

$$\bar{P}_H = \left\langle \mathbf{P}_H \cdot \hat{\mathbf{J}}_{sys} \right\rangle = \frac{8}{\pi\alpha_H} \frac{\left\langle \cos(\phi^*_D - \phi_{\mathbf{J}_{sys}}) \right\rangle}{R_{EP}}, \tag{4.8}$$

where $\mathbf{P}_H$ corresponds to the polarization vector of the parent hyperon, ϕ^*_D corresponds to the azimuthal angle of the daughter charged particle of the decay, measured in the rest frame of the decaying hyperon, and $\phi_{\mathbf{J_{sys}}}$ is the azimuthal angle of $\hat{\mathbf{J}}_{sys}$ relative to the x-axis in the laboratory frame. The factor R_{EP} corresponds to an experimental correction factor related to the resolution in determining the event plane angle and depends on the centrality of collision [83].

---

[1] It is important to establish that the angles Ψ_{EP} and Ψ_{RP} are conceptually different. While Ψ_{RP} corresponds to a real angle of orientation of the ellipse shape relative to the laboratory frame, the angle Ψ_{EP} represents an experimental estimate for Ψ_{RP}. In practical terms, since we just have access to the experimental estimate, we approximate $\Psi_{EP} = \Psi_{RP}$.

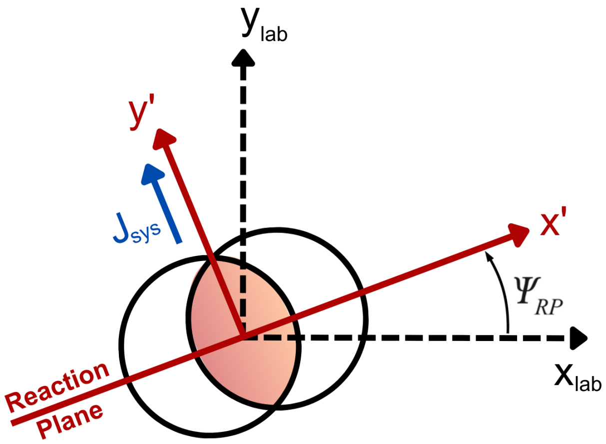

Figure 4.5: Schematic representation of the reaction plane angle (Ψ_{RP}) relative to laboratory frame of reference.

Recent studies have reported global polarization results for different types of hyperons [84]. However, the initial measurements of this quantity focused on the decays of Λ and $\bar{\Lambda}$ hyperons. This fact is influenced by the feasibility of identifying the decay vertices of these particles and also by their production rates compared to the other species. The main decay mode of the Λ is given by $\Lambda \rightarrow p + \pi^-$, which configures the weak parity-violating decay of interest and can be reproduced using the Cooper-Frye formula for the spin (Eq. (4.3)), since this particle has spin 1/2. For that case, the decay parameter value required for the $\bar{P}_\Lambda$ calculations is $\alpha_\Lambda = 0.732 \pm 0.014$ [82].

The first measurements of global polarization were conducted by STAR Collaboration, at RHIC [18]. After that, other measurements were performed in different experiments and were also reproduced by phenomenological models. A synthesis of these results can be observed in Fig. 4.6, which shows the global polarization as a function of the beam energy of the collision. The observed trend in Fig. 4.6 shows that the polarization decreases with increasing beam energy and essentially disappears at high energies. At a first view, this may appear counter intuitive, as one might expect an increase of polarization due to an increase of $|\mathbf{J}_{sys}|$ with the energy of the collision. However, there are other properties related to high-energy conditions that may affect the final global polarization. Some of these properties are represented by the increased temperature and consequently increased time scale of the dynamic evolution of high energy events [85,86]. Considering the vorticity picture within that scenario, the magnitude of vorticity decreases significantly until reaching the thermal freeze-out condition, which leads to a decrease in polarization. Another possible cause that could be related to the observed behavior is the transfer of vorticity to regions of greater rapidity values [87], which becomes hard to measure due to experimental limitations.

The result of all these mentioned factors is a weaker polarization being observed in the direction of the total angular momentum as the energy of the collision increases. In addition to the understanding of the physics behind Fig. 4.6, an important fact to be observed and emphasized is the efficiency of the phenomenological models in reproducing the polarization of the Λ hyperons. In particular to the hydrodynamic model, which applies the relation 4.3 to calculate the final polarization. That model exhibits a remarkable agreement with the experimental data.

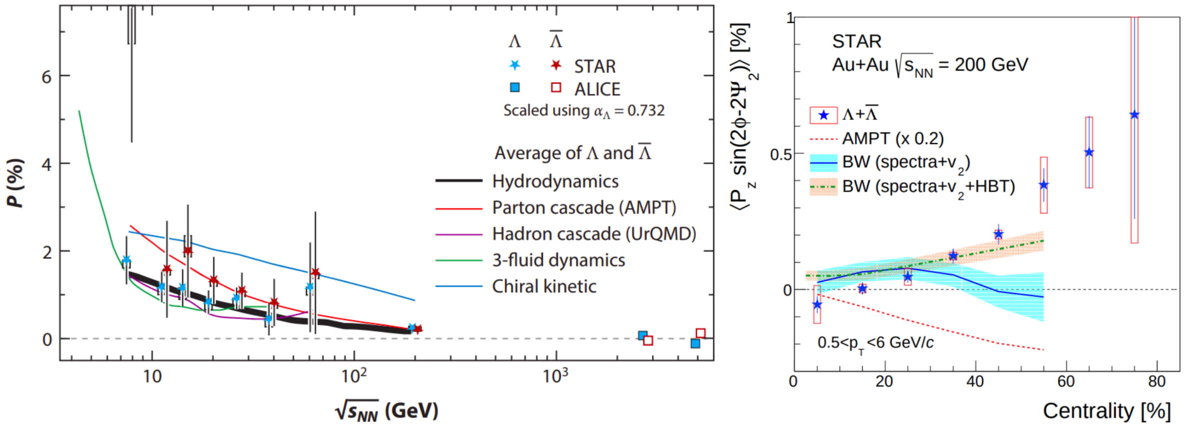

Figure 4.6: (Left) Global polarization of Λ and $\bar{\Lambda}$ particles as a function of beam energy at midrapidity from midcentral Au-Au (20-50%) or Pb-Pb (15-50%) collisions [18,21,88]. (Right) Second order coefficient of the longitudinal polarization of Λ and $\bar{\Lambda}$ as a function of the centrality class for Au-Au collisions with $\sqrt{s_{NN}} = 200$ GeV. More information can be obtained in Ref. [89].

Now, moving in a different direction, the polarization induced along $\mathbf{J}_{sys}$ is not the only interesting result that can be observed from nuclear collisions. The longitudinal component of the polarization also provides important information about the dynamics and anisotropies of the system. That component of polarization, which is perpendicular to $\mathbf{J}_{sys}$, can be observed locally in momentum space by taking the preferential direction $\hat{\mathbf{n}}$ along the longitudinal direction $\hat{\mathbf{p}}_{beam}$. The main difference from global to local polarization is that in global representation, the measure of polarization is performed as a sum over all the Λ particles that are emitted from the system, usually at midrapidity ($y < 0.5$). On the other hand, in the case of local polarization, we have its representation in a momentum space. This allows for a clearer visualization of the polarization distribution within the system, which remains hidden in the global representation due to the symmetries that vanish the signal when we integrate over all particles.

The right panel of Fig. 4.6 displays the second order coefficient of the longitudinal polarization from Λ and $\bar{\Lambda}$ as a function of the centrality class. The observed behavior demonstrates that the signal increases with centrality, resembling the dependence of the anisotropy coefficient v_2 [90]. In that context, it is possible to relate the transverse expansion of the collision medium with some non-zero vorticity [91–94]. This expansion, which is governed by geometric anisotropies, can generate a vorticity field in the system and leads to a polarization perpendicular to the transverse plane, which is the longitudinal direction [89].

The predicted vorticity pattern created in the transverse expansion indicates that the longitudinal polarization should present a typically quadrupolar distribution, expressed as a function of the azimuthal angle relative to the event plane ($\phi - \Psi_{EP,2}$). That behavior, which is represented in Fig. 4.7, was observed for non-central collisions not only in hydrodynamic calculations (right panel), but also in experimental data (left panel). The plot in the right panel of Fig. 4.7 shows the local distribution of longitudinal polarization as a color map of p_x versus p_y. That result is in qualitative agreement with the azimuthal dependence observed in the left panel of Fig. 4.7, which shows $\langle \cos\theta_p^* \rangle$ values as function of the Λ emission angle relative to the event plane[2]. This last result demonstrates that the detection angle of the daughter protons, which are used to extract the Λ polarization, presents the same behavior observed in the hydrodynamic model for the first half of the azimuthal interval. Although the general structure of the signal is described by the hydrodynamic model, it is possible to see that the magnitude and the sign of the polarization presented are in discrepancy to what is observed experimentally. The first quadrant, which is represented in the right panel of Fig. 4.7 by the region where p_x and p_y are positive, shows a negative sign for the polarization signal and a signal of the order of -1.5×10^{-2}. In contrast, the experimental data in the left panel of Fig. 4.7 shows a positive sign and a magnitude of the order of 0.3×10^{-3}.

That divergence between the models and the experimental data remains an open issue in the area. Recent efforts [95–97] were done in order to provide the missing part of the relation between vorticity and polarization in hydrodynamics systems. In those works, it is proposed that the particle polarization should present extra contributions due to a thermal shear tensor [95,96] and also due to the gradients of μ_B/T [96]. In particular for the derivation developed in Ref. [95], a great advancement in the correction of the sign was achieved. However, it is still necessary to develop phenomenological studies in order to understand how these contributions affect the polarization of the final state hadrons.

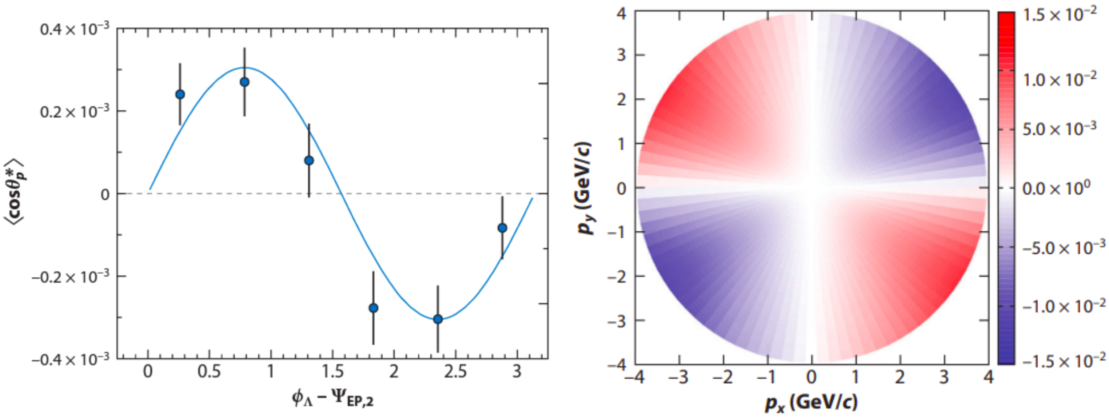

Figure 4.7: (Left) Values of $\langle \cos\theta_p^* \rangle$ as a function of the Λ emission angle relative to the event plane for Au-Au collisions at $\sqrt{s_{NN}} = 200$ GeV in 20-60% centrality class [21]. (Right) Hydrodynamic calculations of the longitudinal polarization in the transverse plane for the same collision system represented in the left panel [21].

---

[2] Here, the angle $\cos\theta_p^*$ corresponds to the polar angle of the daugther particles, measured relative to the direction of the beam axis.

CHAPTER 5

JETS IN HEAVY-ION COLLISIONS

One of the observables that we use to study the QGP is also one of the main signatures for the formation of this new state of nuclear matter. The existence of hard probes, together with the jet quenching phenomenon, allow us to study the system and collect data about its properties and dynamics.

5.1 Hard probes in heavy-ion collisions

In ultra-relativistic collisions, the final state is characterized by the products resulting from the interaction between the constituent partons of the colliding nucleus. Due to the high energies provided by the accelerator's experiments, these partons can directly interact through a process called hard scattering. The interacting partons, which had the momentum pointing initially along the beam direction, scatters with large angles relative to the beam axis and because of this, presents a very high transverse momentum [98].

Together with the high transverse momentum, which provides to the scattered partons a strong penetrating property, the fact that they are created in the initial moments of the collision makes them a powerful tool to probe the characteristics of the medium and its properties. Once an energetic parton is created, it will traverse the medium formed during the collision and will interact with its surroundings along its path. The nature of these interactions will depend on the properties presented by the medium and will be reflected in the final observables. Based on this picture, it is possible to use the products of these hard scatterings as a way to perform a tomography of the system and extract information about its properties. In that context, as the main purpose of this work is related to the phenomenon of jet quenching, we will focus on the concept and study of hard probes that are known as jets.

One of the products that are observed into the detectors after a high energy collision, is given by focused and energetic sprays of particles that we call as jets. These structures emerge from the collision due to confinement effects, which makes the initial parton generated in the hard scattering to fragment into other partons along its evolution and, subsequently, hadronizing in a shower of hadrons. Such a dynamical evolution presents a characteristic conical geometry that is observed in the distribution of the final state hadrons [99] and is illustrated in Fig. 5.1.

Among all types of hard scatterings that can take place in a collision and give rise to a jet event, most of them are characterized by 2 → 2 process, which generates results that are usually called di-jet events. Other kinds of processes such as 3-jets and 4-jets are also possible, always constrained by momentum conservation. Because of that last property, in the case of a di-jet event, it implies that an identified jet should have a partner that presents an angle of approximately 180° relative to its propagation direction [100]. Such a characteristic can be easily observed in the lower panels of Fig. 5.2, particularly in the lower left panel, which shows a real di-jet event measured from a proton-proton collision.

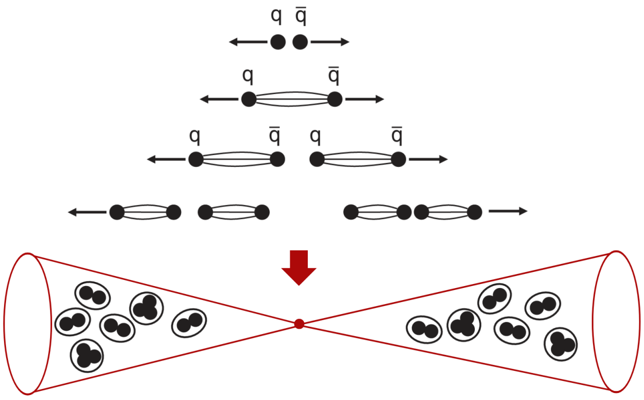

Figure 5.1: Schematic representation of the fragmentation and hadronization process that occurs with energetic partons and leads to a jet formation. In the lower part of the illustration it is sketched the conical geometry observed for jet structure in particle detectors. Modified from Ref. [99].

5.2 Jet quenching

Due to the high energies achieved in the LHC collider, all four experiments: ATLAS, ALICE, CMS and LHCb have measured jet events [98]. The first measurements regarding jet production were published by ATLAS Collaboration [16] and showed an analysis performed on the asymmetry between two identified jets. The asymmetry value A_J measured by ATLAS was defined by comparing both jet energies according to

$$A_J = \frac{(E_{T1} - E_{T2})}{(E_{T1} + E_{T2})}, \tag{5.1}$$

where E_T corresponds to the respective transverse energy of each jet and the index 1 and 2 are used to differentiate the leading and the sub-leading jet, respectively. The first one presents the highest values of transverse energy $E_{T1} > 100$ GeV, while for the second it was considered $E_{T2} > 25$ GeV.

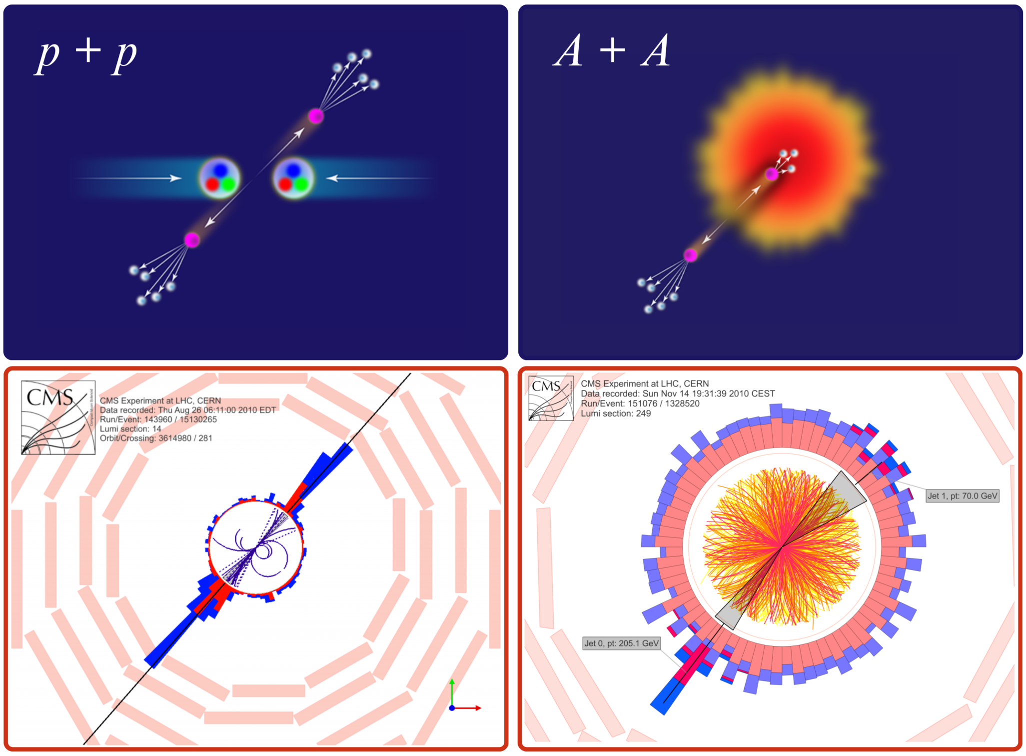

Figure 5.2: Upper panels represents an illustration of a di-jet event being generated in a p-p (left) and A-A (right) collision [101]. In the lower panels it is represented event displays of two collisions measured from CMS Collaboration, in which we have a p+p collision (left) and a Pb-Pb collision (right), both at a center of mass energy of 2.76 TeV [102].

Some of the results from Ref. [16] can be observed in Fig. 5.3, which shows the asymmetry distribution for different centrality classes and also different collision systems. A comparison of the asymmetry distribution measured from p-p events with that from Pb-Pb collisions reveals an increasing difference between the data from the most central events, while seems to be in accordance with the peripheral collisions. This behavior was attributed to the modification of the nuclear medium formed in each centrality class of each collision system. It is interpreted in the area as a direct indication of the jet quenching phenomenon, where a jet created in the initial moments of the collision loses energy to the hot and dense medium through its interaction with the surrounding environment.

When a p-p collision happens, the medium created is very small and as a result, the jets generated in such a system will hardly interact with the medium, leading to a final measure with a very small asymmetry. The left panels of Fig. 5.2 represents that idea with a comparison between an illustration (upper panel) and a real experimental result (lower panel). In the lower panel the colored bars indicate the energy attributed to the measured jets. The magnitude of the bars do not show a significant difference between the leading jet to the sub-leading jet, which is in accordance with the situation illustrated in the upper panel. Both jets experienced the same conditions and then should not present a large asymmetry.

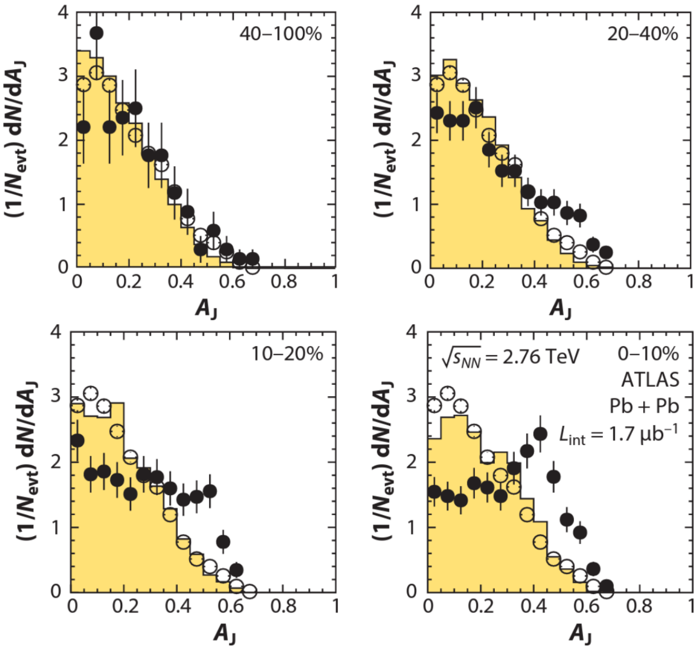

Figure 5.3: Distributions of dijet asymmetry for Pb-Pb (black circles) and p-p (open circles) collisions measured by ATLAS experiment for different collision centralities. The data for p-p events are from collisions at $\sqrt{s_{NN}} = 7$ TeV. The solid yellow histogram corresponds to simulations performed with the HIJING+PYTHIA model [98].

For a Pb-Pb system, the medium formed in central and peripheral collisions are very different. As in the most central events the geometric overlap between the colliding nuclei is large, a jet passing through this system will interact much more with the medium, due to its size. If the di-jet event is created closer to the boundaries of the medium (see the illustration on the right upper panel of Fig.5.2), one of the jets, the leading jet, will traverse a short distance of the fireball and will lose just a small fraction of its energy. On the other hand, its partner jet will have to traverse a large distance inside the medium and will interact for a longer time. As a consequence, it will lose more energy to the medium. The right lower panel of Fig. 5.2 shows an event display with an increased asymmetry when comparing both identified jets, which illustrates using real data the situation described.

Another possible way to quantify the jet quenching phenomenon is provided by the calculation of the nuclear modification factor R_{AA} that can be defined as [103]

$$R_{AA} = \frac{\left[\dfrac{1}{N_{evt}}\dfrac{\mathrm{d}^2 N_{jet}}{\mathrm{d}p_T \mathrm{d}y}\right]_{\mathrm{cent}}}{\left[\langle T_{AA}\rangle \dfrac{\mathrm{d}^2 \sigma_{jet}}{\mathrm{d}p_T \mathrm{d}y}\right]_{pp}} \tag{5.2}$$

where N_{jet} corresponds to the jet yield in Pb-Pb events, while σ_{jet} is the jet cross-section in p-p collisions. The term N_{evt} corresponds to the number of events measured to calculate the R_{AA} and $\langle T_{AA}\rangle$ corresponds to the mean nuclear thickness function, which accounts for the geometric overlap region defined by each centrality class [104].

The measurement of the R_{AA} represents a comparison of the jet yields in nucleus-nucleus collisions with a scaled production of jets in p-p events. A natural and intuitive expectation for the measurement of this quantity is that, in the absence of any influence from the rest of the colliding nucleus, the yields of jet production would scale with the nuclear thickness function, resulting in R_{AA} being close to 1. However, as it can be seen in Fig. 5.4, experimental results of inclusive jets indicate that the jet yield is actually highly suppressed in central events and also presents a small suppression in semi-central events. That observation is in accordance with the results of jet asymmetry discussed earlier.

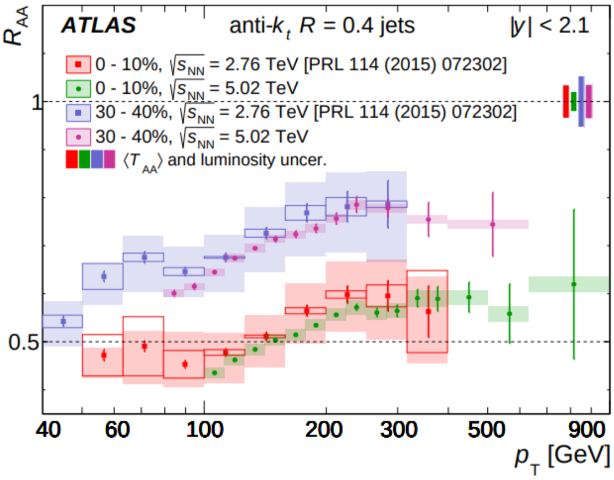

Figure 5.4: Nuclear modification factor R_{AA} as a function of the transverse momentum p_T for measured jets in the ATLAS experiment. The values are shown for two different centrality classes of 0-10% and 30-40%. The error bars correspond to statistical uncertainties and the shaded box corresponds to systematic uncertainties [103].

Both results, jet asymmetry and nuclear modification factor are considered experimental indications of the jet quenching phenomenon and the high opacity presented by the collision medium. This last interpretation, understood as an evidence that the collision medium present a high density property, was predicted as a characteristic for the QGP.

5.3 Jet energy loss

The current understanding of jet quenching suggests that this process is driven by mechanisms similar to the electromagnetic energy loss of charged particles in matter [76,105]. In this context, it is possible to separate the energy loss of jet quenching in two contributions: radiative and collisional processes (See Fig. 5.5).

The radiative energy loss contribution is characterized by medium-induced gluon radiation, which due to its similarity with QED bremsstrahlung is called Gluon Bremsstrahlung [100]. As a result of the multiple scatterings that occurs between the jet and the medium (right panel of Fig. 5.5), which slow down the jets constituents, a fraction of the energy carried initially by the jet is lost in the form of gluon radiation. Due to the nature of that radiation, which also carries color charge, the contribution attributed to the radiative energy loss is regarded as the dominant one in the study of the jet quenching phenomenon [100, 105–107]. In contrast, the collisional energy loss contribution is predicted to be small. That contribution is related to the elastic collisions of the jet constituents with the constituents of the medium [100,105] (left panel of Fig. 5.5). Despite its small contribution to the energy loss phenomenon, the collisional energy loss plays an important role in the study of the medium response to the excitation generated by the propagating jet [100, 108].

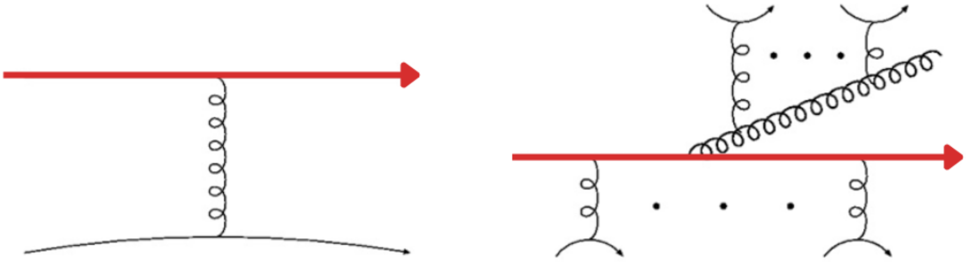

Figure 5.5: Schematic representation of the mechanisms associated with energy loss in the jet quenching phenomenon. The red arrow represents the propagation of a jet constituent. The left panel represents an example of a process that leads to collisional energy loss. The right panel shows multiple curly arrows that indicate the gluon radiation associated with radiative energy loss. Figure modified from Ref. [100].

The medium response is characterized as the consequence of energy and momentum exchanges between the jet and the medium. Due to the collisions attributed to the collisional energy loss, part of the energy lost by the jets is deposited into the medium. Then, for the case in which that energy thermalizes into the medium, it can contribute and affect the medium dynamics, changing not only jet-related observables but also the flow pattern presented by the bulk matter [100]. In the context studied here, the thermalization process can be understood as the mechanism by which the momentum-energy transferred from the jet modifies the medium and reaches the condition of thermal equilibrium with the QGP.

Before continuing to the next chapter, it is important to emphasize the difference between jet quenching and jet thermalization concepts. On the one hand, jet quenching corresponds to the phenomenon of suppression of jets in a nucleus-nucleus collision, which is caused by an energy loss driven by the mechanisms presented earlier. After that, part of the energy lost by the jet and absorbed by the medium will modify the fluid and evolve within the hydrodynamic system, characterizing the process of jet thermalization.

CHAPTER 6

THE MODEL APPLIED

The primary objective of this chapter is to connect all the concepts that were discussed up to this point and show how the proposed model works. Additionally, it will be presented the methodology employed to obtain the results that were presented in the next chapter.

6.1 Jet thermalization through vorticity formation

6.1.1 The vorticity ring

Regarding the hydrodynamic description, a very common phenomenon that can arise in any fluid is the vortex rings structure. In the specific case where the axis of a vortex is defined by a circular closed line, a vorticity ring is created. As a result of that condition, a cylindrical symmetric volume which forms a toroidal figure, analogous to a ring takes form inside the fluid (See Fig. 6.1). Hence the name Vortex Ring. Such a concept is not new in our daily lives and has a very representative example in the smoke rings that we usually see coming out of our mouths when we breathe on a cold day, or also in the structures that are created when a bullet traverses a fluid.

The key physics underlying the formation of vortex rings is represented by the presence of velocity gradients along the radial distance from the center of the ring. While the region in the outer radius of the cylinder presents a relatively small velocity, the central component, which usually receives some external contribution, is large. Such a configuration creates a tendency of the system to rotate around the cylinder axis, generating a vorticity field along that axis line.

Considering a non relativistic case, the natural way of representing and quantifying the vorticity ring structure is by the following relation [22]

$$\mathcal{R}^{\hat{t}}_{NR} \equiv \left\langle \frac{\vec{\omega}_{NR} \cdot (\hat{t} \times \vec{v}_{cell})}{|\hat{t} \times \vec{v}_{cell}|} \right\rangle_{\phi}, \tag{6.1}$$

where $\vec{\omega}_{NR}$ corresponds to the classic definition of vorticity (given by Eq. (3.16)), $\vec{v}_{cell}$ is the velocity of the fluid cell of the medium and $\hat{t}$ is the axis of the ring, which also define its propagation direction. The notation $\langle\cdot\rangle_\phi$ is used to demonstrate that the value $\mathcal{R}^{\hat{t}}_{NR}$ represents an average of the structure over the azimuthal angle about the axis $\hat{t}$.

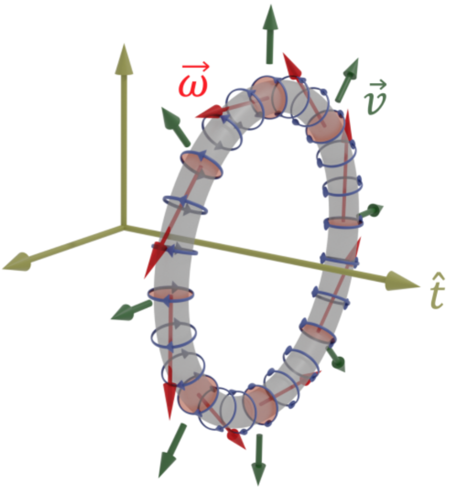

Figure 6.1: Schematic representation of a vorticity ring structure in a general non-relativistic case. In the figure, the red arrows corresponds to the direction of the created vorticity field ($\vec{\omega}$) and the green arrows corresponds to the direction of expansion of the vorticity ring. The oriented blue circles represents the direction of the motion of the medium. Figure from [22].

Now, thinking about the relativistic regime of our study, it is reasonable to consider that an analogous structure could be formed inside the QGP, since it is also described as a hydrodynamic system. We attribute such a phenomenon to the conditions observed in the interactions between a jet and the medium. Due to the momentum exchanges between the jet constituents and the fluid medium, the gradients of momentum created will satisfy the kinematic condition necessary to generate a vortex ring, giving rise to the same toroidal structure inside the QGP. That possibility is illustrated in Fig. 6.2 and shows the situation where a di-jet event is created.

This condition was already evaluated in previous studies of the 3C Collaboration [19,20]. In these works, regarding the vorticity topic, they connected such a property with a final observable by using the spin-vorticity coupling studied in Chapter 4. Since the vortex ring is characterized by a non-zero vorticity field, it is expected for the vorticity created in the thermalization of the energy lost by the quenched jet to induce the polarization of the particles that are emitted from a region near to the ring structure.

The study and identification of vortex rings in the QGP, induced by quenched jets, requires the detection of the quenched jet direction. In that context, one possibility is to measure single jet events, and assume that it corresponds to a scenario similar to the one shown in Fig. 6.2, where only one of the jets was quenched by the medium. Although, another convenient phenomenon that can be addressed to this case is the γ-jet event. In that situation, we have a pair of a photon and a quark (or gluon) being created with high transverse momentum. As the photon does not carry color charge it will not interact with the QGP along its propagation, which allows it to be easily detected and used to set the trigger direction of the quenched jet.

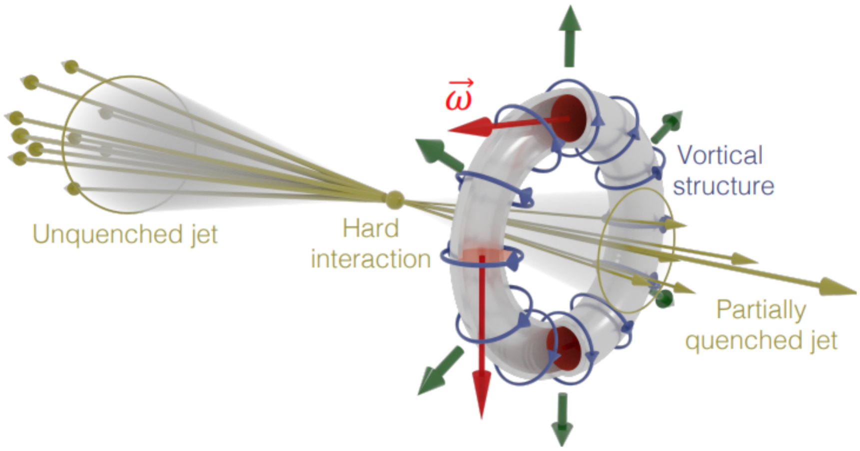

Figure 6.2: Schematic representation of a physical condition that can give rise to a vorticity ring inside the QGP. A di-jet event is observed and while one of the jets is not quenched, its partner is quenched by the strongly interacting medium. As a result, the quenched jet introduces energy and momentum currents in the fluid which will evolve forming the ring [22].

6.1.2 The ring observable

In order to measure the effects caused by the jet thermalization, a new experimental observable was adapted. This observable, which constrain the information about the polarization of the particles with the direction of propagation of the quenched jet, was based on the Eq. (6.1) and on the spin-vorticity coupling. It's mathematical equation represents an extension that can be used to quantify the vorticity ring through the usage of final observables and is expressed as [22]

$$\mathcal{R}_{\Lambda}^{\hat{t}} = \left\langle \frac{\vec{P}_{\Lambda} \cdot (\hat{t} \times \vec{p}_{\Lambda})}{|\hat{t} \times \vec{p}_{\Lambda}|} \right\rangle_{y,p_T}, \tag{6.2}$$

where $\vec{P}_{\Lambda}$ corresponds to the polarization vector of the Λ hyperons, $\vec{p}_{\Lambda}$ is the momentum of the Λ and $\hat{t}$ corresponds to the trigger direction, which in our case is equivalent to the direction of propagation of the quenched jet. Also, in Eq. (6.2), we use Λ's multiplicity as a weight to evaluate the average denoted by $\langle \cdots \rangle_{p_T,y}$, which is performed by a sum over the transverse momentum (p_T) and the rapidity interval (y) of our analysis.

The general picture considered for the analysis of Eq. (6.2), called as Ring Observable is illustrated in Fig. 6.3. Since the polarization of the particles is coupled to the vorticity generated in the fluid, that observable represents a tool that can be used to isolate the circular pattern of Λ polarization that is induced by the vorticity ring created in the thermalization of the energy-momentum currents deposited from a quenched jet.

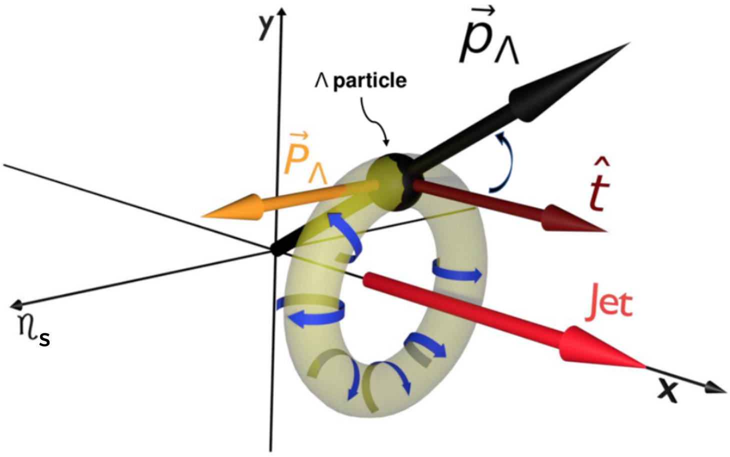

Figure 6.3: Schematic representation of the vector elements involved in the calculus of the ring observable $\mathcal{R}^{\hat{t}}_{\Lambda}$ [20].

6.2 Simulation chain

As we discussed in Chapter 2, the phenomenon of a heavy-ion collision can be divided into distinct steps. The current state of phenomenology in this scenario involves using different phenomenological models to describe each step. Because of this, the simulation chains that we employ to reproduce the real data are usually called hybrid simulation chains. Particularly for the study developed here, we focus our attention on three main stages that are well established in the area and that constitute the necessary stages to reach the observables of our interest. These stages, which are also represented in Fig. 6.4, are: the initial condition, hydrodynamic evolution and particlization.

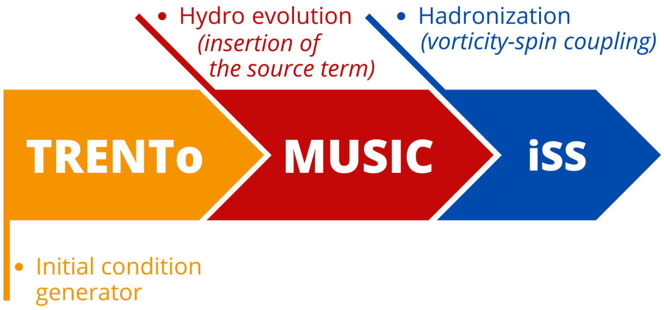

Figure 6.4: Schematic representation of the simulation chain employed to reproduce the results of this work. Each step is referenced by the model used to reproduce the described stage.

6.2.1 Initial condition (T$_\text{R}$ENTo)

In the first step of a heavy-ion collision, we have the characterization of the initial condition generated after the interaction of the colliding nucleus. In our simulation chain, to generate the initial conditions (IC), we utilized the T$_\text{R}$ENTo 3D model (Three-dimensional

Extended Reduced Thickness Event-by-event Nuclear Topology) [109]. That model provides a 3D energy density profile that simulates the deposition of energy due to the interaction of the participant nucleons in the moment of the collision. Based on the impact parameter **b**, which in T$_{\mathrm{R}}$ENTo is always aligned along the x direction, the model selects the nucleons that will interact during the collision, calculating the energy deposition due to its interaction. The nucleons that participate in the collision are called "participants" while those that do not participate are called spectators. That picture is illustrated in Fig. 6.5. The generated profiles change event-by-event, simulating the fluctuations that are predicted for the nucleons' positions inside the nucleus of the ions.

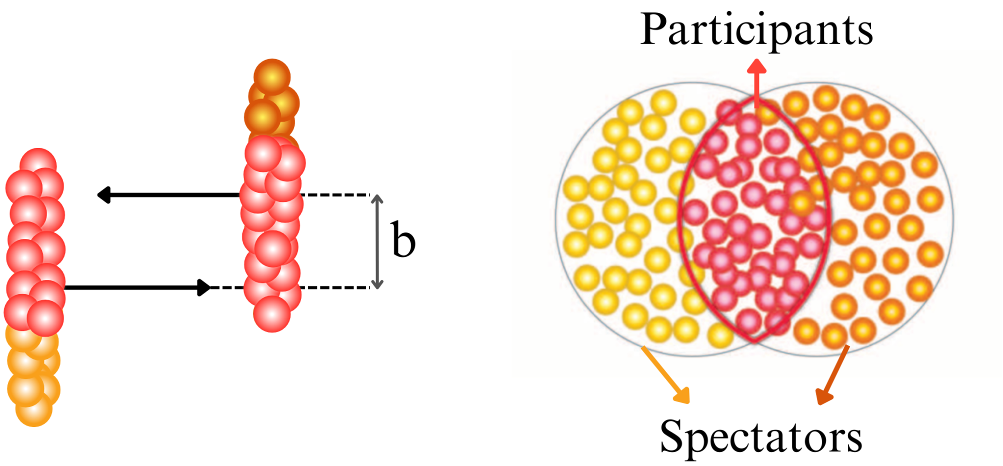

Figure 6.5: The left panel represents the geometric picture of the contracted nuclei that interact in the collisions, considering the $z-x$ plane. The right panel corresponds to a cross section view, in the $x-y$ plane, of the interaction of the colliding ions. Right panel modified from [110]. The colors in both panels differentiates the two ions and the participants and spectators of the collision.

We generated IC's for a collision system created by Pb-Pb collisions at a center of mass energy $\sqrt{s_{NN}} = 2.76$ TeV, using the parameters from Ref. [26, 109]. The parameters common to both 2D and 3D T$_{\mathrm{R}}$ENTo were obtained from Ref. [109], while those exclusive to 3D T$_{\mathrm{R}}$ENTo were taken from Ref. [26]. Table 6.1 explicitly shows the main parameters used to generate the ICs. To ensure numerical accuracy for the simulation, we used a grid spacing equal to $dx = dy = 0.1$ fm in the $x-y$ plane and $d\eta_s = 0.2$ in the space-time rapidity η_s direction.

To complement the analysis performed in Ref. [19], one of the topics that were considered in this work is the accounting for different centrality classes in the collision system. For each centrality bin, we sampled multiple impact parameters b to generate initial conditions using a minimum bias analysis with one million profiles. Then, those profiles were ordered according to the total initial energy of each IC, which is provided by T$_{\mathrm{R}}$ENTo 3D. Considering the relation between the total energy of the initial state and the final particle multiplicity, which is approximated by a linear relation, the centrality classes of those events were mapped in terms of the impact parameter b. The centrality classes applied in this study were defined by the intervals listed in Table 6.2.

Table 6.1: List of parameters used in T$_{\rm R}$ENTo 3D to generate the initial conditions.

	Description	Value
p	Reduced Thickness	0.007
w	Gaussian nucleon width	0.956 fm
-	Skewness type	Relative Skewness
μ_0	Rapidity shift mean coeff.	0.0
σ_0	Rapidity width std. coeff.	2.9
γ_0	Rapidity skewness coeff.	7.3
J	Pseudorapidity Jacobian param.	0.75
d_{min}	Nucleon minimum distance	1.27 fm

Table 6.2: Impact parameter intervals used to define each centrality class.

b (fm)	Centrality (%)
$0.0 - 3.74$	0 - 5
$7.46 - 9.13$	20 - 30
$10.55 - 11.79$	40 - 50
$12.91 - 13.94$	60 - 70

Another topic that is also implemented in this work is the usage of the two types of initial conditions, which we differentiate by using the terms: smooth and lumpy. The difference of both types of initial states is well illustrated by their names and a description of both is given below:

Smooth Initial Condition: is characterized by not presenting the fluctuating properties that were expected from a real collision. The profile is described by a smooth distribution that looks like a Gaussian, as shown in the left panel of Fig. 6.6. This initial state is generated in our study as the result of an average performed over 10,000 fluctuating initial conditions (resulting in a smooth initial condition). The smooth IC is very convenient in order to save computational time in the performed analysis, since for this case the execution of one event is sufficient to obtain satisfactory results of the main behavior presented by the quantities of interest in each study.

Fluctuating (lumpy) Initial Condition: accounts for the fluctuations in the partons positions of the accelerated ions (see the right panel of Fig. 6.6). That profile is the default output of T$_{\rm R}$ENTo 3D model and will differ event-by-event. Because of this, the analysis performed with fluctuations is sometimes called event-by-event (EbE) analysis and also requires the reproduction of several events to obtain consistent results of the final observables. The usage of this kind of initial state, requires a large computational time execution, however it also offers more robust results to compare with experimental data.

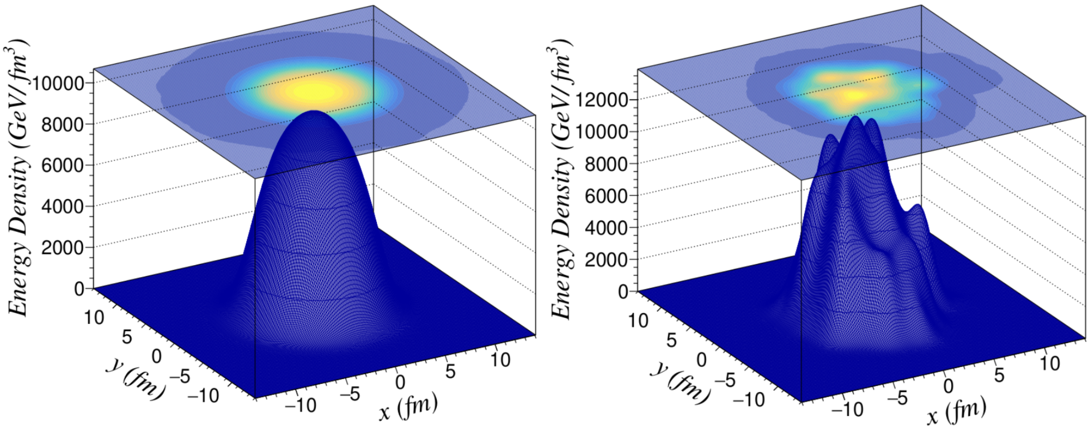

Figure 6.6: Transverse projection of the two types of energy profiles generated by the 3D T$_{\rm R}$ENTo model [109] for the initial condition (IC) of Pb-Pb collisions at 2.76 TeV with 0-5% centrality class. The left panel represents an IC created from an average of 10,000 fluctuating initial conditions, while the right panel shows a typical fluctuating initial condition.

Once the energy distributions of each IC were generated, those profiles were normalized by matching the full simulation results with the experimental midrapidity charged particle multiplicity measured from central (0-5%) events by the ALICE collaboration [111]. A different calibration method was performed for each kind of initial condition (fluctuating and smooth) and the proportionality constant calculated for the 0-5% centrality class was also applied in the peripheral events.

6.2.2 Hydrodynamic evolution (MUSIC)

With the initial conditions ready and calibrated, in the next stage we have the deconfined phase of the collision, which corresponds to the QGP expansion. That phase characterizes the main phase of this work, since it is in there that the phenomenon and effects that we are interested in will occur. In this QGP stage, the energy density profiles of the initial states were hydrodynamically evolved using a viscous relativistic theory which is solved by the MUSIC code [112–114].

This code is responsible for solving numerically the system of mathematical equations that was presented in the last part of Chapter 3. It uses the Israel-Stewart formalism 0 to perform a (3+1)D evolution of the system, which is required for vorticity calculations. We applied the lattice-QCD equation of state derived by the HotQCD Collaboration [115]. Additionally, for the viscosity coefficients, we considered a constant specific-shear viscosity coefficient $\eta/s = 0.08$. That value was kept the same in every simulation performed in this work, except for those expressed in the next Chapter which represents an study of the influence of shear viscosity in the vorticity ring effects. For the bulk viscosity case, due to results presented in Ref. [20], which shows a very small influence of that transport coefficient, we did not included bulk effects in our hydrodynamic simulations. Because of the high energies achieved in the LHC collider, which is the scenario that we are simulating here, we neglected the net baryon density evolution for the QGP fluid dynamics.

In our simulations, we started the hydrodynamic evolution at a longitudinal proper time $\tau_0 = 0.25$ fm/c and let the medium evolve accordingly to the hydrodynamic theory using time steps $\Delta\tau = 0.05$ fm/c. To focus on the polarization effects of our interest, we did not include the configuration required to generate the OAM of the collision, which consequently will not induce a global polarization in our results. The evolution was performed until every cell of the grid reached a thermal freeze-out temperature of $T = 151$ MeV. When this condition was reached, the information of each fluid cell, as energy, temperature, position and time was saved into the freeze-out hypersurface, which was then used in the next step.

Modeling the quenched jet

During the hydrodynamic stage, in order to simulate the dynamics of the energy absorbed by the medium from the quenched jet, a hot source term with well-defined energy and momentum was deposited into the system. In that context, considering the time required for the jet to be created and then quenched by the medium, the jet's energy-momentum currents were deposited directly during the hydrodynamic evolution at a fixed time $\tau_{\rm th} = 1.0$ fm/c.

To characterize the physical properties of the hot source term, we used the same set of parameters that were applied in Ref. [19, 20]. The parameters are described in Table 6.3 and defines not only the values of energy-momentum current deposited by the quenched jet into the fluid medium, but also the size of the hot source term and its initial position of insertion. Similar to what was done for the specific-shear viscosity, we will vary some of those parameters to perform a systematic analysis of the dependence of the polarization induced by the vorticity ring created on them.

Table 6.3: Parameters that characterizes the hot source term that is used to model the energy-momentum currents deposited into the QGP medium by a quenched jet.

Characteristic	Value
Thermalized energy (E_{th})	59.6 GeV
Thermalized momentum (p_{th})	42.3 GeV
Velocity (v_{jet})	$0.7c$
Initial position (x, y, η_s)	$(0, 0, 0)$
Horizontal diameter (R_x)	1.0 fm
Vertical diameter (R_y)	1.0 fm
Longitudinal diameter (R_{η_s})	0.4

In Figs. 6.7 and 6.8 it is possible to see two time steps representing the evolution of the energy-momentum currents of the hot source term (Fig. 6.7) and the induced z-component of thermal vorticity (Fig.6.8). Those results were obtained from a simulation of an event with a smooth initial condition, where the thermalized jet was set to propagate positively in the x direction. The figures show the energy density and vorticity distributions in the center $\eta_s = 0$ slice of the medium, which correspond to the midrapidity region. The distribution of the longitudinal component of thermal vorticity was calculated using $\omega^z_{\text{th}} = \epsilon^{z\rho\mu\nu} u_\rho \varpi_{\mu\nu}$.

Particularly for the left panel of Fig. 6.8, it is possible to observe a vorticity signal generated near to the boundaries of the medium. That contribution of vorticity is associated with the velocity gradients caused by the anisotropic expansion of the system, which despite representing a central collision, still has a certain eccentricity. Once the energy-momentum currents evolves, the right panel of Fig. 6.8 shows, near to the center of the plot, a non-zero signal that is attributed to the vorticity field generated by the thermalization of the hot source term. This result shows a clear ring pattern and represents an indication of vorticity rings being created in our simulations.

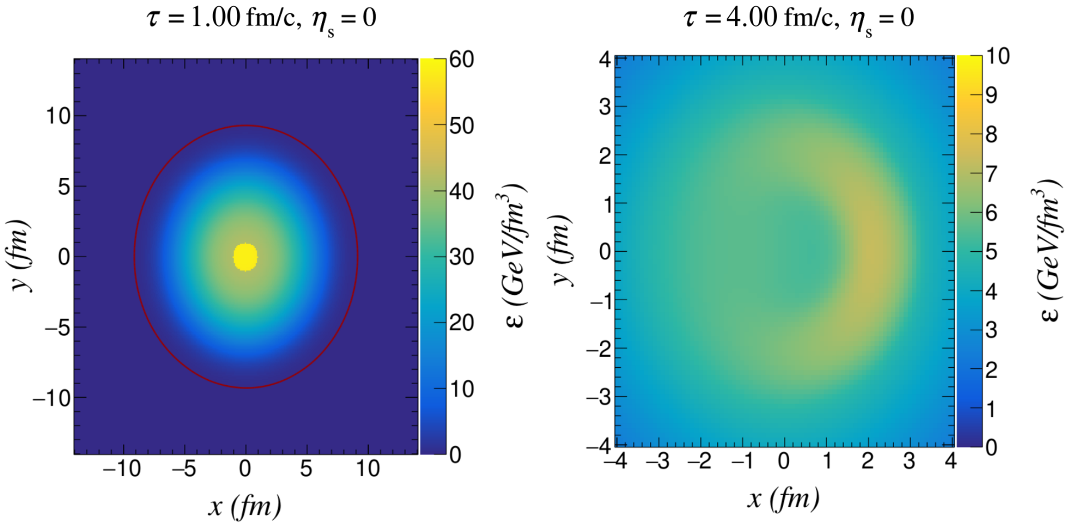

Figure 6.7: Transverse slices at $\eta_s = 0$ of the energy density distribution ε during the hydrodynamic phase for the time steps $\tau = 1.00$ fm$/c$ and 4.00 fm$/c$. The left panel represents the time step where the hot spot simulating the thermalized jet is inserted into the center of the medium. The red solid line corresponds to the position where the freeze-out condition is reached. The right panel represents a zoom of the energy distribution in the region most affected by the energy-momentum currents of the thermalized jet after the evolution of a time interval of $\Delta\tau = 3.0$ fm$/c$.

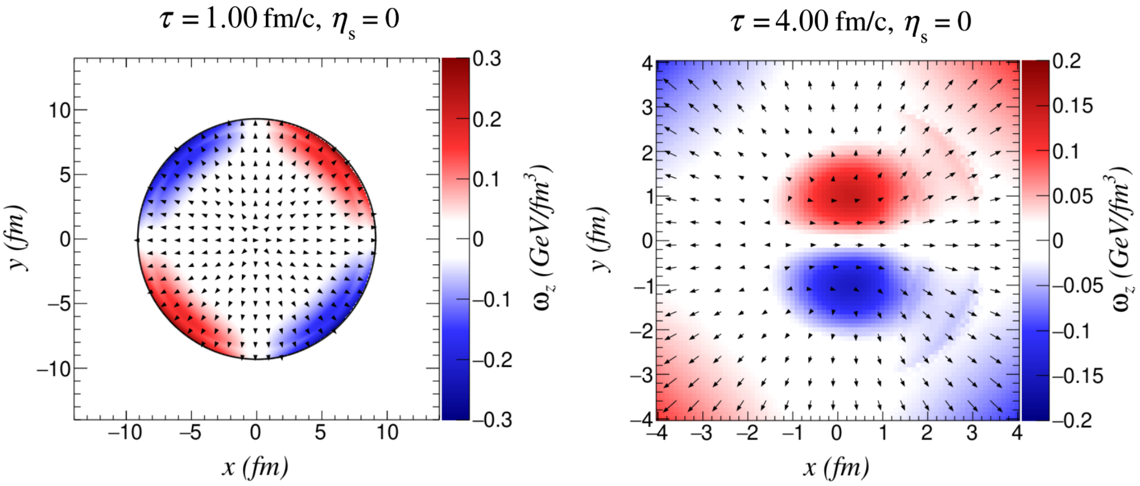

Figure 6.8: Transverse slices at $\eta_s = 0$ of the z component of thermal vorticity ω_z distribution during the hydrodynamic phase for the time steps $\tau = 1.00$ fm$/c$ and 4.00 fm$/c$. The left panel represents the time step where the hot spot simulating the thermalized jet is inserted into the center of the medium. The black solid line corresponds the position where the freeze-out condition is reached. The right panel represents a zoom of the ω_z distribution in the region most affected by the energy-momentum currents of the thermalized jet after the evolution of a time interval of $\Delta\tau = 3.0$ fm$/c$. The black arrows in both panels illustrate the direction of the system's flow.

6.2.3 Particlization (iSS)

After the hydrodynamic phase, the freeze-out hypersurface saved during the fluid dynamics is used to convert the fluid cells to particles via the Cooper-Frye formalism [79, 80]. That process is performed by the iSpectra Sampler code (iSS) [116], which uses Monte Carlo methods together with the Cooper-Frye Formula to provide a momentum spectra of the particles emitted from the simulated medium.

It is during the Particlization phase that the iSS code computes the polarization of the primary Λ hyperons emitted from the hypersurface. The code uses the velocity and temperature information of the hypersurface to determine the thermal vorticity (Eq. (3.18)) associated with each cell. Once this value is obtained, it is used to define the mean spin vector through Eq. (4.3) and then, finally, the polarization vector of Λ hyperons can be computed as

$$P^{\mu}_{\Lambda}(p) = \frac{S^{\mu}(p)}{\langle S \rangle}. \tag{6.3}$$

with $\langle S \rangle = 1/2$ for the case of Λ particles.

CHAPTER 7

RESULTS

Considering the simulation chain and the model for jet thermalization that were presented in the last chapter, we performed several analyses regarding the context of jet insertion and the hydrodynamic response. In order to provide a general picture of the scenario studied, we evaluated not only the effects caused by the vorticity ring, but also the characteristics from events without energy-momentum currents deposited from quenched jets.

7.1 Evaluating the effects of the jet insertion

To assess the consequences of incorporating a hot spot term into the hydrodynamic medium, it is crucial to analyze its impact on the fundamental observables of a heavy-ion collision. While the insertion of the thermalized jet may affect the polarization effects of interest, it is expected that it will not significantly alter other final observables, such as the particle production and the transverse momentum distribution.

Based on this, we performed a comparison of the p_T spectra and mean p_T distribution for both cases: with and without jet insertion. The results for that analysis are presented in Fig. 7.1 and were obtained considering a scenario with fluctuating initial conditions with 40-50% centrality class. The angle ϕ_J that defines the direction of propagation of the inserted jet in each event was randomly selected from an interval $[0; 2\pi)$. For reasons that will be fully discussed in Section 7.3.6, it was preferred to focus this initial analysis in semi-peripheral events. The main motivation for this choice is the comparison between the magnitude of the background energy density in central and peripheral events. As the energy density decreases for peripheral initial conditions, the insertion of the jet in that scenario leads to more evident energy-momentum currents, which consequently should generate stronger influences.

The left panel of Fig. 7.1 shows the p_T spectra of charged particles for both scenarios with (in red) and without (in blue) the insertion of the thermalized jet. The lower left panel represents the *jet/no jet* ratio. It is possible to observe that, in terms of the number of produced particles, the effects due to the insertion of the jet increases with the transverse momentum. In the limit of $p_T = 3.0$ GeV the increase in particle yields becomes of the order of 10%. Despite that, since most of the produced particles are in the low p_T region, the insertion of the jet does not significantly change the general picture of particle yeld.

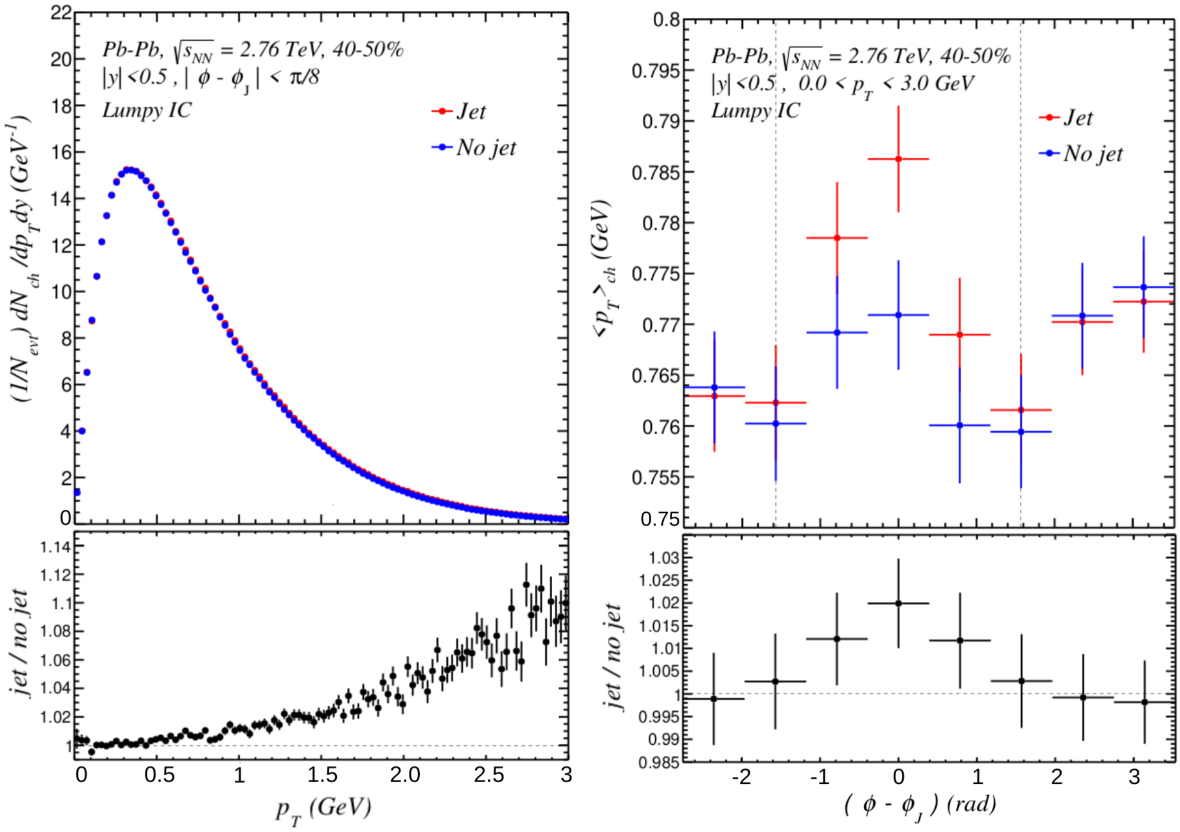

Figure 7.1: (Left) p_T spectra of charged particles measured in the direction of propagation of the thermalized jet ($|\phi - \phi_J| < \pi/8$) for both analysis with (red points) and without (blue points) jet insertion. The lower panel corresponds to the ratio of particle yields comparing both scenarios. (Right) Values of mean transverse momentum $\langle p_T \rangle_{ch}$ measured for charged particles as a function of the azimuthal angle relative to the direction of the thermalized jet. The dashed lines in the upper panel indicate the directions perpendicular to the jet. The lower panel shows the ratio of measurements with and without jet insertion. These results were obtained from fluctuating initial conditions (Lumpy IC) of Pb-Pb collisions at 2.76 TeV and 40-50% centrality class.

The right panel of Fig. 7.1 shows the mean transverse momentum measured as a function of the azimuthal angle relative to the direction of propagation of the thermalized jet. In the case of events without jet insertion, the angle ϕ_J for the analysis was selected to align with the corresponding jet direction in events in which the jet was inserted. As expected, the insertion of the jet in the hydrodynamic medium affects the mean p_T distribution by increasing the $\langle p_T \rangle$ in the direction of the thermalized jet. This is confirmed by the larger values represented with red markers. For the analysis without any jet insertion, the results and error bars indicate that the values of $\langle p_T \rangle$ are consistent with a constant distribution. Looking to the lower right panel of Fig. 7.1, which shows the *jet/no jet* ratio for that analysis, it is possible to observe that the effect of increasing the mean transverse momentum presents a small magnitude, of the order of 2% in the direction of the jet.

In conclusion, the analysis presented in Fig. 7.1, demonstrates that the insertion of the thermalized jet into the hydrodynamic medium does not have a significant impact on the final observables of the system. The same analysis in the scenario of central events (0-5%) reveals changes on the order of less than 1%. Ultimately, our results indicate that the insertion of the jet can be visualized as a small perturbation in the medium.

7.2 Analysis on the polarization distribution

We evaluated the dependence of the z-component of the Λ polarization vector in the lab frame on the transverse momentum and the azimuthal angle. The intervals analyzed correspond to the pseudorapidity $|y| < 0.5$ and transverse momentum $p_T < 3.0$ GeV. The pseudorapidity interval was selected to match the usual acceptance observed in particle experiments, while for the transverse momentum, the interval of analysis takes into account the validity range of hydrodynamic simulations.

7.2.1 Events without jet insertion

In the analysis of events simulated without jet insertion we used both types of initial conditions described in Chapter 6: the smooth and lumpy initial conditions. The polarization of the Λ particles along the longitudinal direction (P^z_Λ), obtained from both analysis, are presented in Fig. 7.2, with the azimuthal axis presented relative to the reaction plane angle Ψ_{RP}. The left panels of Fig. 7.2 presents the polarization obtained from a single event simulated using a smooth initial condition generated to present a mean geometry equivalent to 0-5% (top panel) and 40-50%(bottom panel) centrality class. The right panels show the polarization of 250 lumpy events generated using the impact parameter range of Table 6.2 that defines the 0-5% (top panel) and 40-50% (bottom panel) centrality classes.

It is possible to observe that in all the analysis presented in Fig. 7.2 the distribution of polarization on the azimuthal axis presents a qualitative agreement regarding the distribution structure. For the cases in which the polarization is obtained from events simulated with lumpy IC's, the signal presents some fluctuations that start to dilute in peripheral events, where the magnitude of the signal is larger. It is also possible to see an increase of the magnitude of polarization with respect to the transverse momentum.

The polarization structure observed in Fig. 7.2 shows the characteristic quadripolar pattern observed in literature and discussed in Chapter 4. That pattern is usually attributed to a polarization induced by the anisotropic expansion of the system. In order to further analyze this point and reinforce such an interpretation, Fig. 7.3 shows the results of the polarization signal integrated in transverse momentum for events simulated with smooth initial conditions and assigned to different centrality classes.

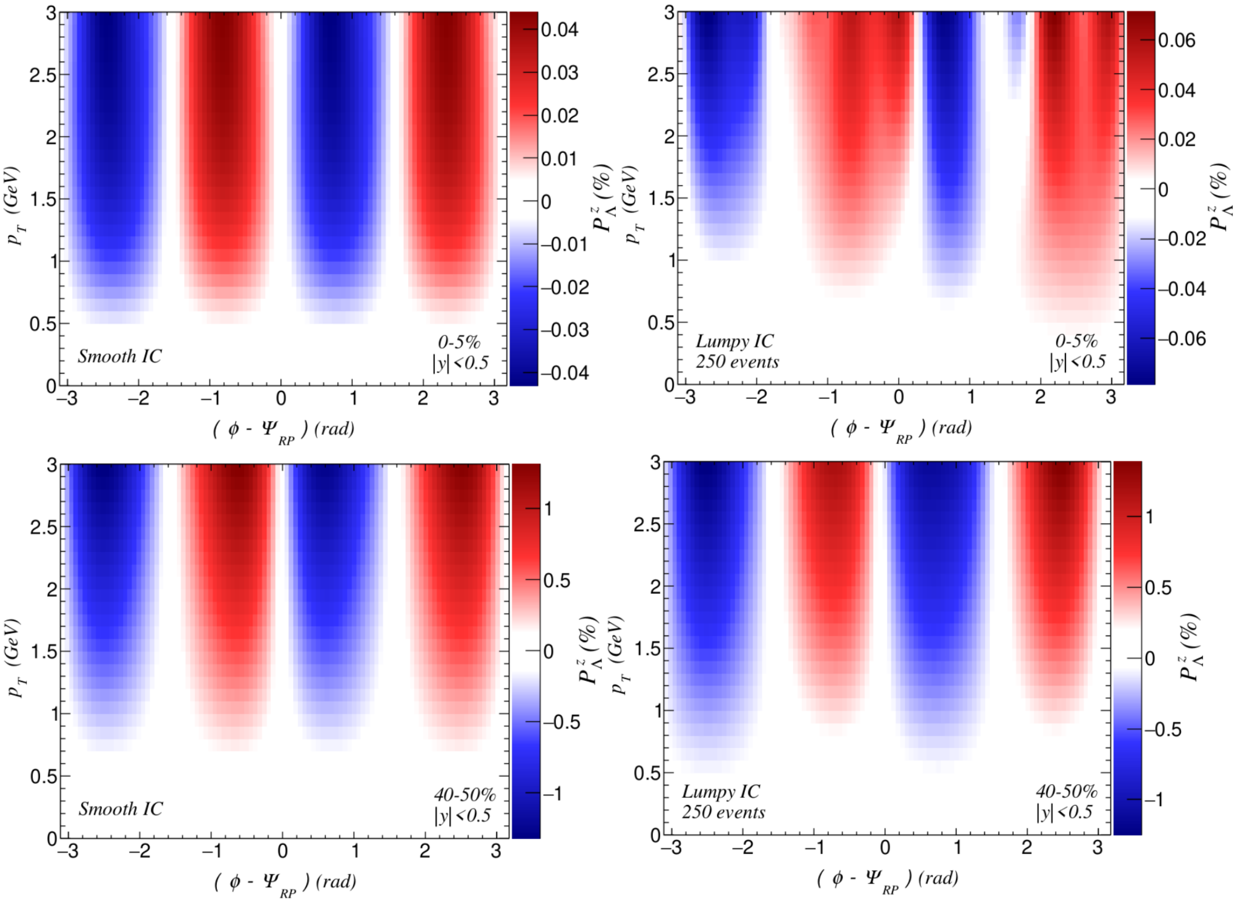

Figure 7.2: P^z_Λ as a function of transverse momentum p_T versus relative angle $\phi - \Psi_{RP}$ for different initial conditions and centrality bins. The top panels correspond to central events in the 0-5% centrality class and the bottom panels to semi-peripheral events of centrality 40-50%. The right panels correspond to results obtained from an event-by-event analysis obtained from 250 fluctuating initial conditions and no thermalized jet was inserted during the hydrodynamics evolution. The left panels represent the results obtained from an analysis where the averaged initial condition was employed and no thermalized jet was inserted. The angle Ψ_{RP} represents the orientation of the reaction plane.

The quadripolar pattern remains present for all centrality bins and the magnitude of the polarization increases for peripheral events. That behavior is analogous to the behavior observed for the elliptic flow measured by v_2 coefficient [90]. The geometry of the collisions, which leads to an anisotropic expansion in the transverse plane, can also generate local vorticity fields that later will induce the polarization of the particles emitted from the collisions. That idea is represented in the right panel of Fig. 7.3. The increase in magnitude can be attributed not only to the increased elliptical flow of peripheral events but also to the shorter lifetime of the system created, which makes the system to freeze-out in a moment when the vorticity field is stronger.

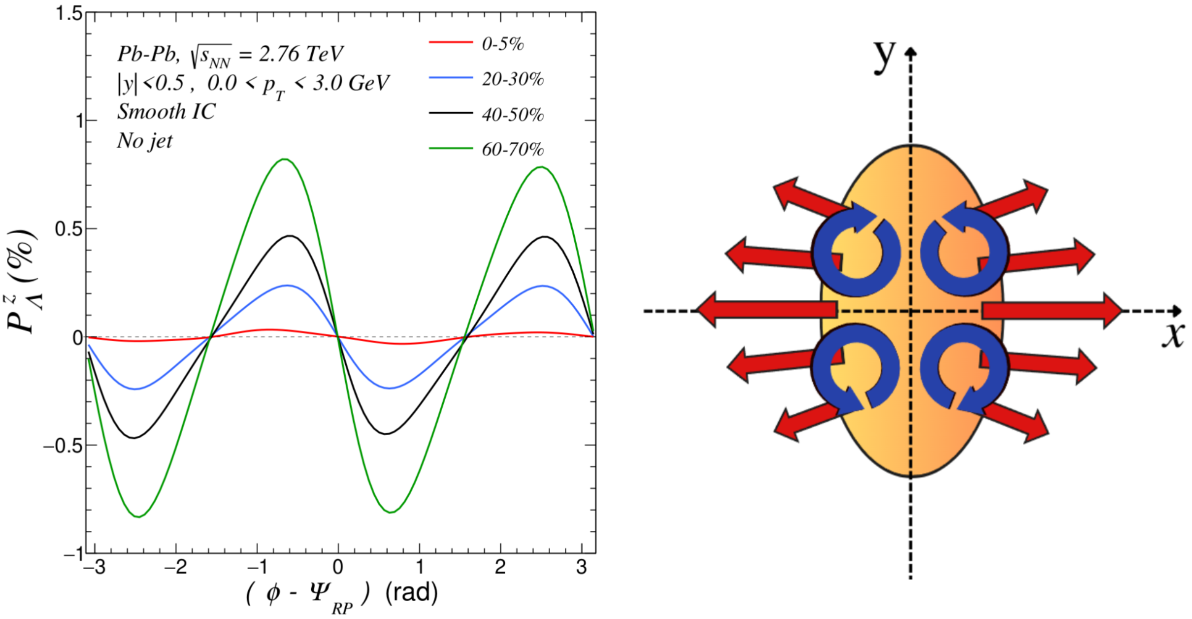

Figure 7.3: (Left) Polarization of the z component of vorticity (P^{Λ}_{z}) as a function of the azimuthal angle relative to the reaction plane for different collision centralities. (Right) Schematic representation of the local vorticity generated by the transverse expansion of the system.

It is clear from the results shown here that the expansion of the system without any jet insertion already induces a polarization signal, as it was expected from our discussion in Chapter 4. However, the polarization due to the background expansion is always aligned with the reaction plane and the jet direction will not be aligned. Thus, if the polarization is measured with respect to the jet direction and not the event reaction plane, the contribution to the polarization from the background expansion will average out. For this reason, in the following studies we varied the direction of propagation of the thermalized jets in the event-by-event analysis performed with lumpy initial conditions.

Results from a more detailed analysis of the polarization induced by the anisotropic expansion of the medium is presented in Appendix A. This analysis includes the contributions for the expansion in the longitudinal and in the transverse direction. We also included a study that explores different novel proposals for the spin-vorticity coupling used in the particlization step of the simulation chain. We show that, depending on the specific model employed, it is possible to discriminate between the polarization contributions originating from the transverse and longitudinal expansion.

7.2.2 Events with simulated jet thermalization

For this analysis, the jet energy and momentum was deposited at the center of the system $x = y = \eta_s = 0$. The azimuthal direction of propagation of the thermalized jet (ϕ_J) will depends on the method of simulation employed: in the case of an event-by-event analysis, the direction ϕ_J was randomly selected from uniform distribution using the interval $[0, 2\pi]$ with rapidity $y = 0$. In contrast, for events simulated from a smooth initial condition, the direction of propagation of the deposited energy and momentum currents is set along x axis, pointing in the positive direction, which is equivalent to $\phi_J = 0$. Figure 7.4 illustrates what was just described, sketching the directions of the jet over a representation of the respective types of initial condition.

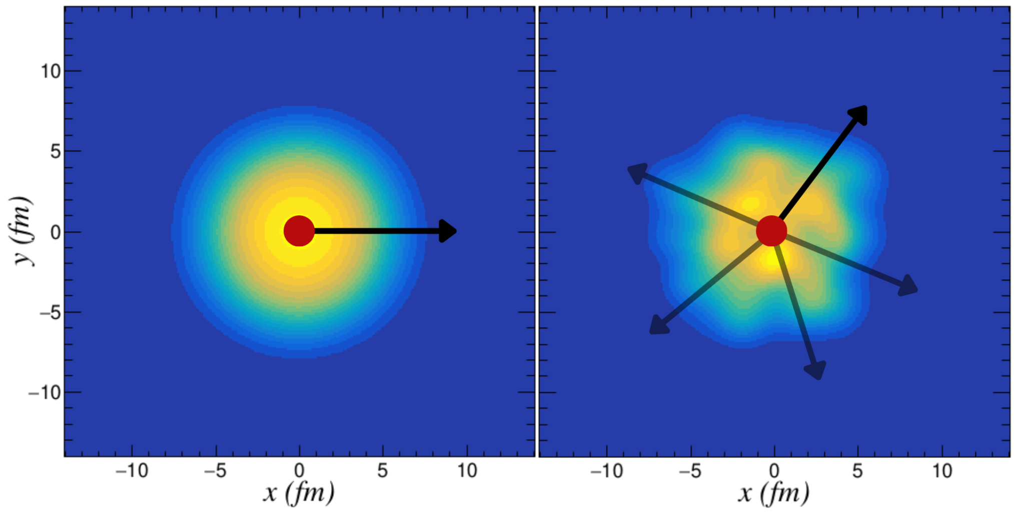

Figure 7.4: Illustration of the direction of propagation for the thermalized jet in each type of simulation performed. In the left panel, which represents the simulation of a single event using the smooth initial condition, the direction of the jet is set to $\phi_J = 0$. The right panel represents the situation of the event-by-event analysis performed with the simulation of lumpy initial conditions, in which the direction of the jet is random.

The results from both cases (event-by-event and smooth) and also both centrality bins (0-5% and 40-50%) can be observed in Fig. 7.5. The azimuthal angle of the polarization pattern is measured relative to the direction ϕ_J of the jet. The top panels of Fig.7.5 represent the results obtained from central events in 0-5% centrality class while the bottom panels correspond to results from semi-peripheral events in 40-50% centrality class. The left panels represent results from a smooth initial condition and the right panels represent the polarization averaged from 250 events simulated from lumpy initial conditions.

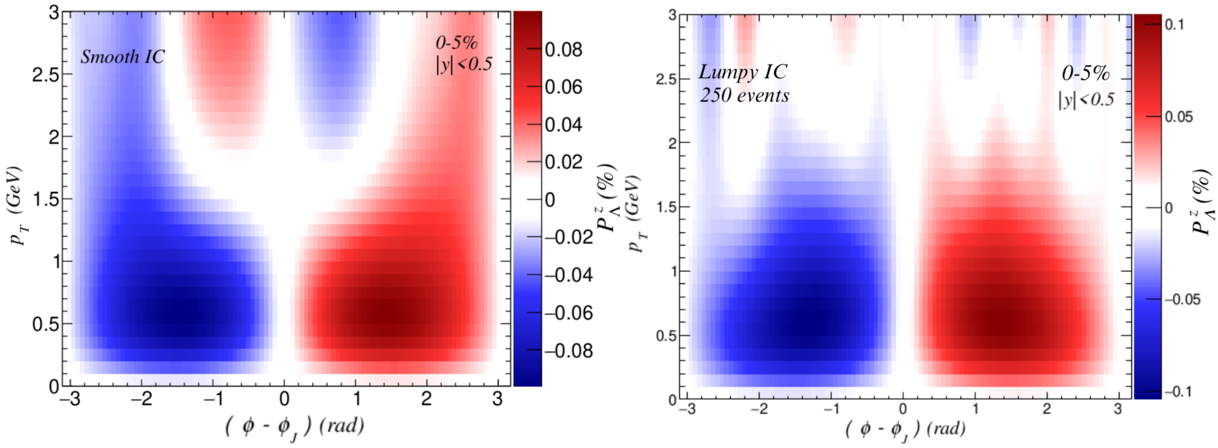

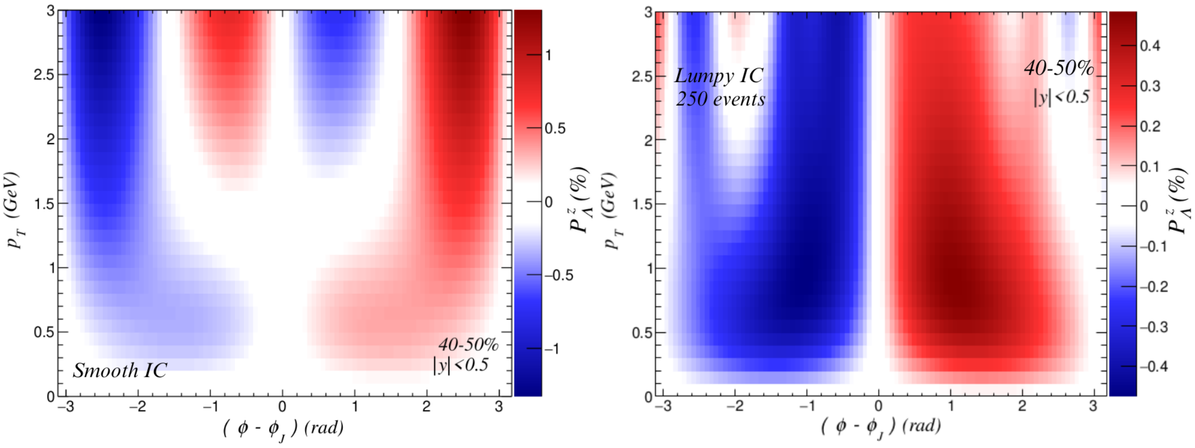

Figure 7.5: P^z_Λ as a function of transverse momentum p_T versus relative angle $\phi - \phi_J$ for different initial conditions and centrality bins. The top panels correspond to central events in the 0-5% centrality class and the bottom panels to semi-peripheral events of centrality 40-50%. The right panels correspond to results obtained from an event-by-event analysis with 250 fluctuating initial conditions and the insertion of the thermalized jet during the hydrodynamic evolution in the center of the system. In the event-by-event analysis the direction of the thermalized jet was chosen at random for each simulated event. The left panels represents the results obtained from an analysis where one averaged initial condition was employed and the thermalized jet was inserted in the center of the system, pointing towards the direction of positive x-axis.

The color gradient presented in the plots of Fig. 7.5 indicates that in all the analysis performed, except by the smooth analysis on 40-50% centrality class (bottom left panel), the longitudinal polarization vector P^z_Λ is concentrated in a region with $p_T < 1.5$ GeV, and its magnitude reaches a maximum around $|\phi - \phi_J| \sim 1.5$ rad. In the bottom left panel of Fig. 7.5, despite the presence of the thermalized jet, the large contribution from the anisotropic expansion of the background dominates, and thus, the signal from the jet is more difficult to see. In the both left panels, which represent the results from smooth initial conditions, it is possible to observe a signal in the high p_T region which we attributed to the influence of the expansion of the medium. In the right panels, the same region appears with a small magnitude signal that we understood as a result of the method applied in varying the direction of the thermalized jet. It is clear that the right top panel of Fig. 7.5 still shows some small signals in $p_T > 2.5$ GeV. However these signals were attributed to a statistical fluctuation which survived the randomization method applied in the direction of the momentum of the thermalized jet.

7.3 Systematic study on the ring observable

Once the polarization distribution on the scenarios of our interest is well understood, from this point forward we will focus on the signal calculated using the Ring Observable equation (6.2). For this, we choose the trigger direction $\hat{t}$ for the analysis as $\hat{t} = \hat{J}$, with $\hat{J}$ corresponding to the propagation direction of the energy-momentum currents deposited from the quenched jet.

To focus on the region of the signal that can be attributed to the jet, we keep the pseudorapidity range $|y| < 0.5$ and set the transverse momentum range $0.5\ \mathrm{GeV}/c < p_T < 1.5\ \mathrm{GeV}/c$, since it is the region that appears to be most affected by the thermalization of the jet, as seen in Fig. 7.5. The upper limit was selected to minimize the contributions from the anisotropic expansion, while the lower limit considers the experimental acceptance.

7.3.1 Fluctuations on ring observable

In the first analysis of the ring observable, we evaluated the influence of the initial condition fluctuations on vorticity ring effects. In Fig. 7.6, we compare the results obtained from event-by-event simulations and those from an event-averaged smooth initial condition. The scenarios for each analysis are the same as those applied in the polarization study performed in the last section. The event-by-event results were obtained from 250 fluctuating initial conditions with impact parameters sampled in the 0-5% centrality class. In both cases, the hot spot simulating the thermalized jet was deposited at the center of the system, *i.e.* $x = y = \eta_s = 0$.

The solid lines in Fig. 7.6 correspond to the results obtained when the energy-momentum current is deposited, and the dashed lines to the scenario where no source terms from the jet were inserted. The shaded area in the plot represents the statistical error associated with each point. This error, calculated for the event-by-event analysis, was obtained through the application of the Jackknife method [117]. As discussed earlier, we see a small but non-vanishing signal generated by the anisotropic flow. In the event-by-event scenario without jets, since the jet direction and the reference direction (in the case of no jet) were randomized, we see an almost vanishing signal for $\mathcal{R}^J_\Lambda$, which is expected from our previous discussion on background polarization.

Regarding the signal generated by the quenched jets, we see that the smooth initial condition scenario is qualitatively similar to the more realistic event-by-event simulations. Based on that comparison, simulations with event-averaged initial conditions can provide a good estimate for the ring observable and characterizes a great opportunity to perform exploratory analysis in scenarios with central events. The quantitative difference between both scenarios is attributed to the influence of transverse expansion. Since the signal obtained with the smooth initial condition was not averaged over different trigger directions, the resulting signal (blue solid line in Fig. 7.6) will present a great contribution from the background expansion (blue dashed line in Fig. 7.6).

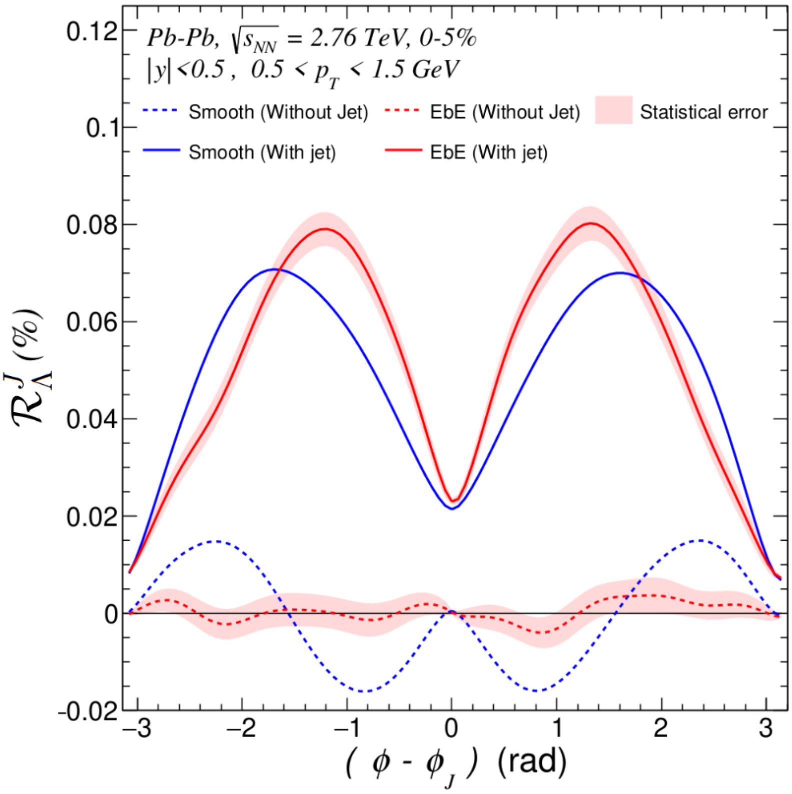

Figure 7.6: The ring observable $\mathcal{R}_{\Lambda}^{J}$ as a function of the relative azimuthal angle $(\phi - \phi_J)$ for event-by-event (in red) and smooth (in blue) initial conditions and with (solid lines) and without (dashed lines) the energy-momentum deposition from thermalized jets.

7.3.2 Viscosity scan

The specific shear viscosity η/s of the medium is an important transport coefficient in the hydrodynamic scenario to modeling the QGP. It characterizes the resistance of the fluid to shear flow and because of this is expected to present a high influence in the study of hydrodynamic phenomena. In this section, we investigate the influence of different values for the specific shear viscosity on the jet-induced ring observable $\mathcal{R}_{\Lambda}^{J}$.

Based on the comparisons shown in Fig. 7.6, simulations conducted with smooth initial conditions can provide a good estimate for the ring observable. With this in mind, we performed the study on shear viscosity coefficient using the event-averaged smooth IC. For these simulations, the energy-momentum current from the quenched jet was deposited to the hydrodynamic medium at $x = y = \eta_s = 0$, with the direction of the momentum pointing to the positive x direction. The results of our scan analysis are presented in Fig. 7.7. The left panel of Fig. 7.7 shows the azimuthal distribution of the Ring Observable calculated from events simulated with different specific shear viscosity values. A clear ring pattern can be observed in all evaluated conditions and it is also possible to see that the maximum magnitude achieved in the peaks for each curve shows that the signal increases with decreasing specific shear viscosity. These results are in qualitative agreement with those from the previous work [19].

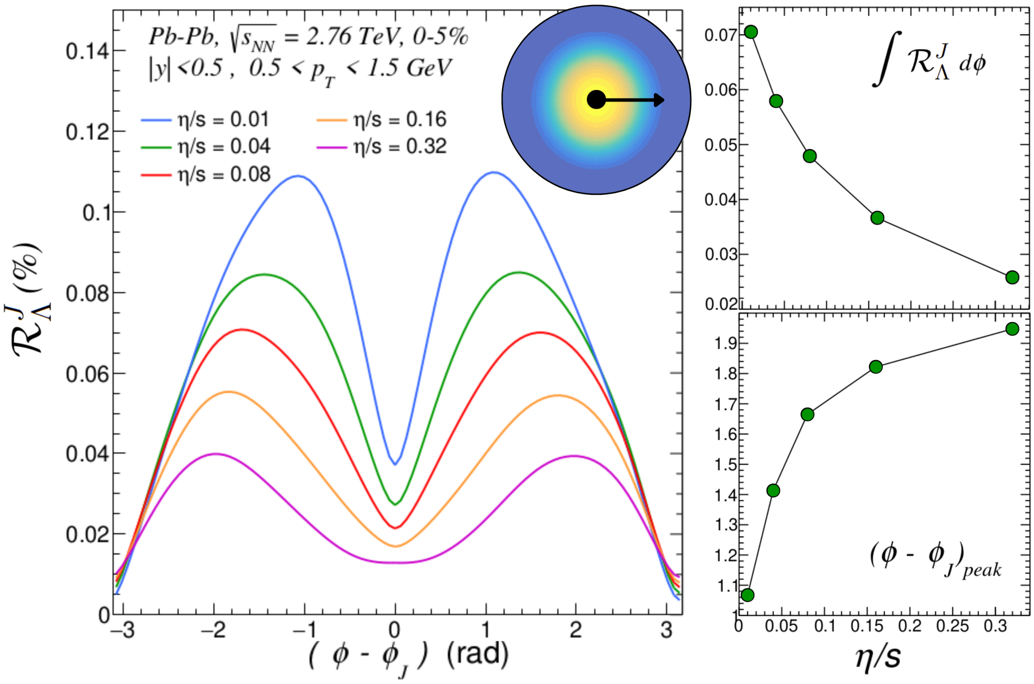

Figure 7.7: In the left panel it is represented the ring observable $\mathcal{R}^J_\Lambda$ as a function of the relative azimuthal angle $(\phi - \phi_J)$ for different values of specific shear viscosity of the medium. The illustration inside the plot represents schematically the scenario studied, in which we applied a smooth initial condition and inserted the energy-momentum current from the quenched jet at the center of the event with momentum pointing in the positive x axis. The top right panel corresponds to the azimuthal integrated $\mathcal{R}^J_\Lambda$ as a function of the specific shear viscosity. The bottom right panel represents the opening angle of the peaks observed in the left panel as a function of the specific shear viscosity of the medium.

A deeper analysis of that signal is also presented in the right panels of Fig. 7.7. The upper right panel represents the azimuthal integrated $\mathcal{R}^J_\Lambda$ for each curve in the left panel. The integrated signal decreases monotonically with increasing specific shear viscosity presenting a non linear behavior for the trend. The lower right panel shows the opening angle of the peaks in the left panel. It is possible to see that the opening angle increases monotonically and in a non-linear way with increasing specific shear viscosity.

Our result indicates that increasing the viscosity of the medium leads to a reduction in the polarization induced by the thermalization of the jet energy. Such a trend can be comprehended within the hydrodynamic framework, where the larger viscosity value prevents the system from developing the velocity gradients required to generate the vorticity ring. As a consequence of this, the vorticity field induced in the system will be weaker and, in turn, will lead to a weaker final hadron polarization.

7.3.3 Velocity scan

In Fig. 7.8 we explore the dependence of the ring observable $\mathcal{R}^J_\Lambda$ on the velocity assigned to the thermalized jet. For this, we used

$$v_{\text{jet}} = p_{\text{jet}}/E_{\text{jet}}, \tag{7.1}$$

where $v_{\text{jet}} = 0.4c$, $0.7c$, $0.8c$, and $0.9c$. In this relation, we fixed the mass of the jet $E_{th} = 59.6$ GeV to match the value employed in Ref. [19] and calculated its momentum p_{th} according to each velocity value.

We performed these calculations with a smooth initial condition in the 0-5% centrality class. The energy-momentum current in this case was inserted at the center of the system ($x = y = \eta_s = 0$) and the velocity assigned to the jet was always pointing positive in the x direction.

The left panel of Fig. 7.8 shows the azimuthal distribution of the ring observable obtained for each different velocity value. A ring pattern is visible for all the curves and the peaks of each analysis increases in magnitude with velocity value. The upper right panel shows that the azimuthal integrated signal increases with the jet velocity while the lower right panel indicates that the opening angle decreases. As the momentum of the deposited energy-momentum current increases, an interplay between the higher velocity gradients and the shorter time to reach the freeze-out hypersurface drives the signal to show an increased magnitude in the final polarization. Both reasons lead to a stronger vorticity field reaching the freeze-out surface, which, in turn, produces a stronger polarization along the vorticity ring.

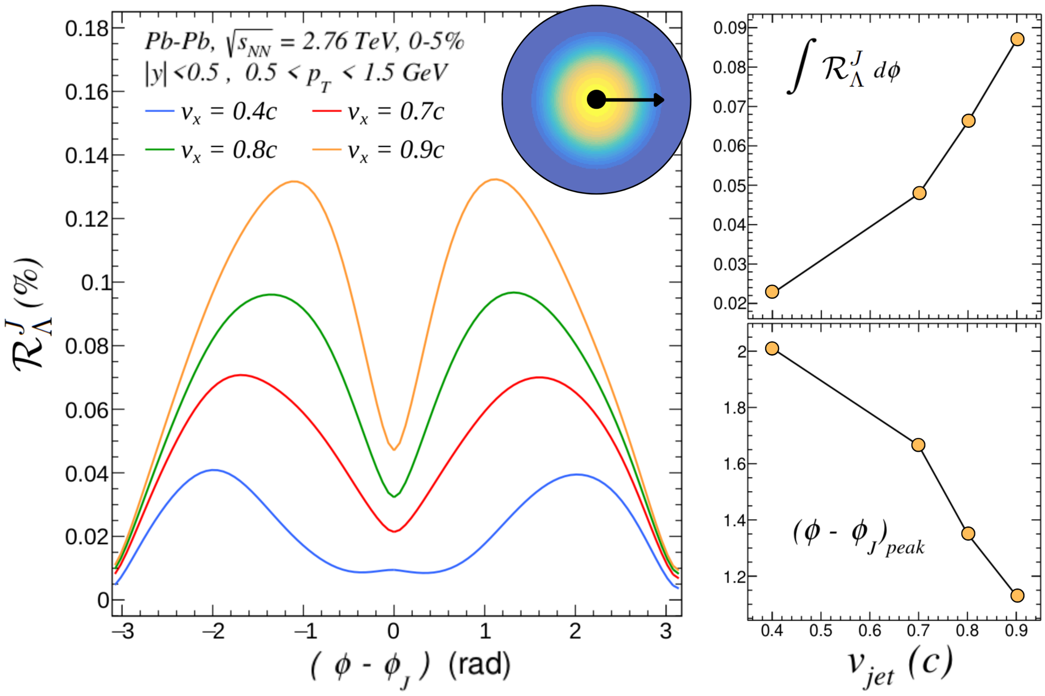

Figure 7.8: The left panel show the ring observable $\mathcal{R}^J_\Lambda$ as a function of the relative azimuthal angle $(\phi - \phi_J)$ for different values of the velocity assigned to the thermalized jet. The illustration inside the plot represents schematically the scenario studied, in which we applied a smooth initial condition and inserted the energy-momentum current from the quenched jet at the center of the event with momentum pointing in the positive x axis. The top right panel represents the azimuthal integrated $\mathcal{R}^J_\Lambda$ as a function of the jet's velocity. The bottom right panel shows the opening angle of the peaks observed in the left panel as a function of the jet's velocity.

7.3.4 Position scan

The main objective of this section is then to evaluate how different initial positions for the deposited energy-momentum current would influence the signal of the ring observable. In this case, to account for the fluctuations in the IC profile, we simulated 250 events using lumpy initial conditions with one energy-momentum deposition per event. The centrality classes applied for this study were central (0-5%) and semi-peripheral (40-50%) Pb-Pb collisions.

The results of our analysis can be observed in Fig. 7.9 and Fig. 7.10, where the ring observable is represented as a function of the relative azimuthal angle to the jet direction ($(\phi - \phi_J)$). For the analysis performed in this section, the method of varying the direction of propagation of the thermalized jets was employed, which means that ϕ_J was chosen randomly from an interval of $[0, 2\pi)$ in each event. We set a radius R and defined three different values $R = 0,\ 2,$ and 4 fm to indicate the distance of the point where the energy-momentum currents were deposited from the center of the system. At this point, we kept the direction of the jet always aligned with the radial direction, thus, either inward or outward following the expansion of the system. Results from 0-5% are presented in Fig. 7.9 for both inward (left) and outward (right) scenarios. Figure 7.10 shows the equivalent results for event centrality 40-50%.

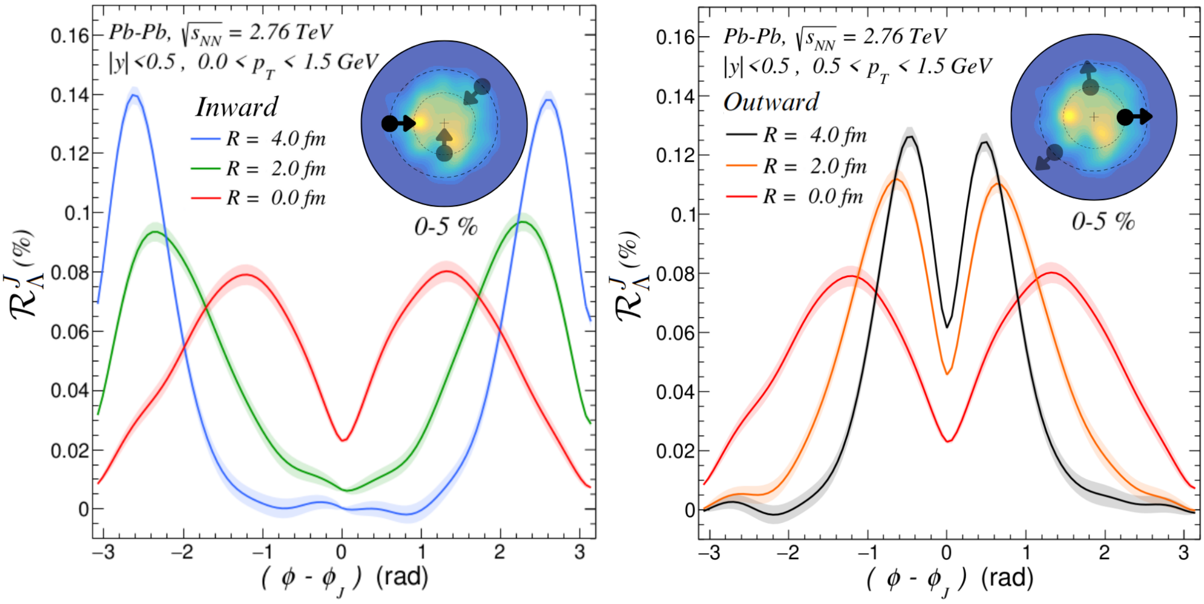

Figure 7.9: $\mathcal{R}^J_\Lambda$ distribution for different positions in the 0-5% centrality class. In both panels, the thermalized jet is inserted in the medium in a position defined by the radius $R = 0,\ 2$ and 4 fm. The direction of the jet ϕ_J was chosen at random. In the left panel, the direction of the energy-momentum currents deposited from the thermalized jet points inward, towards the center of the event. In contrast, in the right panel, the thermalized jet points outwards from the center. The illustration inside the plots represents schematically the scenario studied for different positions of insertion.

Results in Figs. 7.9 and 7.10 show two notable features: first, the maximum values of the ring observable $\mathcal{R}^J_\Lambda$ increases with the R distances of the energy-momentum deposition. Secondly, the distance between the peak angle, also shows a strong dependence on the positions of the jet energy deposition. Those behaviors are mainly attributed to the distance of the jet insertion position to the freeze-out hypersurface and also to the evolution direction of the vorticity ring created.

When the jet is inserted with a large R and points outward from the center, the perturbation that induces the creation of the vorticity ring structure is already closer to the freeze-out surface. Since the velocity gradients induced by the jet presents the largest magnitude at their insertion times and decrease with the hydrodynamic evolution, when they are created closer to the boundaries of the medium, the time available for those gradients to decrease is shorter, which leads to a strong velocity gradients, and consequently, stronger vorticity fields in the moment they reach the freeze-out condition. Regarding the angular distance between the two maxima, for the outward scenario, the opening angle is smaller because of the shorter evolution time available for the vorticity ring to expand in the medium. In the case where the jet insertion was done propagating inwards towards the center, the thermalized jet propagates in a direction that opposes the system expansion, hence, the induced velocity gradients are much larger and they will counterbalance the magnitude of the signal with the longer evolution time. For this case, the velocity gradients will reach the freeze-out surface with a greater contribution in a region behind the jet, which can be seen in the peak angles that are close to $(\phi - \phi_J) = \pi$ or $-\pi$.

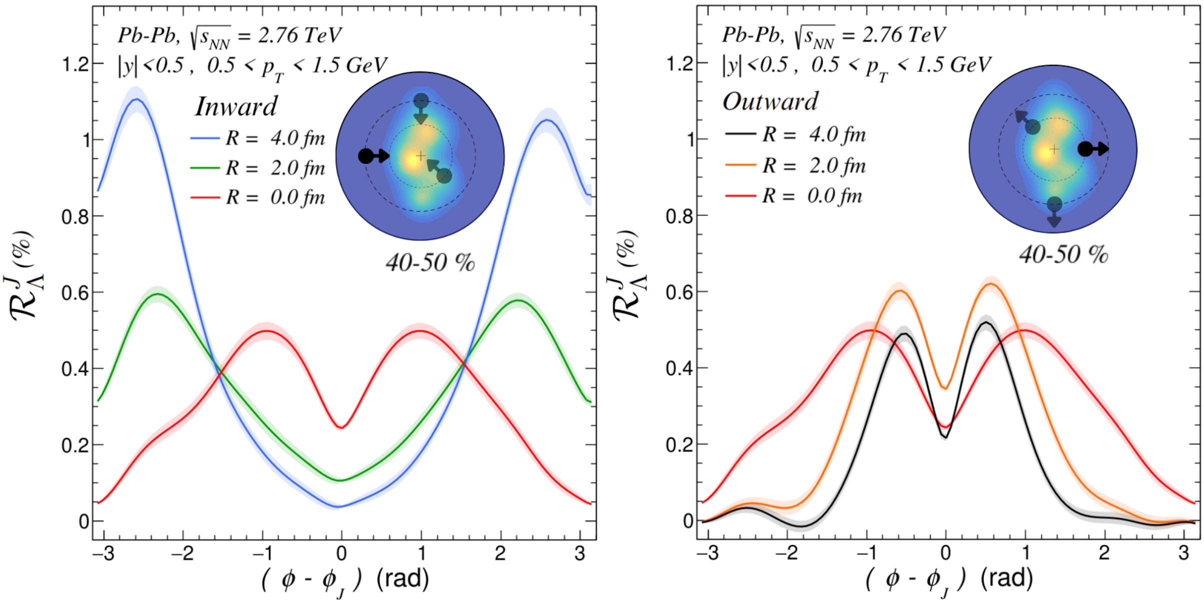

Figure 7.10: $\mathcal{R}^J_\Lambda$ distribution for different positions in the 40-50% centrality class. In both panels, the thermalized jet is inserted in the medium in a position defined by the radius $R = 0,\ 2$ and 4 fm. The direction of the jet ϕ_J was chosen at random. In the left panel, the direction of the energy-momentum currents deposited from the thermalized jet points inward, towards the center of the event. In contrast, in the right panel, the thermalized jet points outward from the center. The illustration inside the plots represents schematically the scenario studied for different positions of insertion.

In addition to that interpretation, the right panel of Fig. 7.10 shows a different behavior in comparing the magnitudes of the results represented by the curves for $R = 4$ fm and $R = 2$ fm. For that comparison, the amount of matter that will hydrodynamically interact to form the vorticity ring seems to play an important role. As in peripheral events the magnitude of the background is already lower, when the jet is inserted in a position that is very close to the boundaries of the system, it is expected that the interaction of the thermalized jet with that region of the fluid to be small, since there is not enough matter to create a well defined vorticity ring structure. Consequently, the induced vorticity field decreases and the polarization induced in the particlization stage is weaker.

An evaluation of the integrated signal and averaged opening peak angle can be observed in Fig. 7.11. The left panel of Fig. 7.11, shows the azimuthal integrated signal for each scenario and both centrality bins. In the central case (lower panel), the integrated signal shows a maximum for $R = 0$ fm and decreases monotonically in each scenario with increasing the R value, however, the variation is small indicating that overall, the integrated polarization is not affected by the jet insertion position. For the case of semi-peripheral events, the integrated signal shows a qualitative agreement to the results observed by the peaks of the azimuthal distribution of $\mathcal{R}^J_\Lambda$.

In the right panel of Fig. 7.11, we show the behavior of the opening angle of the peaks in $\mathcal{R}^J_\Lambda$ azimuthal distribution. Considering that in the inward scenario the ring evolves backwards to the jet, the measure of the ring size in that case should be represented by the distance of the opening angle to $-\pi$ direction. With this in mind, the trend observed for both scenarios in the right panel of Fig. 7.11 shows that the ring size increases monotonically with decreasing the R values. Such a behavior is also related to the time interval available for the ring to evolve and expand in the system.

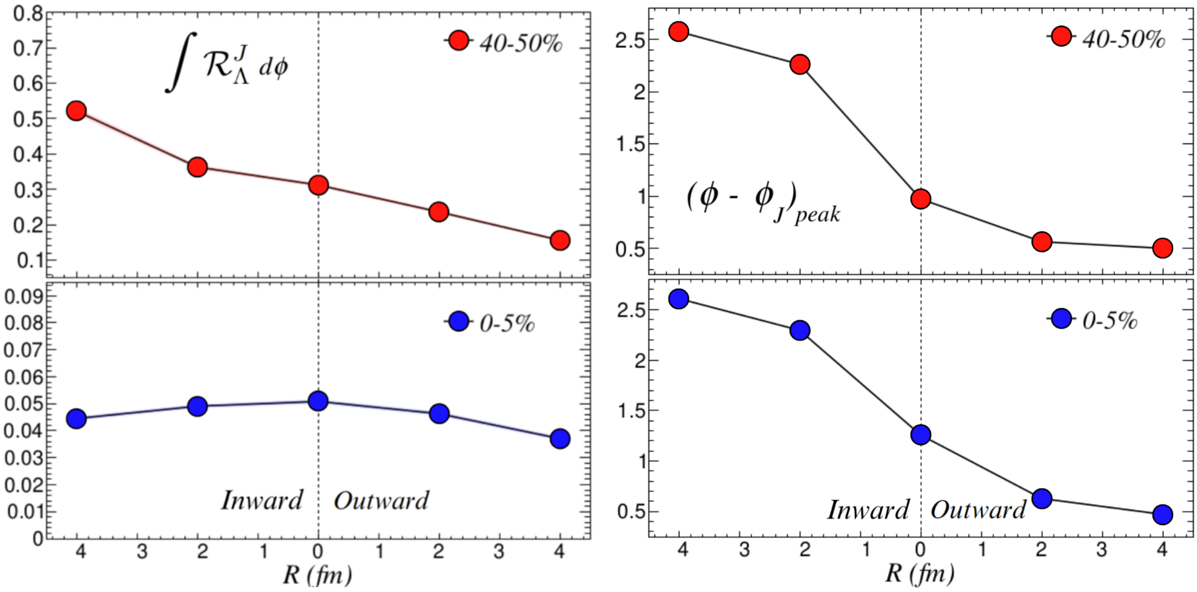

Figure 7.11: The left panel shows the azimuthal integrated $\mathcal{R}^J_\Lambda$ as a function of insertion position of the thermalized jet for the two different scenarios (inward and outward) and different centrality bins. The right panels show the opening angle of the peaks observed in Figs 7.9 and 7.10 as a function of insertion position of the thermalized jet for the two different scenarios (inward and outward).

Sorted Position Analysis

Still considering the influence of the insertion position for our model of jet thermalization, it is possible to argue that the position where a jet is absorbed by the medium is not experimentally accessible and would vary in an event-by-event analysis. A complete analysis of that scenario should account for jets being produced in any part of the medium and propagating with a direction that should vary in each event. In that context, the best scenario for a hard interaction, which represents the origin of a jet, should be in the hot regions with highest energy levels of the initial conditions.

To address this scenario, we insert the thermalized jet into the hydrodynamic medium with a momentum oriented along the $\hat{x}$ direction and varied the positions of the energy-momentum deposition from the quenched jets, considering a probability distribution in the x-axis. That probability distribution was obtained from the normalized energy profile along x direction, defined by $y = 0$ fm and $\eta_S = 0$ for each fluctuating initial condition, which serves as a proxy for the distribution of binary collisions.

Figure 7.12 shows the ring observable as a function of the relative azimuthal angle $(\phi - \phi_J)$ for 0-5% (left panel) and 40-50% (right panel), from the analysis where the jet insertion position was varied randomly along the x-axis. The red curves correspond to the ring observable calculated from events where the jet was inserted, and the blue curves to the background results, *i.e.* without the jet's energy-momentum deposition. Since in this analysis the method of varying the direction of propagation of the jet was not employed, the results referenced as "Jet", presents a great contribution due to the background expansion. Additionally, the size of the vorticity ring varies in each event due to the variation in the position of the jet insertion. Because of this, the pattern of a characteristic vortex ring is no longer visible. For the results where no energy-momentum currents were inserted, the signal of the background is dominated by the anisotropic expansion contribution. The larger magnitude observed in peripheral collisions can be attributed to the more intense anisotropy generated during these collisions and to the shorter lifetime of the QGP created.

The main message of this analysis is that, even with a more realist scenario, considering the binary collision distribution and also a non-vanishing influence of the transverse expansion, the final signal calculated through $\mathcal{R}^J_\Lambda$ is sensitive to the effects of the vortex rings created and can be easily differentiated from the signal of events with no jet.

7.3.5 Jet's alignment

In the search for accurately representing a realistic scenario in our model for jet thermalization, a final remaining variable that needs to be explored is the addition of random directions for the propagation of the thermalized jet. This is an important feature to analyze because, in all results presented up to this point, we assumed that the direction of the thermalized jet was always in the radial direction aligned with the expansion of the system. However, in reality, it is plausible for the jet to exhibit a different orientation relative to the flow axis. To investigate the effects of misalignment between the jet energy-momentum current and the underlying flow velocity, we conducted event-by-event calculations, fixing the insertion position of the energy-momentum current of the quenched jet at $x = 2$ fm, $y = 0$ fm and $\eta_s = 0$. Then, to break the jet-medium alignment we varied the jet's azimuthal angle (ϕ_J) in each of 180 fluctuating events by an interval of $0 < \phi_J < 2\pi$ with a space of $\Delta\phi = 2\pi/180$. This analysis was performed considering a semi-peripheral collision system in 40-50% centrality class.

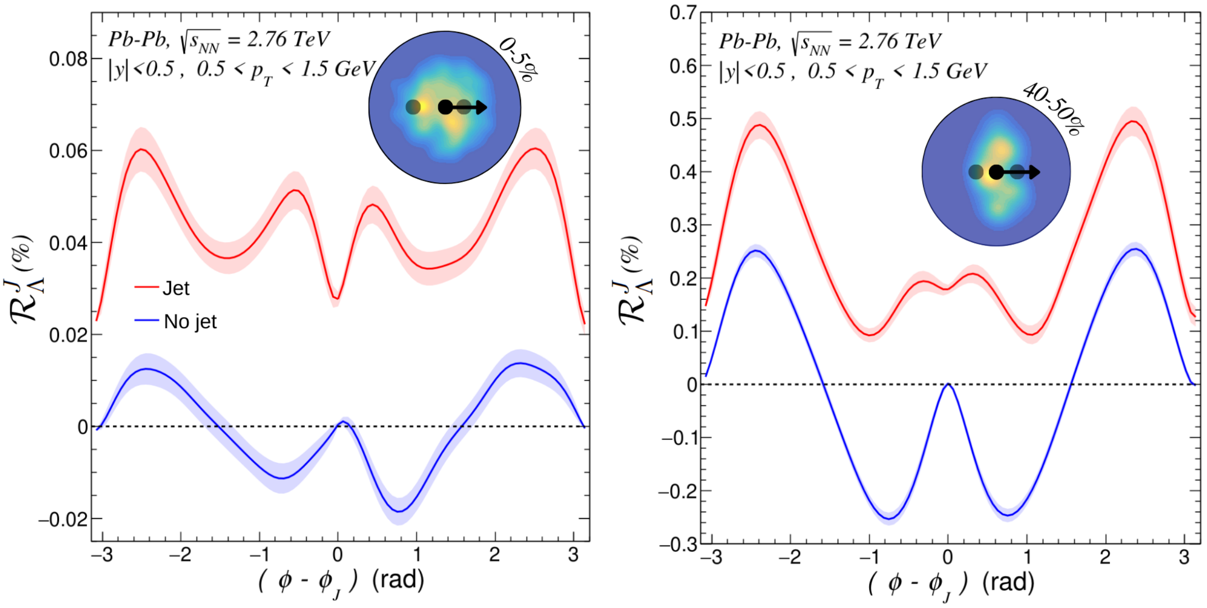

Figure 7.12: $\mathcal{R}^J_\Lambda$ as a function of the azimuthal angle relative to the jet's direction for two different centralities: $0-5\%$ (left) and $40-50\%$ (right). For these results, the position where the jet is inserted was chosen at random according to the normalized entropy distribution of the central slice projected into the x-axis ($y = 0$ fm and $\eta = 0$) of each initial condition profile. In this analysis the direction of the thermalized jet is always pointing positive along the x axis.

The results of this analysis are shown in Fig. 7.13, presenting the ring observable as a function of the relative azimuthal angle for two scenarios: one with jet-medium alignment (represented by blue curves) and the other with jet-medium misalignment (represented by green curves). The comparison between both results shows clearly that for the case of jet-medium misalignment there is a significant decrease in the magnitude of the averaged signal of the ring observable. Additionally, the distinct ring pattern observed in the previous analysis is absent in this case.

The azimuthal-integrated signal obtained from the misaligned jet analysis yields a value of $\mathcal{R}^J_\Lambda = 0.1282 \pm 0.0110$ (%). This resulting signal corresponds to approximately 41% of the signal compared to the scenario when the jet is inserted at the center of the system and the jet's momentum is aligned with the flow velocity. Such a decrease can be assigned to the deformation of the toroidal structure of the vortex ring, caused by the different configurations between the ring's expansion direction and the direction of medium's flow. Figure 7.14 presents some of the possible configurations that constitute the analyzed signal. As a consequence of the deformation, the ring pattern of vorticity that induces the polarization of the hyperons is destroyed, which becomes clear by looking at a later evolution time shown in the lower panels of Fig. 7.14. While the left panel shows a well-defined pattern for the vorticity created in the thermalization of the energy-momentum currents of the jet, the center and right panels show a highly deformed pattern for the vorticity distribution. Nevertheless, despite the significant decrease, it is noteworthy to emphasize that the signal remains nonzero and possesses a measurable magnitude for $\mathcal{R}^J_\Lambda$.

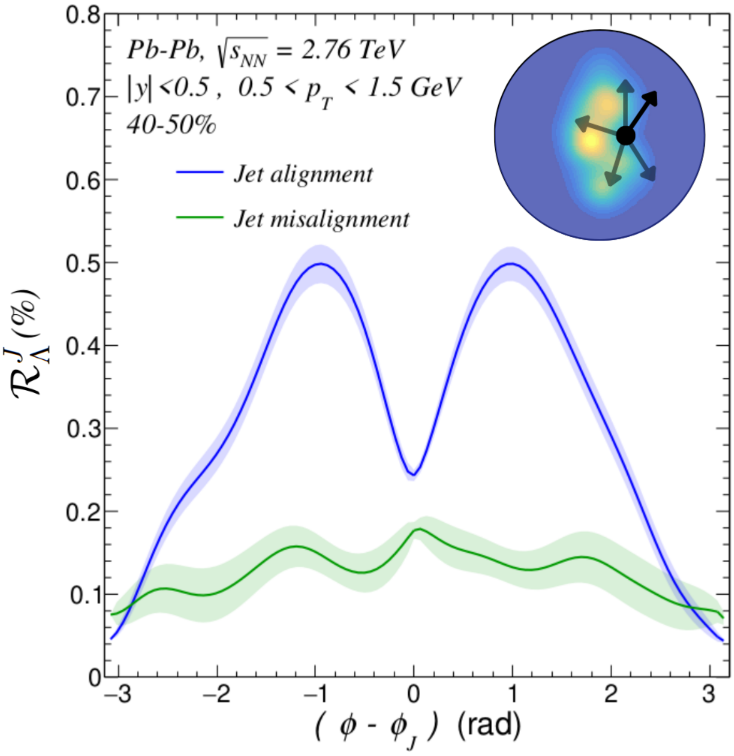

Figure 7.13: $\mathcal{R}^J_\Lambda$ as a function of the azimuthal angle relative to the jet's direction for two different scenarios where the jet is aligned (blue solid line) and misaligned (green solid line) with medium's flow. These results correspond to an event-by-event analysis performed using fluctuating initial conditions in the $40-50\%$ centrality class.

7.3.6 Centrality scan

To conclude our analysis on the vorticity ring formation, we now investigated the influence of the centrality class of the collision system on the integrated value of $\mathcal{R}^J_\Lambda$. This analysis has the purpose of consolidating our previous results from Figs. 7.6, 7.9, 7.10 and 7.12, which were already performed considering different collision centralities. We also added a new centrality class of 60-70% to the scenarios studied before. The simulation procedure was the same as explained in the respective sections where each result was discussed individually.

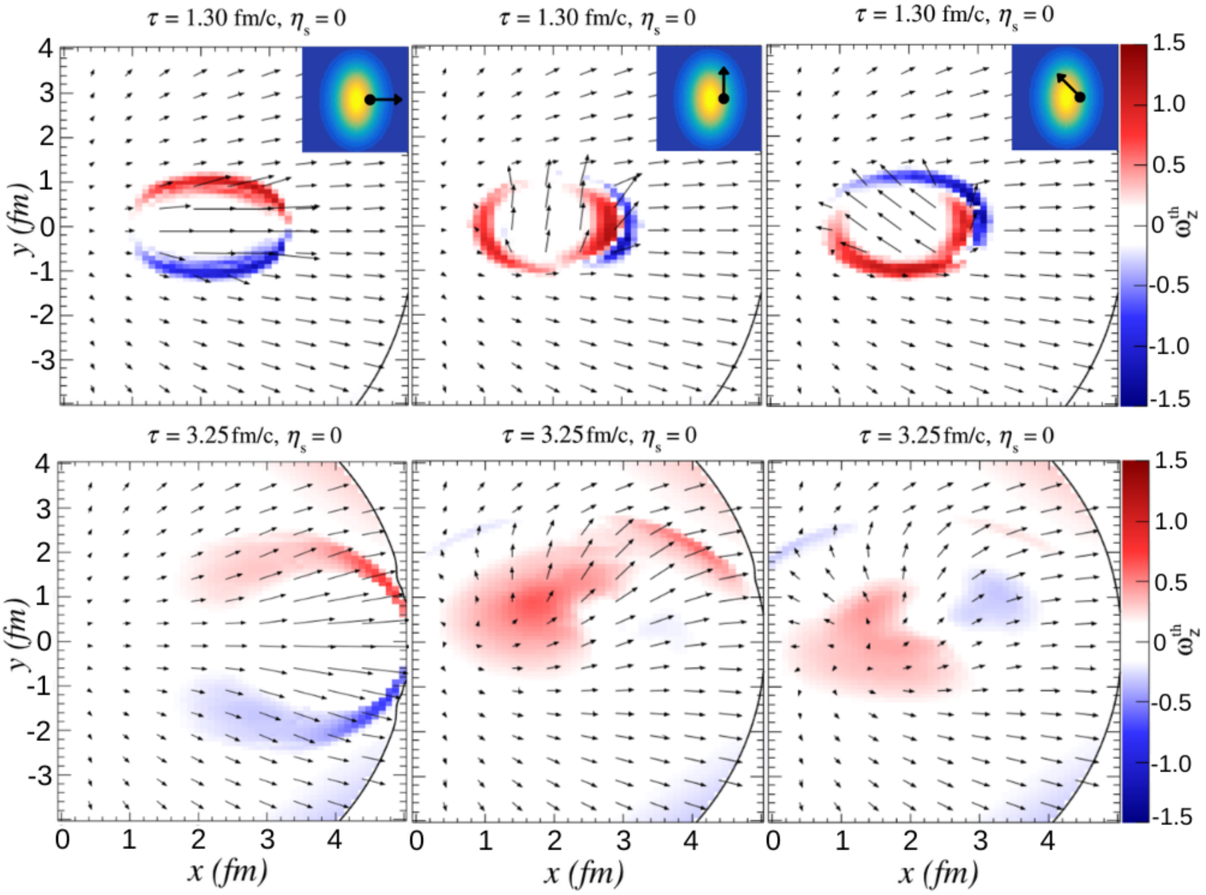

Figure 7.14: Vortex ring formed by the energy-momentum currents of the thermalized jet for time steps $\tau = 1.30$ fm/c and $\tau = 3.25$ fm/c of the hydrodynamic evolution. The panels show the spatial distributions of the z-component of the thermal vorticity, $\omega^z_{\text{th}} = \epsilon^{z\rho\mu\nu} u_\rho \varpi_{\mu\nu}$, at midrapidity. The arrows indicate the fluid's transverse velocity. For all the results, the energy-momentum currents were inserted at $y = 0$ fm and $x = 2$ fm in a smooth initial condition in 40-50% centrality class. In the upper panels, there is an insert scheme to represent the orientation of the jet inside the event. The left panel represents the evolution of the vorticity generated by a thermalized jet with momentum pointing positive in the horizontal axis ($\phi_J = 0$). The central panels represent the evolution of the vorticity generated by a thermalized jet with momentum pointing positive in the vertical axis ($\phi_J = \pi/2$). The right panel represents the evolution of the vorticity generated by a thermalized jet with momentum oriented by an angle of $\phi_J = 3\pi/4$ rad relative to $+\hat{x}$ direction. The black solid line present in the plots corresponds to the freeze-out surface.

Figure 7.15 presents the azimuthal-integrated ring observable as a function of the impact parameter b for the different scenarios of energy-momentum deposition from the quenched jets. The red and blue points in Fig. 7.15 represent the mean of the results obtained from the event-by-event analysis, and the error bar corresponds to the statistical error of the values obtained. The points in the same centrality bin are slightly offset from each other in the b axis for clear visualization. The first case, labeled as *$R = 0$ fm (fluc. IC)*, represents the azimuthal-integrated signal of the $\mathcal{R}^J_\Lambda$ in the scenario $R = 0$ studied in Fig. 7.9 and Fig. 7.10. The second case, referenced as *Distributed x (fluc. IC)*, corresponds to the conditions applied in Fig. 7.12. In this case, a shaded blue area is also presented and represents the distribution of the integrated values for the 250 fluctuating events performed. The last case, denoted as $R = 0$ *fm (smooth IC)*, represents the analysis performed with a single smooth initial condition, in which the jet energy-momentum was inserted at a position defined by $x = y = \eta_s = 0$, with momentum pointing to the $+x$ axis. Results obtained for each analysis scenario in the absence of thermalized jet insertion are also presented and plotted with unfilled markers. For these cases, the legend provides the corresponding reference angles in the calculation for $\mathcal{R}^J_\Lambda$.

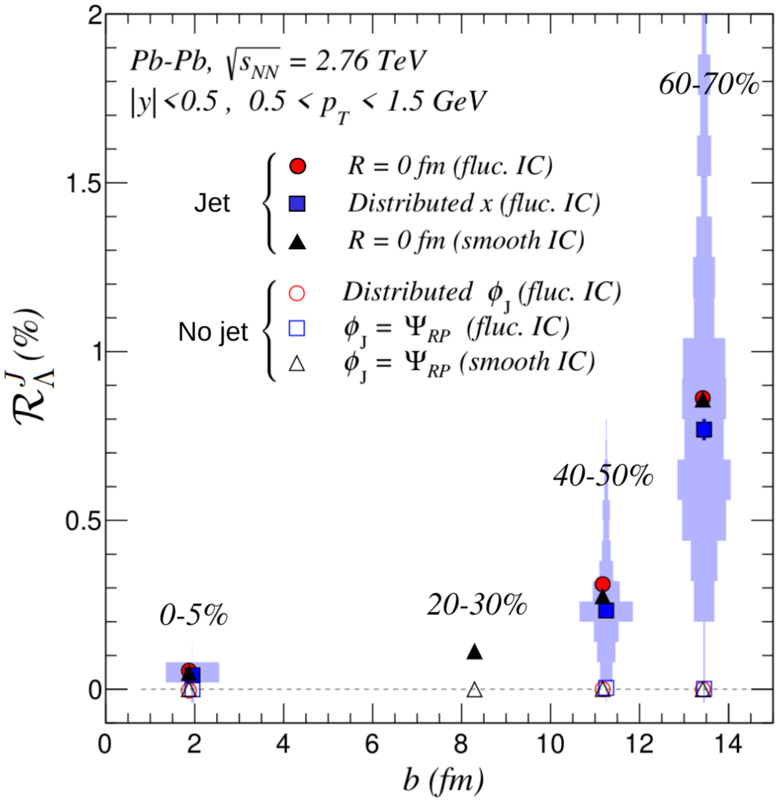

Figure 7.15: Values of integrated $\mathcal{R}^J_\Lambda$ as a function of the impact parameter b for different scenarios, including those with and without the insertion of the thermalized jet. The results were obtained for different conditions of simulation: jet inserted in the center $R = 0$ with fluctuating IC; varying the jet insertion position in the x-axis in fluctuating IC; and jet in the center with smooth IC. The shaded area corresponds to the distribution of the event-by-event $\mathcal{R}^J_\Lambda$ values obtained from the 250 events of the *Distributed x (fluc. IC)* analysis.

The results presented in Fig. 7.15 reveal an increase of the magnitude of the ring observable induced by the jet-medium interactions in peripheral collisions. This dependence can be attributed to a combination of factors. Firstly, in peripheral collisions, the ratio between the deposited energy from the jet and background energy density is greater than in central collisions, leading to bigger velocity gradients within the peripheral events. Additionally, peripheral collisions present a shorter total evolution time, which results in an earlier particlization when the vorticity field induced by the thermalization of the jet is stronger. Together with this observation, the azimuthal-integrated ring observable consistently approaches zero in cases where no energy-momentum current is deposited from quenched jets. This result shows that the proposed ring observable is a robust experimental observable that can be used as a signature and probe of the jet thermalization in the QGP.

CHAPTER 8

CONCLUSIONS

In this work, we performed a systematic investigation of the influence of energy-momentum currents from quenched jets on the generation of vorticity ring structures inside the Quark-Gluon Plasma. Regarding the hydrodynamic description of the QGP, we used the connection between the physical observable of polarization and the properties of vorticity presented by that relativistic fluid in order to evaluate the proposed model for jet thermalization.

To expand on the previous work developed in that scenario [19, 20], we improved our analysis to a more realistic condition by considering peripheral events and also fluctuations in the initial states of a heavy-ion collision. With this configuration we computed the polarization of the Λ hyperons induced by the vorticity generated in the thermalization of the quenched jet and applied the experimental framework of the ring observable to extract information about the different aspects of jet-medium interactions.

Our systematic study provided compelling evidence that the ring observable is a highly sensitive tool to probe the dynamics not only due to jet-medium interactions, but also to the expansion dynamics of the QGP. Our findings demonstrates that the ring observable $\mathcal{R}^J_\Lambda$ is sensitive to several factors, as the momentum of the quenched jet, the specific shear viscosity of the medium, and also the location and orientation of the energy-momentum current deposited from quenched jets. Furthermore, our calculations showed that the ring observable is robust against fluctuations in the initial condition, providing a signal that has the same magnitude as reported by ALICE and STAR for the global Λ polarization [18, 88]. Such an agreement suggests that the proposed observable can be experimentally measured, thereby offering a clear signal of the thermalization of the energy lost by a quenched jet.

The main results of this dissertation have been submitted to the Physical Review C journal, published by the American Physical Society, and are also available on ArXiv as Ref. [1].

BIBLIOGRAPHY

[1] Ribeiro, V. H. *et al.* Λ polarization from vortex ring as medium response for jet thermalization (2023). 2305.02428.

[2] Schäfer, T. & Teaney, D. Nearly perfect fluidity: from cold atomic gases to hot quark gluon plasmas. *Reports on Progress in Physics* **72**, 126001 (2009).

[3] Gale, C., Jeon, S. & Schenke, B. Hydrodynamic modeling of heavy-ion collisions. *International Journal of Modern Physics A* **28**, 1340011 (2013).

[4] de Souza, R. D., Koide, T. & Kodama, T. Hydrodynamic approaches in relativistic heavy ion reactions. *Progress in Particle and Nuclear Physics* **86**, 35–85 (2016).

[5] Shuryak, E. Strongly coupled quark-gluon plasma in heavy ion collisions. *Reviews of Modern Physics* **89** (2017).

[6] Werner, K., Karpenko, I., Bleicher, M., Pierog, T. & Porteboeuf-Houssais, S. Jets, bulk matter, and their interaction in heavy ion collisions at several TeV. *Physical Review C* **85** (2012).

[7] Shen, C. & Yan, L. Recent development of hydrodynamic modeling in heavy-ion collisions (2020). 2010.12377.

[8] da Silva, T. N. *et al.* Prehydrodynamic evolution in large and small systems. *Physical Review C* **107** (2023).

[9] Busza, W., Rajagopal, K. & van der Schee, W. Heavy ion collisions: The big picture and the big questions. *Annual Review of Nuclear and Particle Science* **68**, 339–376 (2018).

[10] Cern Courier, tracks from a lead–lead collision recorded by the ALICE TPC. `https://cerncourier.com/a/heavy-ion-physics-past-present-and-future/`.

[11] Gyulassy, M. & Plümer, M. Jet quenching in dense matter. *Physics Letters B* **243**, 432–438 (1990).

[12] Blaizot, J.-P. & Mehtar-Tani, Y. Jet structure in heavy ion collisions. *International Journal of Modern Physics E* **24**, 1530012 (2015).

[13] Wang, X.-N. & Gyulassy, M. Gluon shadowing and jet quenching in A+A collisions at $\sqrt{s}$ =200 GeV. *Phys. Rev. Lett.* **68**, 1480–1483 (1992).

[14] Wiedemann, U. A. Jet quenching in heavy ion collisions. In *Relativistic Heavy Ion Physics*, 521–562 (Springer Berlin Heidelberg, 2010).

[15] Cao, S. & Wang, X.-N. Jet quenching and medium response in high-energy heavy-ion collisions: a review. *Reports on Progress in Physics* **84**, 024301 (2021).

[16] Aad, G. *et al.* Observation of a centrality-dependent dijet asymmetry in lead-lead collisions at $\sqrt{s_{NN}} = 2.76$ TeV with the ATLAS Detector at the LHC. *Phys. Rev. Lett.* **105**, 252303 (2010).

[17] Chatrchyan, S. *et al.* Observation and studies of jet quenching in pb-pb collisions at $\sqrt{s_{NN}} = 2.76$ TeV. *Phys. Rev. C* **84**, 024906 (2011).

[18] STAR Collaboration. Global Λ hyperon polarization in nuclear collisions. *Nature* **548**, 62–65 (2017).

[19] Serenone, W. M. *et al.* Λ polarization from thermalized jet energy. *Physics Letters B* **820**, 136500 (2021).

[20] Barbon, J. G. P. *Jets, vortices and Λ polarization in the quark-gluon plasma*. Dissertation, Instituto de Física Gleb Wataghin, Campinas, SP (2021).

[21] Becattini, F. & Lisa, M. A. Polarization and vorticity in the quark–gluon plasma. *Annual Review of Nuclear and Particle Science* **70**, 395–423 (2020).

[22] Lisa, M. A. *et al.* Vortex rings from high energy central p+A collisions. *Phys. Rev. C* **104**, L011901 (2021).

[23] Vogt, R. *Ultrarelativistic heavy-ion collisions* (Elsevier, Amsterdam, 2007).

[24] Cern Courier, reporting on international high-energy physics. `https://cerncourier.com/wp-content/uploads/2019/01/CCJanFeb19_Alice-frontis.jpg`.

[25] Wong, C. *Introduction to high-energy heavy-ion collisions* (World scientific, Singapore, 1994).

[26] Bernhard, J. E. Bayesian parameter estimation for relativistic heavy-ion collisions (2018). `1804.06469`.

[27] Aamodt, K. *et al.* Centrality dependence of the charged-particle multiplicity density at midrapidity in Pb-Pb collisions at $\sqrt{s_{NN}} = 2.76$ TeV. *Physical Review Letters* **106** (2011).

[28] MADAI Collaboration, models and data analysis initiative. `https://madai.phy.duke.edu/`.

[29] Picchetti, J. P. Studying the impact of the nucleon size in relativistic heavy-ion collisions (2022). 2210.03186.

[30] Connors, M., Nattrass, C., Reed, R. & Salur, S. Jet measurements in heavy ion physics. *Reviews of Modern Physics* **90** (2018).

[31] Brewer, J. Jets as a probe of the quark-gluon plasma (2020). 2012.14457.

[32] Heinz, U. & Snellings, R. Collective flow and viscosity in relativistic heavy-ion collisions. *Annual Review of Nuclear and Particle Science* **63**, 123–151 (2013).

[33] Kaneta, M. *Thermal and Chemical Freeze-out in Heavy Ion Collisions*. Ph.D. thesis, Hiroshima U. (1999).

[34] ALICE Collaboration. *The ALICE experiment – A journey through QCD* (arXiv, 2022).

[35] Guenther, J. Overview of the QCD phase diagram. *European Physical Journal A* **57**, 136 (2021).

[36] Aoki, Y., Endrődi, G., Fodor, Z., Katz, S. D. & Szabó, K. K. The order of the quantum chromodynamics transition predicted by the standard model of particle physics. *Nature* **443**, 675–678 (2006).

[37] Alford, M., Rajagopal, K. & Wilczek, F. QCD at finite baryon density: nucleon droplets and color superconductivity. *Physics Letters B* **422**, 247–256 (1998).

[38] Tlusty, D. The RHIC beam energy scan phase II: Physics and upgrades (2018). URL `https://arxiv.org/abs/1810.04767`.

[39] Back, B. *et al.* The PHOBOS perspective on discoveries at RHIC. *Nuclear Physics A* **757**, 28–101 (2005).

[40] Arsene, I. *et al.* Quark-gluon plasma and color glass condensate at RHIC? the perspective from the BRAHMS experiment. *Nuclear Physics A* **757**, 1–27 (2005).

[41] Adams, J. *et al.* Experimental and theoretical challenges in the search for the quark-gluon plasma: The STAR collaboration's critical assessment of the evidence from RHIC collisions. *Nuclear Physics A* **757**, 102–183 (2005).

[42] Adcox, K. *et al.* Formation of dense partonic matter in relativistic nucleus-nucleus collisions at RHIC: Experimental evaluation by the PHENIX collaboration. *Nuclear Physics A* **757**, 184–283 (2005).

[43] Niida, T. & Miake, Y. Signatures of QGP at RHIC and the LHC. *AAPPS Bull.* **31**, 12 (2021). 2104.11406.

[44] Adler, C. *et al.* Azimuthal anisotropy and correlations in the hard scattering regime at RHIC. *Phys. Rev. Lett.* **90**, 032301 (2003).

[45] Voloshin, S. & Zhang, Y. Flow study in relativistic nuclear collisions by fourier expansion of azimuthal particle distributions. *Zeitschrift for Physik C Particles and Fields* **70**, 665–671 (1996).

[46] Niemi, H., Denicol, G. S., Holopainen, H. & Huovinen, P. Event-by-event distributions of azimuthal asymmetries in ultrarelativistic heavy-ion collisions. *Physical Review C* **87** (2013).

[47] Qiu, Z. Event-by-event hydrodynamic simulations for relativistic heavy-ion collisions (2013). `1308.2182`.

[48] Adare, A. *et al.* Measurements of higher order flow harmonics in Au+Au collisions at $\sqrt{s_{NN}} = 200$ Gev. *Physical Review Letters* **107** (2011).

[49] Pandit, Y. Beam energy dependence of first and higher-order flow harmonics from the STAR experiment at RHIC. *Nuclear Physics A* **904-905**, 357c–360c (2013).

[50] Landau, L. & Lifshitz, E. *Fluid Mechanics: Volume 6*. v. 6 (Elsevier Science, 1987). URL `https://books.google.com.br/books?id=eVKbCgAAQBAJ`.

[51] Gabriel S. Denicol, D. H. R. *Microscopic Foundations of Relativistic Fluid Dynamics* (Springer Cham, 2022), 1d ed. edn.

[52] Israel, W. Nonstationary irreversible thermodynamics: A Causal relativistic theory. *Annals Phys.* **100**, 310–331 (1976).

[53] Israel, W. & Stewart, J. M. Transient relativistic thermodynamics and kinetic theory. *Annals of Physics* **118**, 341–372 (1979).

[54] Derradi de Souza, R., Koide, T. & Kodama, T. Hydrodynamic approaches in relativistic heavy ion reactions. *Progress in Particle and Nuclear Physics* **86**, 35–85 (2016).

[55] Song, H. & Heinz, U. Interplay of shear and bulk viscosity in generating flow in heavy-ion collisions. *Phys. Rev. C* **81**, 024905 (2010).

[56] Marrochio, H. *et al.* Solutions of conformal israel-stewart relativistic viscous fluid dynamics. *Phys. Rev. C* **91**, 014903 (2015).

[57] Baier, R., Romatschke, P., Son, D. T., Starinets, A. O. & Stephanov, M. A. Relativistic viscous hydrodynamics, conformal invariance, and holography. *Journal of High Energy Physics* **2008**, 100 (2008).

[58] Denicol, G. S., Kodama, T., Koide, T. & Mota, P. Effect of bulk viscosity on elliptic flow near the QCD phase transition. *Phys. Rev. C* **80**, 064901 (2009).

[59] Luzum, M. & Ollitrault, J.-Y. Extracting the shear viscosity of the quark-gluon plasma from flow in ultra-central heavy-ion collisions. *Nuclear Physics A* **904-905**, 377c–380c (2013). The Quark Matter 2012.

[60] Jaiswal, A. & Roy, V. Relativistic hydrodynamics in heavy-ion collisions: General aspects and recent developments. *Advances in High Energy Physics* **2016**, 1–39 (2016).

[61] White, F. M. *Fluid mechanics.* Mcgraw-Hill series in mechanical engineering (McGraw-Hill, New York, NY, 2009), 6th ed edn.

[62] Acheson, D. J. *Elementary Fluid Dynamics* (Clarendon, Oxford, 1990).

[63] Gourgoulhon, E. An introduction to relativistic hydrodynamics. *EAS Publications Series* **21**, 43–79 (2006).

[64] Becattini, F. *et al.* A study of vorticity formation in high energy nuclear collisions. *The European Physical Journal C* **75** (2015).

[65] Komm, R. *et al.* Divergence and Vorticity of Subsurface Flows Derived from Ring-Diagram Analysis of MDI and GONG Data. In Lacoste, H. & Ouwehand, L. (eds.) *SOHO-17. 10 Years of SOHO and Beyond*, vol. 617 of *ESA Special Publication*, 42 (2006).

[66] Perry, C. A. Midwestern streamflow, precipitation, and atmospheric vorticity influenced by pacific sea-surface temperatures and total solar-irradiance variations. *International Journal of Climatology* **26**, 207–218 (2006).

[67] Wurman, J., Richardson, Y., Alexander, C., Weygandt, S. & Zhang, P. F. Dual-doppler analysis of winds and vorticity budget terms near a tornado. *Monthly Weather Review* **135**, 2392 – 2405 (2007).

[68] Choi, D., Banfield, D., Gierasch, P. & Showman, A. Velocity and vorticity measurements of jupiter's great red spot using automated cloud feature tracking. *Icarus* **188**, 35–46 (2007).

[69] Gerlach, W. & Stern, O. Der experimentelle Nachweis der Richtungsquantelung im Magnetfeld. *Zeitschrift fur Physik* **9**, 349–352 (1922).

[70] Merzbacher, E. *Quantum mechanics [by] Eugen Merzbacher* (J. Wiley New York, 1970), 2d ed. edn.

[71] Liang, Z.-T. Spin effects in heavy ion collisions at high energies. In *Proceedings of the 24th International Spin Symposium (SPIN2021)* (Journal of the Physical Society of Japan, 2022).

[72] Einstein, A. & de Haas, W. J. Experimental proof of the existence of Ampère's molecular currents. *Koninklijke Nederlandse Akademie van Wetenschappen Proceedings Series B Physical Sciences* **18**, 696–711 (1915).

[73] Barnett, S. J. Magnetization by Rotation. *Physical Review* **6**, 239–270 (1915).

[74] Matsuo, M., Ieda, J. & Maekawa, S. Mechanical generation of spin current. *Frontiers in Physics* **3** (2015).

[75] Griffiths, D. J. *Introduction to electrodynamics* (Pearson, 2013).

[76] Jackson, J. D. *Classical electrodynamics* (Wiley, New York, NY, 1999), 3rd ed. edn.

[77] Takahashi, R. *et al.* Spin hydrodynamic generation. *Nature Physics* **12**, 52–56 (2016).

[78] Liang, Z.-T. & Wang, X.-N. Globally polarized quark-gluon plasma in noncentral A+A collisions. *Phys. Rev. Lett.* **94**, 102301 (2005).

[79] Cooper, F. & Frye, G. Single-particle distribution in the hydrodynamic and statistical thermodynamic models of multiparticle production. *Phys. Rev. D* **10**, 186–189 (1974).

[80] Cooper, F., Frye, G. & Schonberg, E. Landau's hydrodynamic model of particle production and electron-positron annihilation into hadrons. *Phys. Rev. D* **11**, 192–213 (1975).

[81] Lee, T. D. & Yang, C. N. General partial wave analysis of the decay of a hyperon of spin $\frac{1}{2}$. *Phys. Rev.* **108**, 1645–1647 (1957). URL `https://link.aps.org/doi/10.1103/PhysRev.108.1645`.

[82] Group, P. D. Review of Particle Physics. *Progress of Theoretical and Experimental Physics* **2020** (2020).

[83] Poskanzer, A. M. & Voloshin, S. A. Methods for analyzing anisotropic flow in relativistic nuclear collisions. *Phys. Rev. C* **58**, 1671–1678 (1998).

[84] Adam, J. *et al.* Global polarization of Ξ and Ω in Au+Au collisions at $\sqrt{s_{NN}} = 200$ GeV. *Physical Review Letters* **126** (2021).

[85] Csernai, L. P., Wang, D. J., Bleicher, M. & Stöcker, H. Vorticity in peripheral collisions at the facility for antiproton and ion research and at the jinr nuclotron-based ion collider facility. *Phys. Rev. C* **90**, 021904 (2014).

[86] Karpenko, I. & Becattini, F. Study of lambda polarization in relativistic nuclear collisions at $\sqrt{s_{NN}} = 7.7 - 200$ GeV. *The European Physical Journal C* **77** (2017).

[87] Betz, B., Gyulassy, M. & Torrieri, G. Polarization probes of vorticity in heavy ion collisions. *Physical Review C* **76** (2007).

[88] Acharya, S. e. a. Global polarization of Λ and $\overline{\Lambda}$ hyperons in Pb-Pb collisions at $\sqrt{s_{NN}} = 2.76$ and 5.02 TeV. *Phys. Rev. C* **101**, 044611 (2020).

[89] Adam, J. *et al.* Polarization of $\Lambda(\bar{\Lambda})$ hyperons along the beam direction in Au+Au collision at $\sqrt{s_{NN}} = 200$ GeV. *Physical Review Letters* **123** (2019).

[90] Adamczyk, L. *et al.* Centrality dependence of identified particle elliptic flow in relativistic heavy ion collisions at $\sqrt{s} = 7.7 - -62.4$ GeV. *Physical Review C* **93** (2016).

[91] Jiang, Y., Lin, Z.-W. & Liao, J. Rotating quark-gluon plasma in relativistic heavy-ion collisions. *Phys. Rev. C* **94**, 044910 (2016).

[92] Pang, L.-g., Petersen, H., Wang, Q. & Wang, X.-N. Vortical fluid and Λ spin correlations in high-energy heavy-ion collisions. *Phys. Rev. Lett.* **117**, 192301 (2016).

[93] Becattini, F. & Karpenko, I. Collective longitudinal polarization in relativistic heavy-ion collisions at very high energy. *Phys. Rev. Lett.* **120**, 012302 (2018).

[94] Xia, X.-L., Li, H., Tang, Z. & Wang, Q. Probing vorticity structure in heavy-ion collisions by local Λ polarization. *Phys. Rev. C* **98**, 024905 (2018).

[95] Becattini, F., Buzzegoli, M. & Palermo, A. Spin-thermal shear coupling in a relativistic fluid. *Physics Letters B* **820**, 136519 (2021).

[96] Liu, S. Y. F. & Yin, Y. Spin polarization induced by the hydrodynamic gradients. *Journal of High Energy Physics* **2021** (2021).

[97] Yi, C., Pu, S. & Yang, D.-L. Reexamination of local spin polarization beyond global equilibrium in relativistic heavy ion collisions. *Physical Review C* **104** (2021).

[98] Norbeck, E., Šafařík, K. & Steinberg, P. A. Hard-scattering results in heavy-ion collisions at the lhc. *Annual Review of Nuclear and Particle Science* **64**, 383–411 (2014).

[99] Thomson, M. *Modern Particle Physics* (Cambridge University Press, 2013).

[100] Qin, G.-Y. & Wang, X.-N. Jet quenching in high-energy heavy-ion collisions. *International Journal of Modern Physics E* **24**, 1530014 (2015).

[101] American Physical Society, the stopping power of hot nuclear matter. https://physics.aps.org/articles/v7/97.

[102] Cern Document Server, CMS experiment. http://cdsweb.cern.ch/record/1309898.

[103] Aaboud, M. *et al.* Measurement of the nuclear modification factor for inclusive jets in Pb+Pb collisions at $\sqrt{s_{NN}} = 5.02$ TeV with the ATLAS detector. *Physics Letters B* **790**, 108–128 (2019).

[104] Miller, M. L., Reygers, K., Sanders, S. J. & Steinberg, P. Glauber modeling in high-energy nuclear collisions. *Annual Review of Nuclear and Particle Science* **57**, 205–243 (2007).

[105] Baier, R., Schiff, D. & Zakharov, B. G. Energy loss in perturbative qcd. *Annual Review of Nuclear and Particle Science* **50**, 37–69 (2000).

[106] Gyulassy, M., Vitev, I., Wang, X.-N. & Zhang, B.-W. Jet quenching and radiative energy loss in dense nuclear matter. In *Quark–Gluon Plasma 3*, 123–191 (World Scientific, 2004).

[107] Kovner, A. & Wiedemann, U. A. Gluon radiation and parton energy loss. In *Quark–Gluon Plasma 3*, 192–248 (World Scientific, 2004).

[108] Tachibana, Y. Medium response to jet-induced excitation: theory overview. *Nuclear Physics A* **982**, 156–162 (2019). The 27th International Conference on Ultra-relativistic Nucleus-Nucleus Collisions: Quark Matter 2018.

[109] Ke, W., Moreland, J. S., Bernhard, J. E. & Bass, S. A. Constraints on rapidity-dependent initial conditions from charged-particle pseudorapidity densities and two-particle correlations. *Phys. Rev. C* **96**, 044912 (2017).

[110] Jacak, B. V. & Müller, B. The exploration of hot nuclear matter. *Science* **337**, 310–314 (2012).

[111] Abbas, E. *et al.* Centrality dependence of the pseudorapidity density distribution for charged particles in Pb–Pb collisions at $\sqrt{s_{NN}} = 2.76$ TeV. *Physics Letters B* **726**, 610–622 (2013).

[112] Schenke, B., Jeon, S. & Gale, C. (3+1)D hydrodynamic simulation of relativistic heavy-ion collisions. *Phys. Rev. C* **82**, 014903 (2010).

[113] Schenke, B., Jeon, S. & Gale, C. Higher flow harmonics from (3+1)D event-by-event viscous hydrodynamics. *Phys. Rev. C* **85**, 024901 (2012).

[114] Paquet, J.-F. m. c. *et al.* Production of photons in relativistic heavy-ion collisions. *Phys. Rev. C* **93**, 044906 (2016).

[115] Bazavov, A. *et al.* Equation of state in (2+1)-flavor QCD. *Phys. Rev. D* **90**, 094503 (2014).

[116] Chun Chen, iSS: Monte Carlo sampler for particle distribution from Cooper-Frye freeze-out procedure. `https://github.com/chunshen1987/iSS`.

[117] Sinharay, S. Jackknife methods. In *International Encyclopedia of Education (Third Edition)*, 229–231 (Elsevier, Oxford, 2010), third edition edn.

[118] Gardim, F. G., Giacalone, G., M., L. *et al.* Thermodynamics of hot strong-interaction matter from ultrarelativistic nuclear collisions. *Nature Physics* **16**, 615–619 (2020).

[119] Becattini, F., Buzzegoli, M., Palermo, A., Inghirami, G. & Karpenko, I. Local polarization and isothermal local equilibrium in relativistic heavy ion collisions. *Phys. Rev. Lett.* **127**, 272302 (2021).

APPENDICES

APPENDIX A

COMPLEMENTARY ANALYSIS ON COLLECTIVE EXPANSION OF THE QGP

In this complementary analysis, we performed an exploratory study on the ring observable for the vorticity induced by the anisotropic expansion of the hydrodynamic medium that corresponds to the Quark-Gluon Plasma. Regarding that topic of medium expansion, it is possible to evaluate the evolution of the system in two distinct scenarios: the longitudinal and the transverse expansion.

The longitudinal expansion accounts for the dynamics that can be observed along the longitudinal direction, which is illustrated in Fig A.1 with the black arrows in the z axis. The transverse dynamics is related to the expansion in the transverse $x - y$ plane, which is illustrated in the red arrows of Fig. A.1. In both scenarios, the presence of an anisotropic dynamics gives rise to local non-zero vorticity. In the case of longitudinal expansion, the vorticity field generated will be responsible for inducing the polarization of the particles in the directions perpendicular to the longitudinal axis, which means $\hat{y}$ and $\hat{x}$ directions. In contrast, the transverse expansion will be responsible for inducing the polarization of particles in the longitudinal z direction.

For the simulations conducted in this analysis, we used a smooth initial condition equivalent to 0-5% centrality class, which was hydrodynamically evolved without any jet insertion. After the hydrodynamic stage, in the particlization step where the polarization is calculated, we accounted for recent works that suggests a different definition of the spin-vorticity coupling that was presented in Chapter 4. These recent definitions indicates an additional contribution to spin polarization due to a shear-induced term [95, 96] that is summed to the current the thermal vorticity contribution. In both works, the mean spin vector of the Λ hyperons is defined with a similar relation compared to Eq. (4.3)

$$S^{\mu}(p) = -\frac{1}{4m}\frac{\int_{\Sigma} \mathrm{d}\Sigma \cdot p\, n_F(1-n_F)\mathcal{A}^{\mu}}{\int_{\Sigma} \mathrm{d}\Sigma \cdot p\, n_F}, \tag{A.1}$$

where $\mathcal{A}^{\mu}$ corresponds to the different derivations for the shear contribution achieved in each analysis [95, 96].

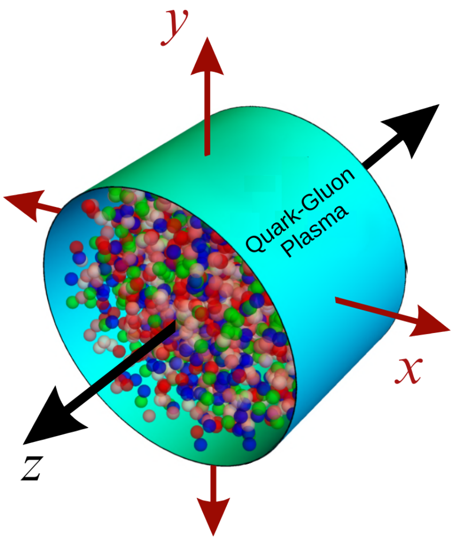

Figure A.1: Schematic representation of the expansion dynamics of the quark-gluon plasma created in a heavy-ion collisions. The red arrows represents the transverse expansion and the black arrows indicates the longitudinal expansion. Modified from Ref. [118]

In Ref. [95], the complementing term of Eq. (A.1) is given by

$$\mathcal{A}^{\mu}_{BBP} = \epsilon^{\mu\nu\sigma\tau}\left(\frac{1}{2}\varpi_{\nu\sigma}p_{\tau} + \frac{1}{E}\hat{t}_{\nu}\xi_{\sigma\lambda}p^{\lambda}p_{\tau}\right), \tag{A.2}$$

where $\hat{t} = (1,0,0,0)$ corresponds to a global vector, ε represents the energy density and $\xi_{\sigma\lambda}$ is the thermal shear tensor defined as

$$\xi_{\mu\nu} = \frac{1}{2}(\partial_{\mu}\beta_{\nu} + \partial_{\nu}\beta_{\mu}) \tag{A.3}$$

with β_{μ} corresponding to the temperature four-vector $\beta_{\mu} = u_{\mu}/T$.

On the other hand, in Ref. [96, 97], the definition of the mean spin vector is complemented by the term

$$\mathcal{A}^{\mu}_{LY} = \epsilon^{\mu\nu\sigma\tau}\left[\frac{1}{2}\varpi_{\nu\sigma}p_{\tau} + \frac{1}{E}u_{\nu}\xi_{\sigma\lambda}p^{\lambda}_{\perp}p_{\tau}\right], \tag{A.4}$$

where $p^{\lambda}_{\perp}$ corresponds to an additional transverse projection operator defined as

$$p^{\lambda}_{\perp} = p^{\lambda} - (u\cdot p)u^{\lambda}. \tag{A.5}$$

In Fig. A.2, we compared the azimuthal distribution of the ring observable with and without the shear-induced polarization and also for both definitions that included a shear term. For that results, the ring observable was calculated considering a p_T interval in the range of $0.5 < p_T < 3.0$ GeV/c, which prioritizes the signal of the background as could be seen in the left panel of Fig. 7.2, and we maintain the same interval for the rapidity cut.

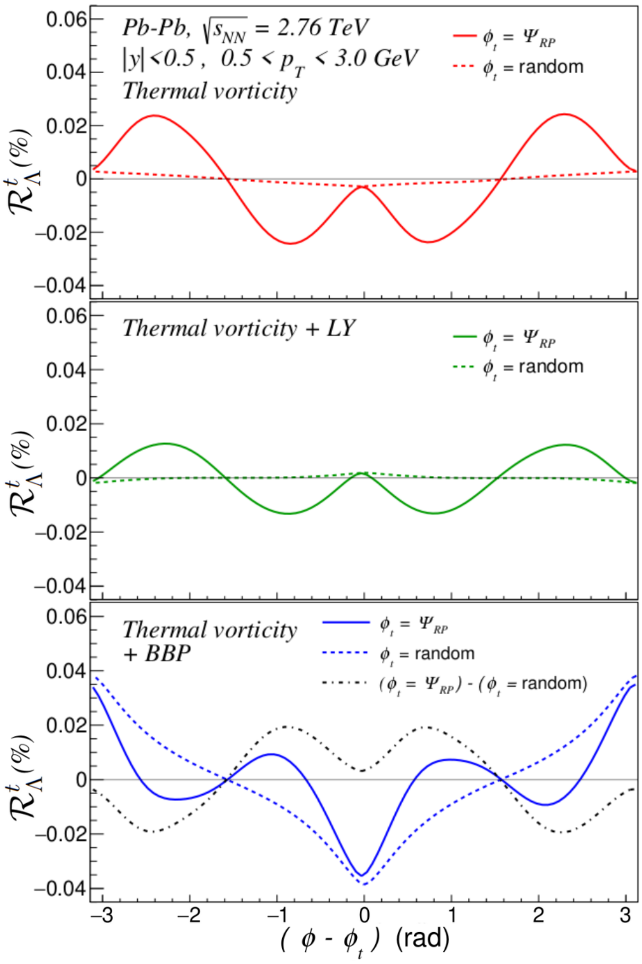

Figure A.2: Values of $\mathcal{R}^t_\Lambda$ with different definitions of the polarization induced by the expansion of the system for 0-5% Pb+Pb collisions. These results correspond to an analysis where a smooth initial condition was used. The solid lines represent $\mathcal{R}^t_\Lambda$ calculated for the trigger angle ϕ_t in the reaction plane Ψ_{RP} and the dashed lines correspond to results obtained from an analysis where $\mathcal{R}^t_\Lambda$ was averaged over 1000 different ϕ_t sampled from a uniform distribution defined by the interval $[0, 2\pi)$. The top panel corresponds to results where the polarization is induced by the local thermal vorticity. The middle panel corresponds to results where the polarization is defined by the sum of the thermal vorticity contribution with the shear-induced term LY from [96]. The bottom panel corresponds to results where the polarization is defined by the sum of the thermal vorticity contribution with the shear-induced term BBP from [95]. The black dot-dashed line in the bottom panel represents a proxy signal that only displays contributions of the transverse expansion.

We showed that summing the signals calculated with different ϕ_t would average zero and vanish with the contribution of polarization induced by the transverse expansion of the system (see the red dashed lines on Fig. 7.6). Since this method is based on azimuthal correlations in the $x - y$ plane, it is expected that it should not affect the distribution of polarization in the longitudinal plane. The result of this statement is that the contribution of polarization induced by the longitudinal expansion will not average to zero as the transverse contribution does. Such an observation, characterized through the calculus of the ring observable, presents a characteristic that could be used in order to decouple the longitudinal contribution from the transverse one. This process is employed in the current analysis by averaging $\mathcal{R}^t_\Lambda$ over 1000 calculations with ϕ_t being selected at random from a uniform distribution of the interval $[0, 2\pi)$. The resulting signal obtained from this method is shown Fig. A.2 and referenced as $\phi_t =$ random.

For the considerations of our results, expressed in Fig. A.2, the signal obtained with $\phi_t = \Psi_{RP}$, accounts for both transversal and longitudinal expansions, while for $\phi_t =$ random the transversal contribution is averaged out and the signal is attributed just to the longitudinal contributions. In that context, Fig. A.2 shows the results obtained for each definition of polarization in a different panel. The curves expressed in the top panel represents the signal obtained from the polarization calculated just from the thermal vorticity. The central panel corresponds to results where the polarization accounts the shear induced term derived in Ref. [96, 97]. Then, the bottom panel corresponds to a signal obtained from a polarization defined by the shear term contribution from Ref. [95].

In both top and central panels of Fig. A.2, it is possible to verify that signal of $\mathcal{R}^t_\Lambda$ attributed just to the longitudinal expansion (dashed lines) presents a small magnitude relative to the result where the transversal contribution also accounts (solid line). In contrast, a great difference is observed for the results where the polarization is defined by the inclusion of the shear-induced term derived in Ref. [95]. In the bottom panel of Fig. A.2, the comparison of the dashed line with the solid one reveals a remarkable increase of the longitudinal contribution. In order to compare the transversal and longitudinal contributions produced by that definition of polarization, we subtracted the signal obtained with $\phi_t =$ random from the signal where $\phi_t = \Psi_{RP}$. This method is used as a proxy to isolate the contribution that should be caused just by the transversal expansion. The result of that subtraction is expressed in the black dash-dotted line.

Comparing the magnitudes of the signal induced by just the longitudinal dynamics (dashed line) with the proxy-signal attributed just to the transversal expansion (dash-dotted line), the maximum value achieved for the longitudinal contribution presents a magnitude that accounts for almost twice the maximum observed for the transverse signal. This observation indicates a dominance of the longitudinal contribution and represents an inversion of the hierarchy presented by the other two definitions of polarization. It is also important to highlight that the qualitative properties of the black dash-dotted line of the lower panel in Fig. A.2 are very similar to the properties of the signal represented by the solid lines in the top and center panels. All the results present the same azimuthal dependence, which is characteristic of a signal induced by the transverse anisotropic expansion of the medium. The only striking difference observed in the comparison is the sign presented by the curve in the lower panel, which is opposite to the sign observed for curves in the center and upper panels. That difference is in accordance with the properties observed in [119], which indicates an inversion of the polarization signal for the polarization calculated using the shear-induced contribution of Ref. [95].